POLITECNICO DI MILANO

School of Civil, Environment and Land Management Engineering

Master of Science – Environmental and Land Planning Engineering

Laboratory study of $Ca(OH)_2$ dissolution dynamics in artificial seawater

Supervisor:	Stefano Caserini	Candidates:	
Co-supervisor:	Piero Macchi	Matteo Colombo	943736
	Guido Raos	Francesco Crisanto	945173

Academic Year 2020-2021

Ringraziamo tutto il team che ha collaborato e reso possibile lo sviluppo di questa tesi e che ci ha supportato durante il percorso di ricerca. In particolare, i Professori Piero Macchi, Guido Raos e Stefano Caserini che si sono sempre spesi per noi; le dottorande Simona Sorbara, sempre preziosa e disponibile, Selene Varliero, per il supporto teorico e Serena De Marco, che ci ha aiutati nella stesura della sezione riguardante le elaborazioni statistiche dei risultati.

Contents

List of figures

List of tables

Abstract

This thesis concerns the dissolution kinetics of calcium hydroxide — $Ca(OH)_2$, also known as slaked lime, SL — in artificial seawater. The aim of the research is to characterize the dissolution kinetics in order to provide information for the use of SL for ocean alkalinization, since the effects after its release into the sea have not yet been exhaustively studied. The use of SL for ocean alkalinization has two objectives: the contrast of ocean acidification and the CO_2 absorption by sequestration from the atmosphere. An in-depth knowledge of the dissolution kinetics is important so as to optimize the dispersion of SL, minimizing at the same time the possible negative effects on the marine environment.

The SL dissolution was studied in laboratory experiments by monitoring some variables of artificial seawater, with varying amounts of added $Ca(OH)_2$. The solutions, contained in beakers under stirring, with a finite and constant volume, are in contact with the atmosphere. Several parameters were varied to measure, using appropriate sensors, the response of the variables, such as: pH and conductivity, with temporal resolution of one second. Moreover, additional measurements were made to quantify the alkalinity and solid residues after filtration of the solutions. The parameters varied during the tests were instead: temperature, salinity, stirring mode, the concentration and mode of dispersion of calcium hydroxide.

The results show that the release of SL into seawater causes an increment in the values of pH, conductivity and alkalinity. The pH reaches values between 10 and 11, for SL concentrations up to 4 g/L. Above this concentration it grows rapidly, reaching values above 12, as in the case of 8 g/L. The variation of conductivity presents the same behaviour of the pH, with a sharp increase above the concentration of 4 g/L. Alkalinity increases significantly too, depending on the concentration and the time after the release of SL. The analysis of the filtered matter by X-ray diffraction reveals that it is mainly composed of brucite ($Mg(OH)_2$) and calcite ($CaCO_3$), while the SL is completely dissolved. The present data may be used to test and validate kinetics and fluid-dynamics models.

Sommario

Questa tesi riguarda la dissoluzione dell'idrossido di calcio — $Ca(OH)_2$, chiamato anche slaked lime, SL — in acqua di mare artificiale. La ricerca si pone come intento la caratterizzazione della cinetica di dissoluzione, al fine di fornire informazioni per l'utilizzo di SL per l'alcalinizzazione degli oceani, poiché i suoi effetti dopo il rilascio in mare non sono stati ancora studiati in maniera esaustiva. L'utilizzo di SL per l'alcalinizzazione degli oceani ha due obiettivi principali: il contrasto dell'acidificazione degli oceani e l'assorbimento di CO_2 mediante il sequestro dall'atmosfera. Una conoscenza approfondita della cinetica di dissoluzione è importante per ottimizzare la dispersione di SL, minimizzando al tempo stesso le possibili conseguenze negative per l'ecosistema marino.

La dissoluzione di SL è stata studiata tramite esperimenti di laboratorio monitorando alcune variabili dell'acqua di mare artificiale, con quantità variabili di $Ca(OH)_2$. Le soluzioni, contenute in becher sotto agitazione, possiedono quindi un volume finito e costante e si trovano a contatto con l'atmosfera. Diversi parametri sono stati variati per misurare, mediante opportuni sensori, la risposta delle variabili, quali ad esempio: il pH e la conduttività, con risoluzione temporale di un secondo. Inoltre, sono state eseguite ulteriori misure per quantificare l'alcalinità e i residui solidi dopo la filtrazione delle soluzioni. I parametri variati durante le prove sono stati invece: la temperatura, la salinità, la tipologia di agitazione, la concentrazione e la modalità di dispersione dell'idrossido di calcio.

I risultati hanno evidenziato che il rilascio di SL in acqua di mare ha causato un aumento dei valori di pH, conducibilità e alcalinità. Il pH ha raggiunto valori tra 10 e 11 per concentrazioni di SL fino a 4 g/L. Oltre questa concentrazione è cresciuto rapidamente raggiungendo valori superiori a 12, come nel caso di 8 g/L. La variazione di conducibilità ha mostrato lo stesso comportamento del pH, con un forte aumento sopra la concentrazione di 4 g/L. L'alcalinità è aumentata in maniera significativa, in funzione della concentrazione di SL disciolto e del tempo intercorso dal suo rilascio. Tramite un'analisi di diffrazione ai raggi X, è stato rilevato che la materia filtrata è composta principalmente da brucite ($Mg(OH)_2$) e calcite ($CaCO_3$), lo SL viene invece completamente disciolto in soluzione. I dati presentati potranno essere utilizzati per testare e validare modelli di cinetica e fluidodinamica.

1. Introduction

1.1. Climate change

Since the beginning of the nineties, climate change has represented a rising concern, starting from the academic and scientific world, that has progressively conquered space in the economic and social perspective of people and countries.

From a peculiar phenomenon to study, it has been understood that climate change represents a serious threat to the environment, human life and related activities. This fact was clearly highlighted in the 1992 "Earth Summit" of Rio de Janeiro, where the participants signed the UNFCC (United Nation Framework Convention on Climate Change), which stated that stabilization of the emission was a target to reach within a certain period, to avoid possible negative interference of human activities with the Earth's climate system (UN, 1992).

Climate change includes several changes in the natural behaviour of phenomena on which human activity is, for the most part, responsible: these modifications regard the magnitude, the temporal and frequency aspect and the geographic distribution of some events too (IPCC, 2021a).

The scientific community, with a continuous process of publications and reviews that is still ongoing, has ratified that human activity is responsible for these alterations. As common denominator and major driving force, these last have the rising concentrations of Green House Gases (GHGs).

Since mankind became a non-migratory species, relevant in number on the Earth, it has started to alter the composition of the atmosphere, mainly through the discovery of fire, which brings, as a scientific consequence, the phenomenon of combustion, the biggest character from here on. Another significant factor can be traced to the land-use change that mankind has operated to become a settled population.

With the massive revolutions brought by steam machines, powered by coal and internal combustion engines, powered by oil derivatives, the emissions increased on a yearly basis without interruption (fig. 1.1) (IPCC, 2021a). In addition to this last one, a wider number of emitting activities not related to combustion (industrial processes, livestock, land-use change, waste management) have contributed to worsening the problem. There are several emissions, typically grouped under the GHGs, but the most important ones are carbon dioxide (CO_2), methane (CH_4), nitrous oxide (N_2O), water vapour (H_2O), sulphur hexafluoride (SF_6) and various halogenated gases. (fig. 1.2) (IPCC, 2014).

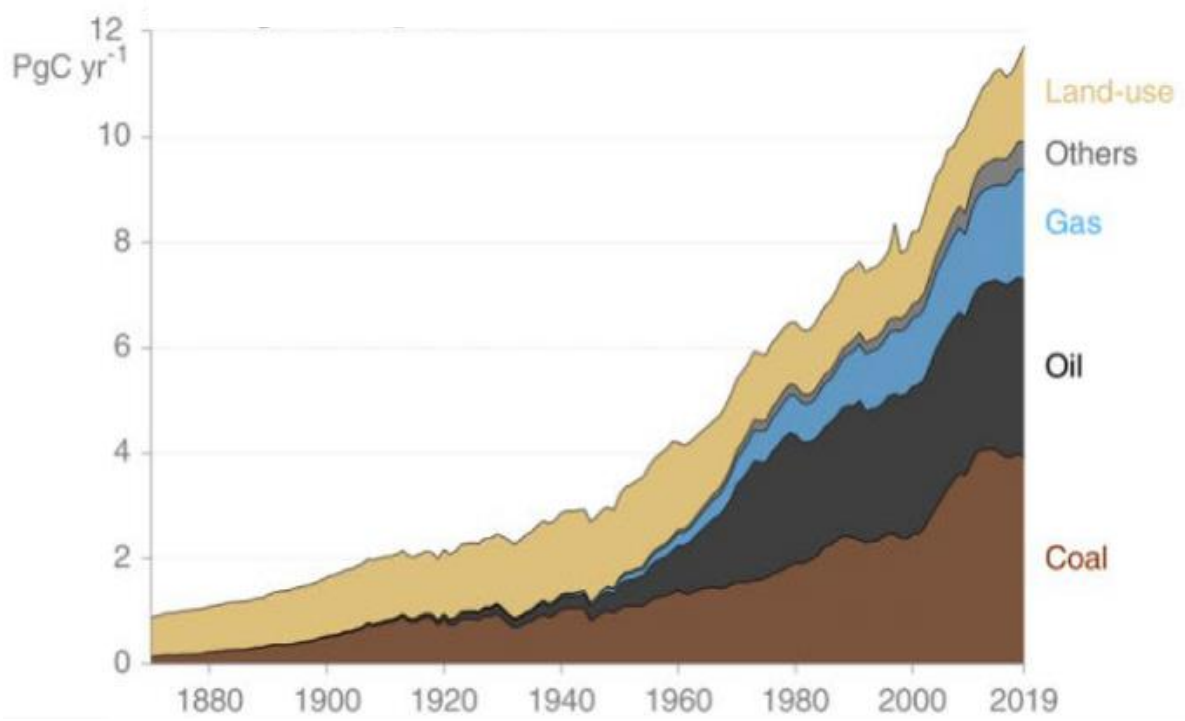

Figure 1.1. Annual global CO_2 emission. (IPCC, 2021, Figure 5.5)

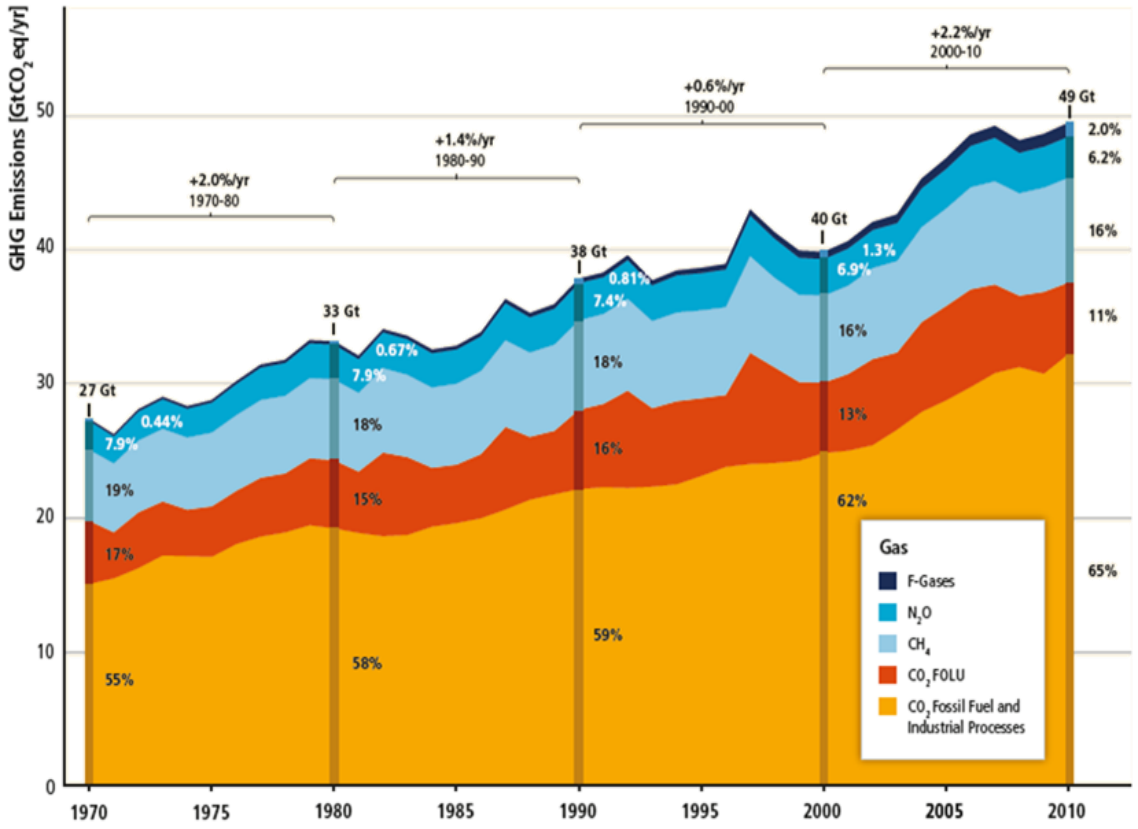

Figure 1.2. Total annual anthropogenic GHG emissions by group of gases 1970-2010. (IPCC, 2013, fig.SPM.2)

These gases, when mixed with the atmosphere, have the property to absorb specific electromagnetic waves. The sun's radiation, entering Earth's atmosphere, is roughly absorbed by half by the land surface; the rest is absorbed by the atmosphere or backscattered into space. The energy received on the land is partially re-emitted in Earth's atmosphere at shorter wavelengths which are captured, once again, by the gas molecules present in the atmosphere and converted into heat. This peculiarity, the presence of an atmosphere that blocks part of the radiation that would escape into the space, is a key problem: in fact, electromagnetic waves, once captured, are then converted into heat, and this phenomenon allows the conservation of a proper temperature suitable for the development of life processes. This mechanism has worked for billions of years and guaranteed an energy balance between incoming and exiting radiation with little or no modifications at all. In any case, the variation of the composition of the atmosphere has always been a slow process, leaving time for Earth's sub-systems to evolve as well as to adapt and also counterbalance with proper feedback mechanisms (Kweku et al., 2018).

Starting from the Industrial Revolution, the composition of the atmosphere has been perturbed by the massive introduction of the above-cited gases, which have brought, as a consequence, a strengthened capacity to stop radiations leaving Earth's atmosphere. This capacity, in particular, affects the radiative forcing, i.e. the energy flux density in W/m^2 of a certain perturbant species, that alters the Earth's energy balance.

Since the Industrial Revolution, the radiative forcing has increased, reaching in 2019 an estimation of about 2.72 W/m^2 (IPCC, 2021a).

From the evaluation of the radiative forcing, the scientific community has elaborated different trajectories of GHGs emissions which result, at the end of the century, in different increase of the radiative forcing active on Earth's balance.

These scenarios, different in terms of global emission reduction, result in the well-known Radiative Concentration Pathways (RCPs). The number following the RCP (e.g. 8.5 in RCP8.5) indicates the level of the radiative forcing reached at the end of the century, as shown in figure 1.3 (IPCC, 2014).

The immediate and tangible results of these modifications are the observed rising temperatures of the Earth's surface and low troposphere (IPCC, 2014)(fig. 1.4), responsible for many of the phenomena that are, commonly, included under the name of climate change.

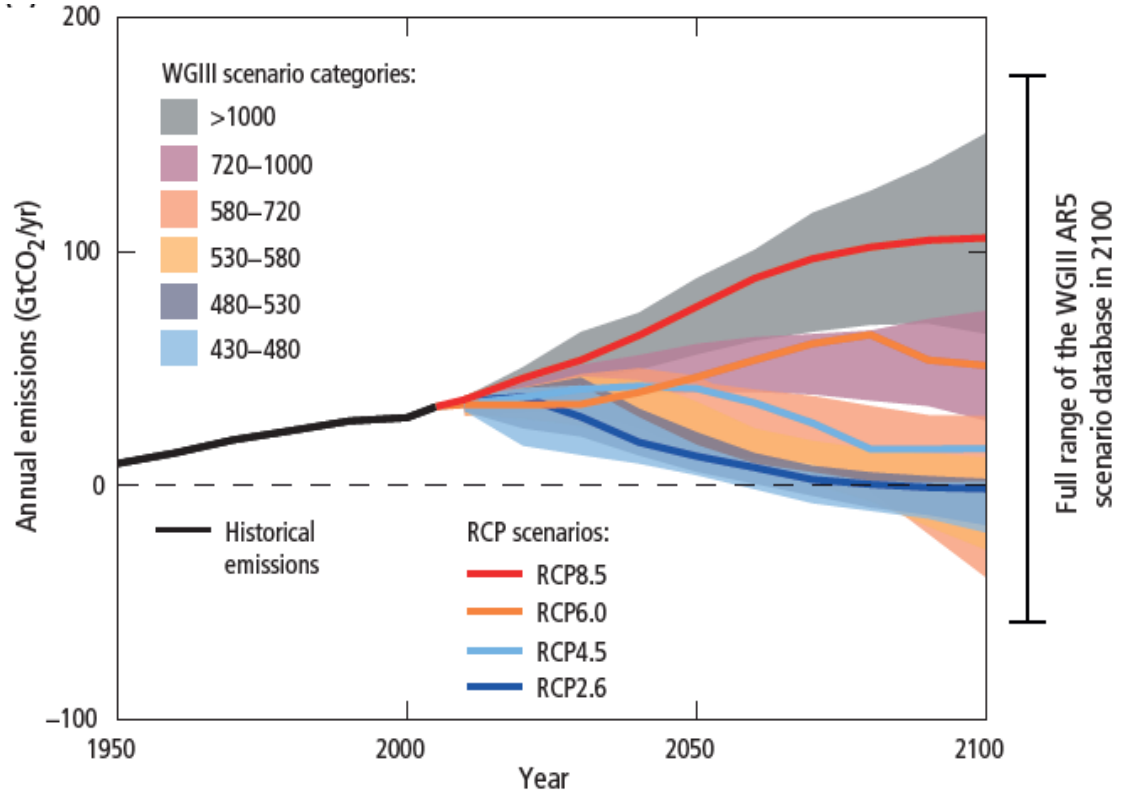

Figure 1.3. Annual anthropogenic CO_2 emission. (IPCC, 2013, fig. SPM 5a)

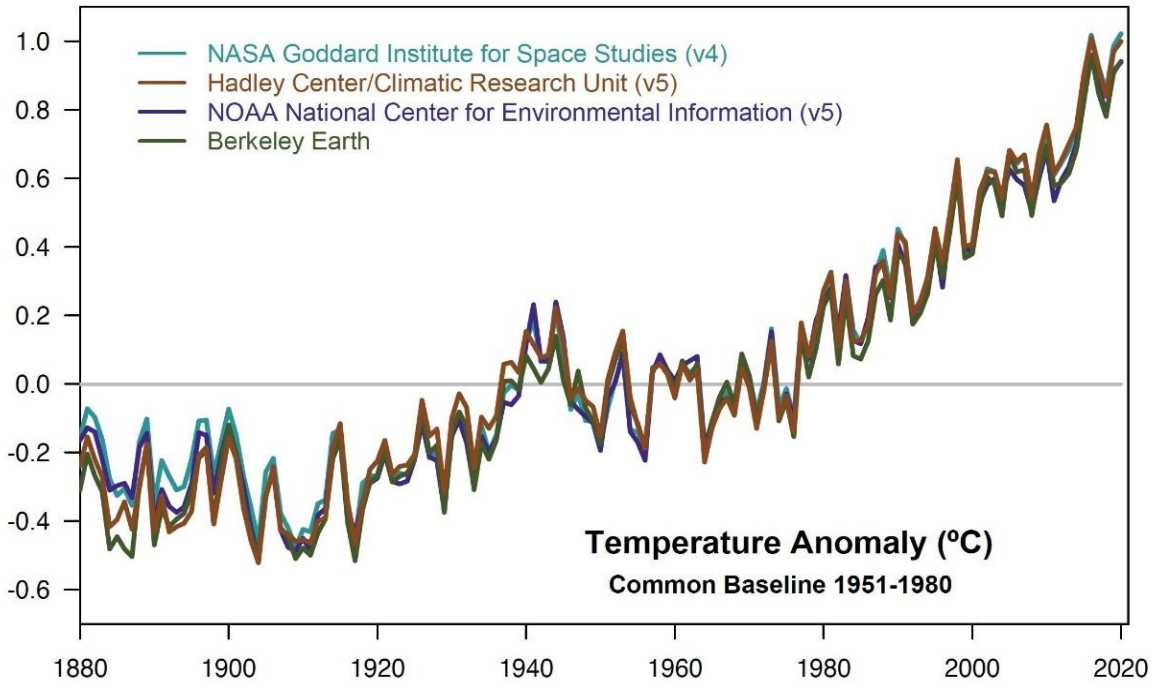

Figure 1.4. Global annual average surface air temperature anomalies (1961-1990), each trajectory represents a different institution. (NASA GISS/Gavin Schmidt)

1.2. Carbon emission rates and sinks

The Intergovernmental Panel for Climate Change (IPCC) is a supranational body of the United Nations established in 1988 which studies all the aspects related to climate change. It publishes, periodically, reports on the state of the art of scientific knowledge and, in addition, special focuses on critical aspects or suggested targets.

The most recent overall study, "sixth assessment report", has been published in 2021: following its schematization, it is possible to describe the carbon cycle in a system composed by atmosphere, land and ocean (IPCC, 2021b).

The average annual fluxes between these sectors are expressed, for different periods until the most recent one 2010-2019, in table 1.1. It is noteworthy that these data refer just to anthropogenic gases containing carbon (whereby, CO_2 and CH_4 , jointly, account for 92% of the overall GHGs emissions (*EPA*, 2021; IPCC, 2014).

Table 1.1. Cumulative (1750-2019) and decadal (1980-1989, 1990-1999, 2000-2009, 2010-2019) emission of C [Pg]. (IPCC, 2021)

	1750–2019 cumulative PgC	1980–1989 PgC yr^{-1}	1990–1999 PgC yr^{-1}	2000–2009 PgC yr^{-1}	2010–2019 PgC yr^{-1}
Emissions					
Fossil fuel contribution and cement production	445 ± 20	5.4 ± 0.3	6.3 ± 0.3	7.7 ± 0.4	9.4 ± 0.5
Net land use change	240 ± 70	1.3 ± 0.7	1.4 ± 0.7	1.4 ± 0.7	1.6 ± 0.7
Total emissions	685 ± 75	6.7 ± 0.8	7.7 ± 0.8	9.1 ± 0.8	10.9 ± 0.9
Partition					
Atmospheric increase	285 ± 5	3.4 ± 0.02	3.2 ± 0.02	4.1 ± 0.02	5.1 ± 0.02
Ocean sinks	170 ± 20	1.7 ± 0.4	2.0 ± 0.5	2.1 ± 0.5	2.5 ± 0.6
Terrestrial sink	230 ± 60	2.0 ± 0.7	2.6 ± 0.7	2.9 ± 0.8	3.4 ± 0.9

From table 1.1, it emerges that, roughly, more than half of the emission of C containing gases is absorbed by the Earth ecosystems at the end of the annual balance. From an average emission of 10.9 Pg (10.9 Gt) of carbon into the atmosphere, the net flux absorbed by the Earth surface results in 3.4 Pg and the amount captured by ocean turns out to be 2.5 Pg.

As shown by these data, the mass of the oceans plays a relevant role, not always perceived by laymen or even by experts, in counterbalancing human emissions. Seawater, overall, contributes to around 40% of the annual carbon absorption.

Without the ocean, the effects of climate change would have been much more severe than what has been experienced until now; this huge sink of carbon, in fact, is a resource that should be safeguarded like uncontaminated forests. Ocean atmosphere interactions, regulated through mechanisms that are now under a stress condition, are explained in section 1.7.

1.3. Carbon budget

With a continuous emission of GHGs and raising concentrations of CO_2 from 278 ppm in the pre-industrial period (Corinne Le Quéré et al., 2018) to the global monthly highest data, registered in 2020, featuring a record value of 413.9 ppm (*NOAA*, 2021), scientists and researchers tried to estimate a safety threshold that could guarantee an acceptable future scenario, limiting dangerous and harmful situations.

In 2013 Hansen et al. in "Assessing Dangerous Climate Change: Required Reduction of Carbon Emissions to Protect Young People, Future Generations and Nature" stated that a concentration of 350 ppm would be a safe limit (Hansen et al., 2013). This limit has already been overcome, so, in the study, different strategies have been analyzed to achieve this target and come back to a safe zone. The equilibrium is, as of today, reestablished within a couple of centuries or more, according to the emission stop date.

Complementary to this argument, different remaining carbon budgets have been estimated and refined, in order to evaluate the residual possibility of CO_2 emission useful to reach the target of 1.5-2 °C warming compared to the pre-industrial period.

The Fifth Assessment of the Intergovernmental Panel on Climate Change (2013) suggested that the cumulative emission of CO_2 should not exceed 2900 Gt since the start of the industrial era to limit the temperature increase below 2°C, with 1900 $GtCO_2$ already emitted in 2011 (IPCC, 2014).

In 2015, the historical Paris' Agreement marked an important milestone for the fight against climate change. During that conference, almost all countries recognized the urgency to take immediate actions and agreed to contribute with personal pledges to the case. This bottom-up approach, radically different from the Kyoto Protocol, was probably originated also from the partial failure of the 2009 Copenhagen summit. With the Paris' Agreement, each country

proposed a CO_2 cutting emission strategy based on its ranking as a worldwide emitter and according to its technological and social possibility.

Article 2 of the Agreement sets the temperature limit "*well below 2°C above pre-industrial levels*" with "*efforts to limit the temperature increase to 1.5°C*". This marked an enhanced commitment in the effort, highlighting the fact that scenarios over 2°C global warming would be destructive and re-marking the good suggestion to have an increase below 2°C. At the same conference, the UNFCC invited the IPCC to prepare a special report on 1.5°C global warming which was published in 2018.

In this document (IPCC SR 1.5°, 2018), it was concluded that there is a remaining budget of 580 $GtCO_2$ to limit the warming up to 1.5°C at 50% probability, whereas with a limit set to 420 $GtCO_2$ the probability is 66%.

With the current emission rates, that limit will be overcome within a decade (IPCC SR 1.5°, 2018) and may also be reduced considering not-related CO_2 gases (CH_4, SF_6 and halogen gases).

1.4. Emission reduction pathways and carbon dioxide removal technologies

To access the possibility of remaining below 2°C global warming, it is urgently necessary to lower the CO_2 emission with the aim to reach net-zero emissions by mid-century. However, not all the industrial sectors present an easy path towards total decarbonization, e.g. aviation, construction of buildings and infrastructure (Rayner, 2021). To overcome this limit, in the last 20 years there has been a growing interest in Carbon Dioxide Removal technologies, CDR. CDR, also called negative emission, are defined as *"intentional human efforts to remove CO_2 emissions from the atmosphere"* (Minx et al., 2018) and may help in providing carbon neutrality. By carbon neutrality, it is meant a condition where residual emissions are offset by natural or artificial absorption of CO_2 that is trapped instead of being re-emitted in the environment.

CDR technologies present two functions, depending on their effective implementation date and rate of use. If used before half of the century, they may neutralize the unabated CO_2 emissions, ensuring the respect of the remaining carbon budget and avoiding a temporary overshoot of 1.5°C global warming. Instead, if they are intensively deployed after the mid-century, provided that carbon neutrality has been already reached, their main role will be to obtain net negative emissions that will contribute to the re-establishment of lower CO_2 concentrations in the atmosphere (IPCC SR 1.5°, 2018).

Due to their relative immature stage of development and combined with the current emission rate of CO_2 and other GHGs, CDR techniques will be probably used to compensate a varying overshoot of temperature regarding global warming in the next decades.

Many CDR techniques are now under feasibility studies, and a correct mix of them may provide successful results.

An application of CDR technologies can be seen in the emissions' trajectories coming from the four Shared Socio economic Pathways, SSPs, towards 1.5°C global warming that were published in the 2018 IPCC special report, fig. 1.5. SSPs represent different regional scenarios that vary according to future socio-economic development, demographic growth, equity and level of cooperation among countries. In these scenarios, the only CDR technologies deployed are those gathered under the acronyms AFOLU, (Agriculture, Forestry and Other Land Use) and BECCS (Bioenergy with Carbon Capture and Storage).

AFOLU contains all practices linked to the management of forestry and soils, mainly afforestation, reforestation and Soil Carbon Sequestration, SCS, performed through various amendments or techniques that enable CO_2 absorption. BECCS couples bioenergy production with sequestration and storage of C-rich flue gases from biomass burning: in this way, trees and biomass, sequestrate CO_2 leading to a net negative emission.

The SSPs represented in Figure 1.5 follow different characteristics:

- scenario P1 is characterized by rapid decarbonization coupled with low energy demand
- scenario P2 has focused on sustainability, low carbon technology innovations with economic development and international cooperation
- scenario P3 presented social and technological developments following historical pattern, emission reduction is due to the changing methods for energy production
- scenario P4 is characterized by economic growth and globalization with high GHGs lifestyles.

From scenario P1 to scenario P4 the adoption of CDR techniques increases significantly.

The emission pathways' results of fig. 1.5 are elaborations coming from interpolations of Integrated Assessment Models, IAMs, that take as input the above cited SSPs and other assumptions, like energy production and land use. The IPCC SR1.5 chapter 2 says about IAMs: "*combine insights from various disciplines in a single framework, resulting in a dynamic description of the coupled energy–economy–land-climate system that cover the largest sources of anthropogenic greenhouse gas (GHG) emissions from different sectors*." (IPCC SR 1.5°, 2018)

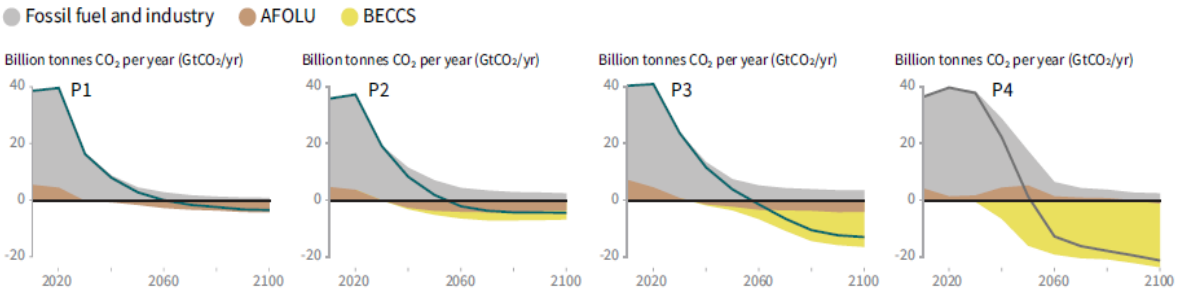

Figure 1.5. Breakdown of contributions to global net CO_2 emissions in the four SSPs. (IPCC, 2018, SPM 3b)

Each trajectory represents a different SSP and has a different approach towards decarbonization with raising effort to put in CDR techniques that are estimated in the order of 100-1000 $GtCO_2$ (IPCC SR 1.5°, 2018). These trajectories, even though they all respect the 1.5°C warming limit, include different limited overshoots in terms of rising temperatures.

Each CDR technology features pros and cons: a) for AFOLU, the main problems concern the decrease in the albedo reflectance, competition for land use and also the stability of stocked CO_2; b) afforestation requires careful management to limit fires and outbreaks of pest (Smith et al., 2016).

BECCS issues are the utilization of land, water consumption and open questions about CCS, mainly the search of suitable places where to practice it, the safety of the stored CO_2 and also the social impact.

Another CDR technique with prospective potential which is not considered in the SSPs, is ocean alkalinization. This technique does not present the above-mentioned problems, that are relatively manageable: its main limitations are the cost (Minx et al., 2018) which is directly linked to the energy required, higher than other CDR processes and potentially harmful effects for the marine biota (Gim et al., 2018).

Artificial Ocean Alkalinization belongs to the techniques under the name of Enhanced Weathering, EW. EW is part of the portfolio of solutions represented by CDR.

A final consideration regarding CDR is necessary: the deployment of CDR techniques will be unavoidable if the current emission pace continues in the next decades, however the extent of such utilization will mainly depend on the policies adopted for emission reduction.

Start decreasing CO_2 emissions in this decade is not certainly the least cost-effective choice, i.e. delaying abatement actions reduces the cost, as new efficient and powerful technologies will exist in the future. However, negative emissions are not consolidated technologies and the

effects of their unsuccessful development may be potentially destructive (Fuss et al., 2014; Minx et al., 2018).

Transferring all the choices to the future presents a double-sided risk. The first one is related to the real efficiency of those technologies: new studies to understand possible drawbacks or side effects may reduce the final efficacy. The second risk is an immediate effect of disincentivizing present virtuous actions, increasing the future CO_2 burden to remove. This may become harmful for the defined target of 1.5-2 °C global warming increase.

1.4.1 Ocean liming

Ocean liming is considered as part of EW techniques which comprehend all the processes that accelerate the weathering of certain minerals that, in the chemical reaction, trap CO_2 during degradation. Artificial Ocean Liming is not strictly a weathering process, but it is considered in this category.

Artificial Ocean Liming consists in spreading and dissolving in seawater different rock powder derivatives. This, among its benefits, entails the release of cations and increments the alkalinity. Hereby, we analyze only the dissolution of calcium hydroxide $Ca(OH)_2$, which reacts following the general equation (1). As written in (1) the dispersed $Ca(OH)_2$ reacts with the diluted CO_2 forming bicarbonates. This mechanism, in theory, sequesters 2 moles of CO_2 in the aqueous phase per each mole of calcium hydroxide dispersed. However, some competing reactions occur and lower the yield to 1.4-1.7 moles of captured CO_2 (Renforth, 2019; Renforth and Henderson, 2017).

$$Ca(OH)_2 + 2\,CO_2 \rightarrow Ca^{2+} + 2HCO_3^- \qquad (1)$$

Artificial Ocean Liming presents another advantage regarding sea and its equilibria: the reaction releases OH^- ions that react with positive H^+ ions, contrasting acidification. The alkalinity is increased as well, thanks to the formation of HCO_3^- ions.

As explained in section 1.7, (fig. 1.7), the pH rise tends to increase the concentration of CO_3^{2-} and to reduce the dissolved CO_2. Therefore, the reduction of CO_2 in water is readily compensated by the absorption of CO_2 from the air, causing net sequestration of carbon dioxide in order to find a new air-water surface equilibrium.

1.5. Desarc-Maresanus project

The research project Desarc-Maresanus (DEcreasing Seawater Acidification Removing Carbon, *www.desarc-maresanus.net*) was launched with two main objectives: 1) mitigate CO_2 emissions through ocean absorption and 2) counteract the acidification of the seas. For these purposes, it is planned to spread $Ca(OH)_2$ from the sterns of ships onto the surface of oceans. Once the calcium hydroxide has dissolved, the pH of the sea is increased and, in the meanwhile, CO_2 is removed from the atmosphere (Renforth et al., 2013).

The research is carried out at the Politecnico di Milano and the Euro-Mediterranean Center on Climate Change Foundation (CMCC), with the financial support of Amundi and the collaboration of CO2APPS.

The process is protected by a patent (Cappello and Ross Morrey, 2018) and combines proven industry practices with the technology currently under study.

After a simplified scheme shown in figure 1.6, the phases of the process are then explained, based on the works report in Caserini et al., and Campo et al., 2020 (Campo et al., 2020; Caserini et al., 2019).

To increase the pH and the ocean capacity to absorb CO_2, $Ca(OH)_2$ is essential, for the overall process of production is required energy. The project process aims to produce it, generating the lowest impact in term of anthropogenic CO_2 emitted.

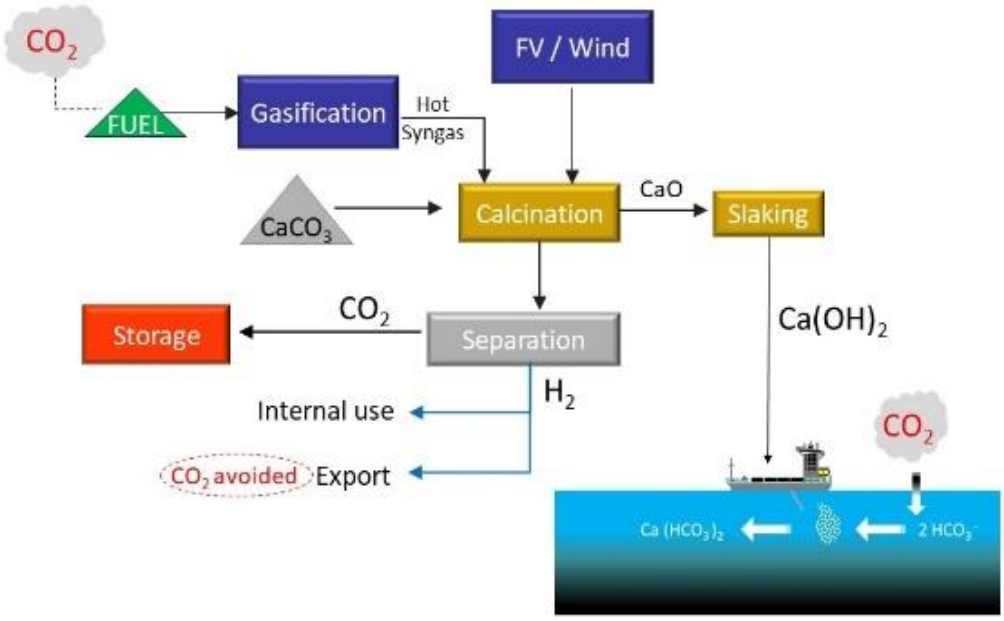

Figure 1.6. Conceptual scheme of the project Desarc-Maresanus. (www.desarc-maresanus.net)

1.5.1. Biomass gasification

The first phase of the process is the gasification of biomass. Gasification is a chemical process that converts a material containing carbon into gas. The gas produced is called synthetic gas, or syngas, and is composed mainly by hydrogen (H_2), carbon monoxide (CO), carbon dioxide (CO_2), methane (CH_4), nitrogen (N_2). The percentage and composition of the gases depends on the type of gasifier, the gasifying agent, the material used, and the process parameters (Baláš et al., 2017; Couto et al., 2013). This gas mixture is obtained providing heat to the solid materials in controlled condition of oxygen or steam, without combustion. The syngas is a combustible fuel. The gasification is also applicable to a range of solid combustibles, like coal or SRF (Solid Recovered Fuel) (Bell et al., 2010; Vonk et al., 2019). However, choosing biomass as fuel allows maximizing the effect of negative emission of the overall process if combined with carbon storage; because, during its growth, the biomass, has sequestered carbon from the atmosphere.

1.5.2. Calcination and production of slaked lime

The second phase of the process is the calcination and the production of $Ca(OH)_2$. The reaction of calcination is endothermic (standard enthalpy of reaction $\Delta H°_r$ = 178.5 kJ/mol, 25°C and 1 atm, NIST Chemistry WebBook), thus heat is necessary to realize it, eq. 2.

$$CaCO_3 + heat \rightarrow CaO + CO_2 \qquad (2)$$

The syngas, after the gasification phase, has a temperature exceeding 1 000 °C and provides heat for the above-cited reaction through a heat exchanger. To produce calcium hydroxide, the lime produced is used in equation 3, by adding water:

$$CaO + H_2O \rightarrow Ca(OH)_2 + heat \qquad (3)$$

The reaction is exothermal (standard enthalpy of reaction $\Delta H°_r$ =-65.3 kJ/mol, 25°C and 1 atm, NIST Chemistry WebBook), and the heat generated can be used by a heat recovery steam generator (HRSG) to supply steam in the first phase of the process.

1.5.3. $Ca(OH)_2$ spreading and dissolution

Ocean liming, or ocean alkalinization, is a process that adds alkalinity to ocean's water. Alkalinity is added through the dissolution of slaked lime ($Ca(OH)_2$) in seawater (Renforth et al., 2013), better explained in section 1.4.1, commonly following reaction 4.

$$Ca(OH)_2 + 2CO_2 \rightarrow Ca^{2+} + 2HCO_3^- \qquad (4)$$

The addition of slaked lime has a double positive effect: 1) it enables CO_2 to be absorbed from the atmosphere into the ocean; 2) helps to counteract the acidification of the sea caused by the natural uptake of atmospheric carbon (section 1.7).

In order to spread slaked lime over the sea, dedicated or cargo ships can be used, discharging it in the wake (Renforth et al., 2013).

1.5.4. Water gas shift reforming and CO_2 separation

The scope of this phase is to separate CO_2 from other gases, like H_2, CH_4 or CO. There are different technologies for this purpose based on pressure swing adsorption (Chou et al., 2013) or membranes (MTR-Membranes, 2017). Moreover, the water gas shift reforming (WGSR) is necessary to convert CO in CO_2, by addiction of H_2O. This reaction leads to extra formation of H_2 (Smirniotis and Panagiotis, 2015).

1.5.5. CO_2 storage

A carbon storage technology is desirable for the project in order to increase the entire negative emissions effectiveness as a negative emissions process. Different methods are available to store carbon, a geological way can be applied using saline formation, exhaust gas or oil reservoir (Aminu et al., 2017), or performing confined storage in glass capsules on the seabed (Caserini et al., 2017).

Although areas in the world have different storage potentials, there is an overall large capacity of available sites all over the world, to permanently stock CO_2 underground (Fuss et al., 2018).

1.5.6. Other gaseous products of the process

The gases obtained from the separator, e.g. H_2 or N_2, can be used for different purposes. Hydrogen can be burnt in a turbine engine to cover the electricity demand of the system and generate a surplus, that can be sold to the national grid too. Alternatively, H_2 and N_2 can

compose anhydrous ammonia, using the Haber Bosch process. Anhydrous ammonia (NH_3) is a fuel of great interest for the transport sector (Zamfirescu and Dincer, 2009).

1.6. Results and future developments

Part of the research has been already done out to evaluate the necessities and pitfalls of each stage. A Life Cycle Assessment of the process was carried out, showing that the total negative benefit of CO_2 is 3.37 tons for each ton of biomass utilized (Campo et al., 2020; Campo, 2019). In addition, an analysis of the marine traffic data has been conducted to evaluate the potential of ocean alkalinization and future scenarios of spreading. It emerged that the Mediterranean Sea has a high potential for the spreading of calcium hydroxide, thanks to the high number of ships that navigate every day (Caserini et al., 2020).

Moreover, a preliminary model to describe the fluid dynamics of $Ca(OH)_2$ discharge in water was developed. A 3D non-reactive model and a 1D reactive model have been used to evaluate the evolution in time of concentration and the particles' radius. These models help to quantify the magnitude of perturbation of the pH. In particular, discharges of 10 or 100 kg/s of $Ca(OH)_2$ generate both a maximum pH increase of 1 unit for a few minutes, with different time distances of the peak for the two amounts (Caserini et al., 2021).

Different researches have been done on Desarc-Maresanus project and on ocean liming technique. Still, none studied the dissolution's dynamic, in sea-water, of $Ca(OH)_2$, one of the best promising compounds for this purpose.

1.7. Ocean CO_2 sequestration dynamics

The ocean-atmosphere dynamics is characterized by complex and multiple interactions. First of all, CO_2 is dissolved in water, following Henry's law, which states that the amount of dissolved gas in a liquid is proportional to its partial pressure above the liquid. Increasing the partial pressure of CO_2 in the atmosphere, by higher concentration of the same gas, leads to greater presence of CO_2 in the oceans.

The amount of carbon present in the ocean is much higher, however, than the value restituted by Henry's law, this is due to mechanisms that affect the chemical equilibrium of the oceans.

Reactions 5-6-7 represent the interaction between water and diluted CO_2, which forms carbonic acid (eq. 5), a weak acid that dissociates into bicarbonate ions and H^+ ions (eq. 6). The bicarbonate, in turn, dissociates into carbonate and H^+ (eq. 7). The presence of carbonates and

mainly bicarbonates explains the reason why the ocean is actually able to store more carbon. These species, moreover, are negatively charged and cannot evaporate such as CO_2.

$$CO_{2\,(aq)} + H_2O_{(aq)} \leftrightharpoons H_2CO_3 \quad (5)$$

$$H_2CO_3 \leftrightharpoons H^+ + HCO_3^- \quad (6)$$

$$HCO_3^- \leftrightharpoons H^+ + CO_3^{2-} \quad (7)$$

The predominant species among these reactions are the bicarbonates, present in much higher concentrations and less susceptible to variations, fig. 1.7 (Logan, 2010).

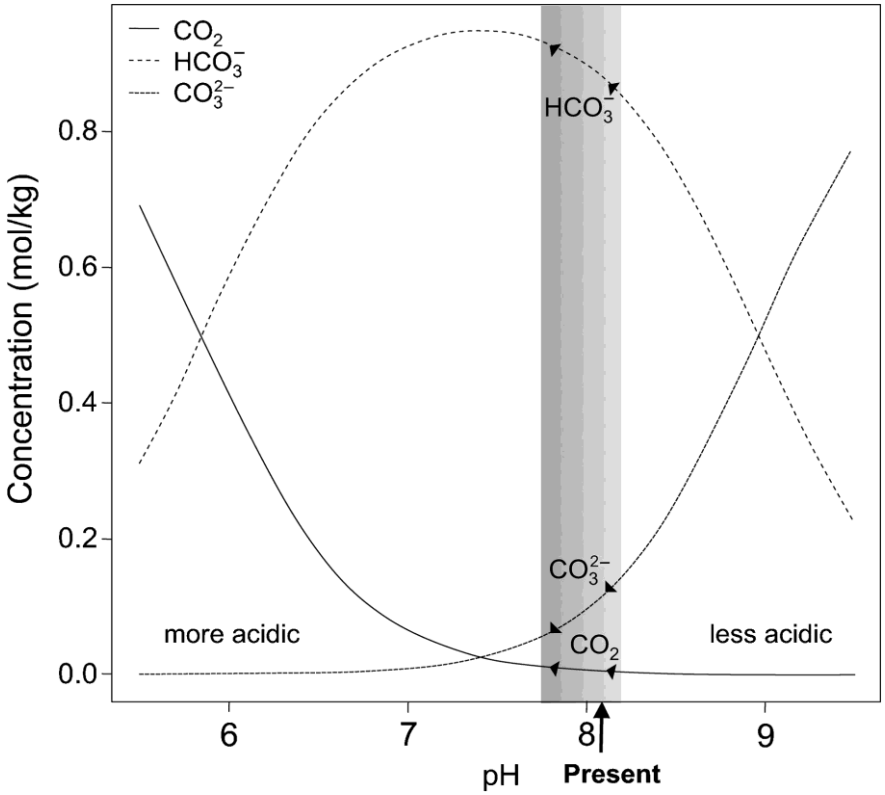

Figure 1.7. Diagram of species (HCO_3^-, CO_2, CO_3^{--}) present in the seawater (Logan, 2010).

At this point, an equilibrium between the above-cited species occurs (eq. 8): adding diluted CO_2 moves the reactions towards the right, causing the carbonates to become the limiting factor and thus reducing the efficiency of the ocean to absorb CO_2.

$$CO_{2-d} + H_2O + CO_3^{2-} \leftrightharpoons 2HCO_3^- \quad (8)$$

Here a little clarification on biological effects is needed: by adding CO_2 in a diluted form, it is possible to see, both from the equations 5-6-7-8 and also from the graph, that the pH of the sea is strictly connected to these processes: in particular, the formation of carbonic acid that dissociates is responsible for the increasing amount of H^+ ions, that accounts for the reduction of the pH. The problem of ocean acidification is one of the most known even for the general public opinion, leading to very serious environmental issues like coral bleaching and diminishing the activity and proliferation of calcifying organisms (IPCC, 2014).

1.8. Previous works regarding $Ca(OH)_2$ dissolution

There are no extensive researches of dissolution of $Ca(OH)_2$ in seawater, while different scientific articles have been published discussing dissolution in freshwater.

In Giles et al. (1993), starting from their previous studies on calcium oxide, the authors investigated the dynamics of dissolution in freshwater and estimated a rate of dissolution both for powdered and disc-compressed $Ca(OH)_2$, following a form of eq. 9.

The experiments on the disks are conducted by means of compressed calcium hydroxide disks spinning in different aqueous solutions under a controlled atmosphere, no exchange of CO_2 is allowed. The conductivity is registered in continuous, while calcium concentration is monitored by Atomic Absorption Spectrophotometry by means of samples extracted at intervals. The experiments demonstrate that, at a low rotating speed below 275 rpm, the reaction is diffusion-controlled: the dissolution of calcium hydroxide is function of the rate of removing the ions of Ca^{2+} and OH^- away from the surface into the solution eq. 10. At low rotating speed, calcium hydroxide re-deposits in the form of crystals on the disk, slowing the reaction. At higher rotating speeds, the reaction becomes chemically controlled, and the reason is that these crystals are reduced as speed is increased, fig.1.8.

$$Ca(OH)_2 \rightarrow Ca^{2+} + 2OH^- \quad (9)$$

$$Ca^{2+} + 2OH^-(surface) \rightarrow Ca^{2+} + 2OH^-(bulk\ solution) \quad (10)$$

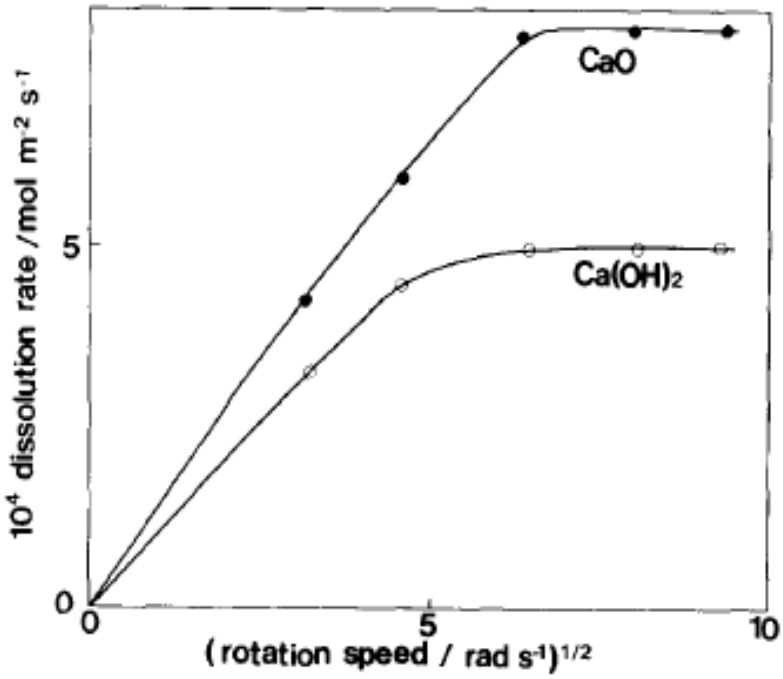

Figure 1.8. Plot of the rate constant at 25°C against the square root of the rotation speed of CaO discs and $Ca(OH)_2$ discs. (Giles et al. (1993))

Concerning the temperature, they demonstrated the direct dependence of the dissolution constant for the disks.

For powder, instead, the theory of dissolution of the shrinking core model is adopted and the rate constant is estimated through calorimetric measurements.

Following this approach, Wang et al. (1998) investigated the dissolution rate of SL in freshwater controlling the variables involved in the process of dissolution of calcium hydroxide.

They replicated the spinning disk of Giles et al. paying attention to minimize the active area of the disk and the permeability of the solid, allowing the dissolved ions to be maintained in the solution. The main difference concerns the addition of a titration pump that injects HCl acid each time the solution reaches a fixed upper limit of pH; the operative scheme is shown in fig. 1.9.

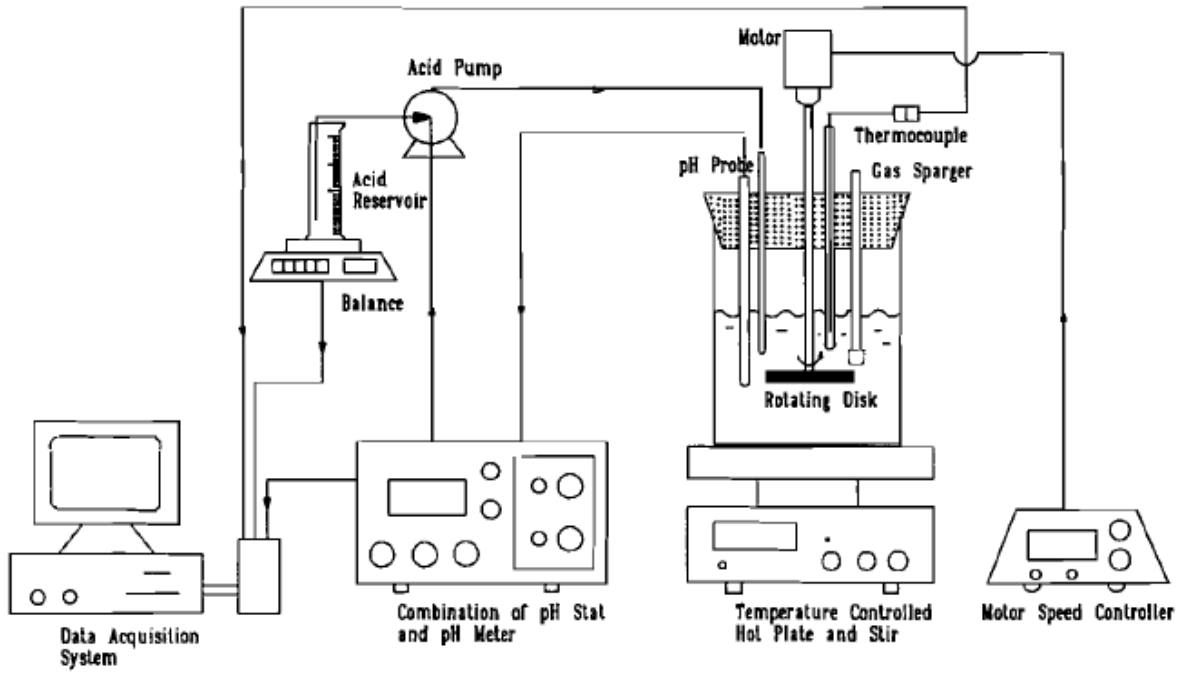

Figure 1.9. Technical scheme of the equipment employed by Wang et al. (Wang et al., (1998))

With this compound it is possible to estimate first, by linear regression, a couple of functions regarding the acid consumption, (eq. 11) and the dissolution of the sorbent, (eq. 12) and to investigate the relationship with temperature, pH and spinning velocity.

$$Acid\ consumption\ rate = N = \frac{L \cdot C_{acid}}{60 \cdot 10^3 \cdot \rho} \qquad (11)$$

$$Sorbent\ dissolution\ rate = N_s = \frac{L \cdot C_{acid} \cdot d \cdot 10^{-8}}{6 \cdot S_{BET} \cdot W_s \cdot \rho} \qquad (12)$$

where:

L (g/min) = $\Delta W / \Delta t$ is the acid solution consumption rate

ΔW is the acid weight change

Δt is the time change

C_{acid} (mol/L) is the acid concentration

W_s (g) is the initial weight of the sorbent (slaked lime)

S_{BET} (m^2/g) is the surface area of the sorbent

ρ (g/cm^3) is the density of the acid solution (dilute acid density is assumed to be the same of water)

d is the sorbent/acid complete reaction molar ratio

They confirmed the change in the behaviour of the dissolution mechanism as a function of the rotation speed: the dissolution is linear up to the value of 300 rpm while, above this speed, it becomes independent from the rotational speed.

Coupling all this information, leads to the formulation of a dissolution expression for $Ca(OH)_2$ either in terms typical of hydraulics, eq. 13, until the Reynolds number of the spinning disk remains below 10^4, or with a more conventional formula, eq 17.

Regarding eq. 13-14, it's important to notice that the Sherwood number includes the dissolution rate expressed in a dimensionless form

$$Sh = 0.62\, Re^{1/2}\, Sc^{1/3} \tag{13}$$

Where:

$$Sh = Sherwood\ Number = {k \cdot d}/{D} = {N_s}/{D \cdot c_{sat}} \tag{14}$$

$$Re = Reynolds\ Number = (d^2 \cdot {\omega}/{v})^{1/2} \tag{15}$$

$$Sc = Schmidt\ Number = ({v}/{D})^{1/3} \tag{16}$$

and:

k is the mass transfer coefficient (cm/s)

v is the kinematic viscosity of water (cm/s)

D is the solute diffusion coefficient in water (cm^2/s)

d is the disk diameter (cm)

ω is the angular velocity of the disk (1/s)

c_{sat} is the saturation concentration of the solute (mol/cm^3)

$$ln(N_s) = -17.68 - 280\left({1}/{T}\right) - 0.105(pH) + 0.458\, ln\,(\omega) \tag{17}$$

Where:

T is the temperature over the range of 298 - 323 K

pH is for the range of 4.0 – 7.0

ω is the disc rpm, for $Re \leq 10^4$

Another promising field of research comes from the shale-oil industry and its wastes that are produced by the energy sector. These wastes are largely composed of calcium-rich minerals that may be separated and re-utilized.

Tamm et al., (2016), starting from three real different types of residues-ashes, *circulating fluidized bed (CFB), pulverized firing (PF),* and *solid heat carrier (SHC),* tried to replicate in laboratory the composition using just three main components: pure $Ca(OH)_2$, $CaSO_4 \cdot 2H_2O$ and CaS. They obtained good matching with the measurements of pH and conductivity in their water leachates after three hours of stirring. Then, through a model (*HsC Chemistry® 7.1 and Aspen Plus V8.6*), the equilibrium constants are obtained for dissolution reactions of the above-cited minerals. The value obtained for a common equation like eq. 18 is $4.28*10^{-5}$ mol/l.
In equation 18, from basic chemistry knowledge, the final value of the equilibrium constant K_{eq}, is the result of two opposing kinetic reactions. The reaction rate constant: k_1 [s^{-1}] accounts for the kinetic forward reaction (calcium hydroxide is transformed into ions) while k_2 [s^{-1}] for the kinetic backward reaction, products are re-transformed into reactant.

$$[Ca(OH)_2] \underset{k_2}{\overset{k_1}{\rightleftarrows}} [Ca^{2+}] + 2[OH^-] \qquad (18)$$

The relationship between dissolved calcium ions and conductivity was also investigated, and the result is eq. 19. Eq. 19 is calculated with the solutions kept at 25 °C and it is valid for all the three ash-residues replicated artificially (CFB, PF and SHC).

$$[Ca^{2+}] = 0.003375 \cdot E \qquad (19)$$

where:
Ca^{2+} is the concentration of the calcium ions (mol/l)
E is the system conductivity (mS/cm)

The part of the dissolution kinetics is set monitoring pH and conductivity in continuous after the release of the powder mixture in a batch reactor containing distilled water. The solution is kept in a close system for one hour at 25 °C under agitation. The resulting suspensions are filtered and the concentrations of calcium ions [Ca^{2+}] and total alkalinity are obtained by means of titration

The experimental data are compared with the modelling results performed with MODEST 6.1, a package of the software FORTRAN. Furthermore, it is determined the leaching kinetics of the calcium hydroxide, reporting the coefficients in eq. 20.

$$\frac{d[Ca(OH)_2]}{dt} = -k_1[Ca(OH)_2] + \frac{k_1}{K_{eq}}[Ca(OH)_2][Ca^{2+}][OH^-]^2 \qquad (20)$$

Expanding this branch, in another work (Uibu et al., 2015) a model for the dissolution kinetics of $Ca(OH)_2$ was refined. First of all, it was decided to model it with two different approaches: a double step reaction system, eq. 21 and 22 or a single step one, eq. 23.

$$Ca(OH)_2 \leftrightharpoons CaOH^+ + OH^- \qquad (21)$$

$$CaOH^+ \leftrightharpoons Ca^{2+} + OH^- \qquad (22)$$

$$Ca(OH)_2 \leftrightharpoons Ca^{2+} + 2OH^- \qquad (23)$$

Each equation is regulated by an equilibrium constant, suppose K_1, K_2, K_1^*, in which the activity coefficients γ_i accounts for the non-ideality of these electrolyte solutions, eq. 24, 25 and 26.

$$K_1 = [CaOH^+]\,\gamma_{CaOH^+}[OH^-]\,\gamma_{OH^-} \qquad (24)$$

$$K_2 = \frac{[Ca^{2+}]\,\gamma_{Ca^{2+}}[OH^-]\,\gamma_{OH^-}}{[CaOH^+]\,\gamma_{CaOH^+}} \qquad (25)$$

$$K_1^* = [Ca^{2+}]_{total}[OH^-]^2_{total} \qquad (26)$$

For both models, using the Pitzer model embedded in the *Aspen Plus* platform, by means of an estimation of the Gibbs' free energy, both the species in the solution and thermodynamic equilibrium constants (K_1, K_2, K_1^*) are calculated.

Starting from experimental data (measurements of pH and OH^- ions at different concentrations of $Ca(OH)_2$), the model, composed of first-order differential equations of the same appearance of eq. 20 is constructed, in which the activity coefficient of each ion is calculated using Debye–Hückel equation (eq. 27).

$$log\gamma_i = -\frac{0.51\, z_i^2\, \sqrt{I}}{1 + 3.3\, d_i \sqrt{I}} \qquad (27)$$

Where:

γ_i is activity coefficient of species *i*

d_i is the effective diameter of the hydrated ion (nm)

z_i is the charge on species *i*

I is the ionic strength of the solution.

The results show that for dilute solutions, the single-step model is more accurate, while, when saturation is approaching, the share of $CaOH^+$ and its effect on $Ca(OH)_2$ dissolution kinetics becomes more relevant; thus the double step is more precise.

Johannsen and Rademacher (1999) modeled the dissolution of calcium hydroxide through the concept of the net rate of dissolution, which includes, in his extended form, a relationship with the surface area, eq. 28-29.

$$Net\ rate\ of\ dissolution = R = k_f - k_b \cdot a(Ca^{2+}) \cdot a^2(OH^-) \qquad (28)$$

$$R = \frac{d_c(Ca)_T}{A \cdot d_t} = k_f - k_b \cdot c(Ca^{2+}) \cdot f^4 \cdot c^2(OH^-) \cdot f^2 \qquad (29)$$

Where:

a is the activity of the ions

k is the backward (k_b) and forward (k_f) reaction

c is the concentrations in mol/l

f is the activity coefficient

A is the total surface of the $Ca(OH)_2$ particles.

The activity coefficient f is calculated by means of a modified Debye–Hückel equation (eq. 30) where I is the ionic strength, while all the parameters about the surface area and diameter of particles are the results of a laser scattering measurements.

$$lg\, f = \frac{-0.5 \cdot \sqrt{I}}{1 + 1.4 \cdot \sqrt{I}} \qquad (30)$$

Using an iterative procedure and the data from batch experiments, all the parameters above are estimated, including the rates of the forward and backward reaction. It is proved that, during the time of an experiment, the rate remains constant, while, in different tests, a dependence is observed on the temperature, on the dosage of $Ca(OH)_2$ and on the dimension of the particles. In particular, the dissolution rate increases with the temperature.
The amount of calcium hydroxide released acts just on the backward rate of the reaction inhibiting it while it emerges that the major factor influencing the dissolution of particles is their diameter.

One of the few studies on $Ca(OH)_2$ dissolution in seawater was conducted by Sá and Boyd, 2017. With the work, the authors wanted to explore the effective benefits of aquaculture by means of adding of calcium hydroxide in seawater. Lime is often applied in shrimps pond to control the phytoplankton abundance, to remove CO_2 at the bottom of the ponds and stabilize the pH. The test consists of four groups of water, 2 liters each one, receiving a different amount of $Ca(OH)_2$ powder. The water employed was obtained from Gulfshores, AL, USA, and presented the following specifics: salinity 31.7 g/L, pH 8.12 and total alkalinity 109.1 mg/L. Four groups, six replicates for each one, receive respectively: 0, 0.0117 (low), 0.0251 (medium) and 0.0756 (high) g/L of $Ca(OH)_2$ powder. Each flask is stirred manually for 10 seconds after the application of as $Ca(OH)_2$, and 30 minutes before all the pH readings. The pH of water is determined before the adding of $Ca(OH)_2$ and at 1, 7, 24 hours afterwards, and after 2, 3, 6, 7, 9 and 10 days. Figure 1.10 shows the results obtained.

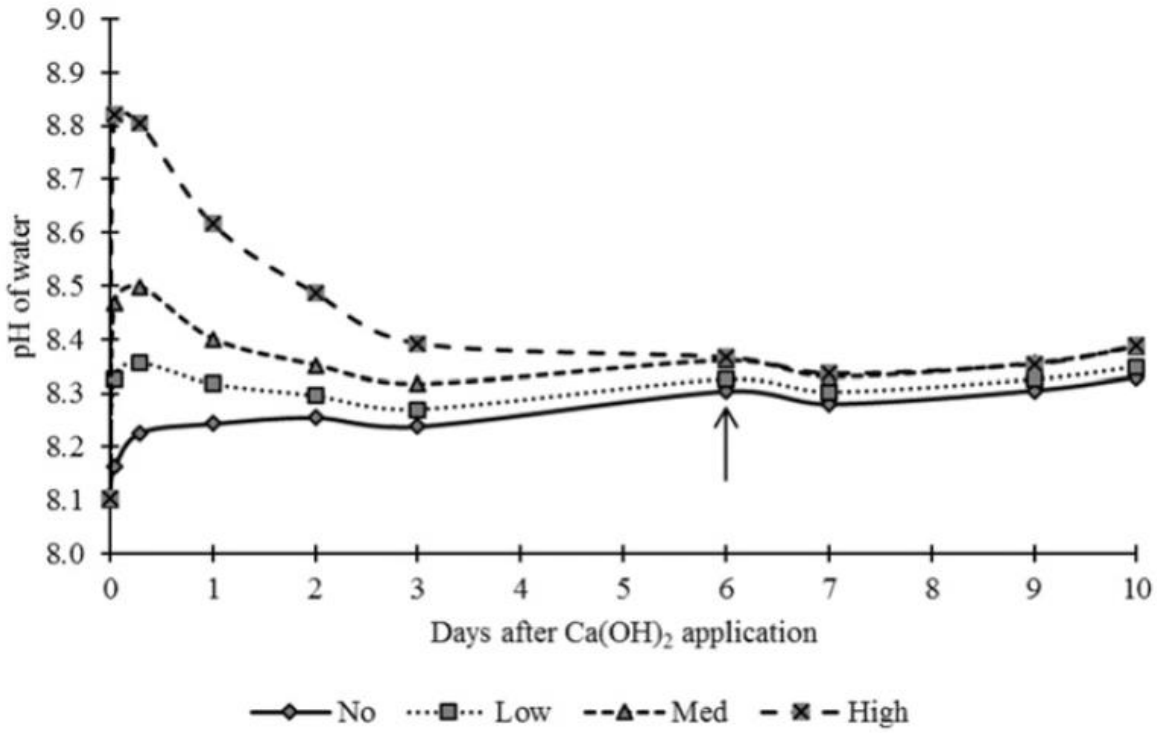

Figure 1.10. Evolution in time of pH after $Ca(OH)_2$ spreading. The trajectory with circles represents the control water, the squares the application of 0.0117 g/L, triangles of 0.0251 and crosses of 0.0756 g/L. The arrow is the point where the variations of pH among curves are no more significative (P > 0.05). (Sà and Boyd, 2017).

In the high and medium concentrations flasks, the pH of seawater decreases progressively over time while pH remains almost constant at the low-rate. In the control flasks, there is a slight increase in pH. The differences between trajectories are not statistically significant after 6 days. It is estimated a linear relationship between the pH rise after 1 hour and the application rate of $Ca(OH)_2$, eq. 31

$$y = 0.0081 \cdot x + 0.097 \qquad (31)$$

Where:

y is the pH increase after one hour

x is the amount of calcium ions concentration in mg/L.

1.9. Aim of the study

The purpose of this research is to study the dissolution of $Ca(OH)_2$ in seawater, and provide information and observations for the development of the Desarc-Maresanus project. To understand the dynamics of dissolution of calcium hydroxide, specific parameters were changed to understand their influence on the monitored variables. The variables are pH, conductivity, Ca^{2+} ions concentration, alkalinity, precipitated matter in the solution. Instead, the parameters are: temperature, salinity, level of mixing (influenced by the stirring), form of the $Ca(OH)_2$, (slurry or powder).

The objective is to gather data in a controlled and monitorable environment and use them in various branches of the project Desarc-Maresanus. The first application is the development a model able to reproduce the kinetics of dissolution of $Ca(OH)_2$. Understanding the mechanisms of dissolution is fundamental because it enables to pinpoint those variables that are relevant in the process and permits to have an accurate representation in time of what is happening.

In addition, these data will also be employed to check the correspondence with other models that reconstruct the phenomena of diffusion and mixing of $Ca(OH)_2$ in 3D space.

The collected information on dissolution will also be an essential requirement for the future upscaling of the project. The massive release of OH^- ions derived by the dissolution of $Ca(OH)_2$ in seawater raises the pH in the vicinity of the source. Estimating the magnitude and the evolution in time of the perturbation could help researchers to study whether and how the marine biota will react in the presence of high basicity of the water. Starting from this research, further works could assess the amount of stocked CO_2, providing another piece of information for the future endorsement of the project and, in general, on the necessity and the effectiveness of the CDR technologies.

Finally, from the economic point of view, determining the correct amount of $Ca(OH)_2$ to spread is a key aspect to maximize the results and minimize the cost, relevant when considering negative emission technologies.

2. Materials and methods

To measure the kinetics of dissolution of $Ca(OH)_2$, it has been necessary to carry out multiple experiments in the laboratory: different variables were changed to understand their effect, like temperature, salinity, amount and form of the calcium hydroxide dissolved, agitation speed.

The "classical" experiment was carried out starting with synthetic seawater in the beaker, under agitation, followed by $Ca(OH)_2$ addition. During this process, the temperature, the pH, and the conductivity of the solution were measured. For the container of the reaction, a beaker of 2 L of volume was used, containing 1 or 2 liters of seawater.

As shown in fig. 2.1, two electrodes were soaked in the solution, one for pH and the other one for conductivity. Thanks to these two electrodes the variables of the reaction were monitored in continuous with the possibility to store the measures every second.

A third calcium ion sensitive sensor was used to monitor the concentration of calcium ions in the solution. No data concerning this sensor are shown, because, since the beginning of the experiments, uncertainty about data arose (the theoretical value of the Ca^{2+} ions in seawater differed from the measurement effectuated by the instrument). Moreover, the membrane of the head of the sensor degraded quickly, causing non-reproducible measurements.

Figure 2.1. The solution, seawater with $Ca(OH)_2$ diluted, under agitation monitoring values through pH-meter and conductivity sensor.

To enhance the dissolution and simulate the wake of a cargo ship, the experiments were under agitation. This can be performed with a rotating stir on the bottom of the beaker (moved by an externally rotating magnet) or otherwise by a rotor mechanically activated.

2.1. Seawater

For most of the experiments, a synthetic seawater made in the laboratory was used, following the recipe in tab. 2.1, (Roy et al., 1993). The seawater used was made mixing pure water of grade 2 with the salts shown in tab. 2.1, the water of grade 2 was produced by *Millipore Elix 5* from tap water (for the sake of simplicity, from here on it will be called distilled water). The manufacturing of the salt indicated a specific purity for each product: for $MgCl_2$-$6H_2O$ an assay of 98.0-101.0%, KCl 99-101%, $CaCl_2$ >94%, Na_2SO_4 >99% and NaCl > 99.9%. To measure the quantity of salt, a precision balance with a readability of 0.01 grams has been employed, after weighting, the salts were put in a beaker with distilled water and dissolved through a magnetic stirring. Mixing was performed for a variable time of about 15 minutes, until there was no visible salt particle in suspension. Hereafter, the water was stored in a closed HD-PE tank of 20 litres.

For the preparation of the synthetic seawater $MgCl_2$-$6H_2O$ was used instead of $MgCl_2$ anhydrous (which is not easily available). This required some calculation in order to take into account the water content in the salt. For the preparation of 1 kg of solution 0.052 moles of $MgCl_2$ were requested, this quantity brought with it 0.316 moles of water (six times the moles of $MgCl_2$), for a total quota of 5.703 grams of contained water that have to be subtracted to the overall quantity of distilled water to add.

By means of simple calculations, starting from the molarity of Roy et al., the molality has been calculated, reported in tab. 2.2. By looking at the original molality (Roy et al., 1993), third column tab. 2.1, differences appeared at the 5^{th} decimal digit, below the lower detectable limit of the scale.

Table 2.1. Chemical composition [mol/kg] and molality of synthetic seawater. (Roy et al., 1993)

Salt	**[mol/kg of solution] (Roy et al., 1993)**	**Molality [mol/kg of distilled H_2O] (Roy et al., 1993)**
NaCl	0.413	0.428
Na_2SO_4	0.028	0.029
KCl	0.010	0.011
$MgCl_2$ anhydrous	0.053	0.055
$CaCl_2$	0.010	0.011

Table 2.2. Chemical composition of synthetic seawater used in the experiments; the third column reports the molality for each salt.

Salt	**Molecular mass [g/mol]**	**Molality [mol/kg of distilled H_2O] (Obtained by calculation)**	**Mass [g/kg of solution]**
NaCl	58.443	0.428	24.113
Na_2SO_4	142.040	0.029	4.011
KCl	74.551	0.011	0.761
$MgCl_2$	95.211	0.055	5.029
$CaCl_2$	110.984	0.011	1.151
$MgCl_2 * 6H_2O$	203.205		11.122

Using the calculated molality of anhydrous $MgCl_2$ (0.05473 moles per kg of H_2O) and the molar mass of $MgCl_2$ hydrated, it was easily found the total amount of hydrated salt requested. For all these calculations the density of distilled water was considered equal to 1 000 kg/m^3, introducing an error, due to the temperature dependence, that oscillated between 2 and 5‰, (Tilton and Leroy, 1922).

This approximation was evaluated as acceptable due to multiple reasons: a) the cylinder used to calculate a liter of water had a sensibility of some milliliters, it was not possible to weight each time a quantity of 1 kg on the technical balance but also, most importantly, b) without, for most of the experiments, a temperature control, the density varied each time.

An important parameter of seawater is the salinity, that express the dissolved salts in a given solution, to define it, is often used the PSU (Practical Salinity Unit). The PSU, useful when the seawater is collected as sample and the mass of salts are unknown, is determined by measuring the electrical conductivity ratio between the seawater sample to a potassium chloride solution (32.4356 g of KCl in 1 kg of solution) at 15°C and atmospheric pressure (Bradshaw and Schleicher, 1980; Millero, 2007).

An equivalent way to express salinity, easier when the mass of salts is known, is through eq. 32:

$$Salinity\ [‰] = \frac{g\ of\ dissolved\ salts}{kg\ of\ solution} \qquad (32)$$

Preparing the seawater in laboratory, the mass of salts was well known and was possible to calculate the salinity. The water used for the experiment had a salinity of 35‰ (or 35 ppt).

The obtained value was in the range of the salinity of Atlantic ocean, as shown in fig. 2.2 (Surface salinity in the Atlantic Ocean (30°S–50°N) (Reverdin et al., 2007), considering the upper part of 3-15 metres of depth.

The Mediterranean Sea, instead, features a salinity in the range 36.6-39.4‰ at 10 meters depth (Brasseur et al., 1996). Very low levels of salinity are observed in the Baltic Sea, where the value of 10‰ is never exceeded (Janssen et al., 1999). In the results' chapter, ch.3, data about experiments with different values of salinity are shown.

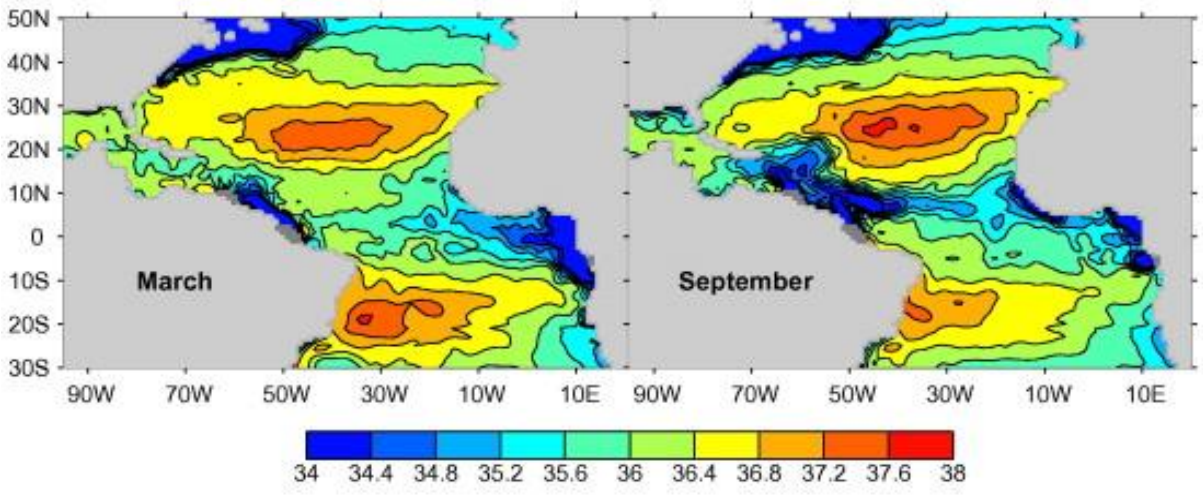

Figure 2.2. Salinity of the Atlantic Ocean in the upper part (3-15 m of depth), values are between 34 and 38‰. (Reverdin et al., 2007)

2.2. Slurry and powder

The $Ca(OH)_2$ can be added in two forms, namely a powder (as from the production) or a slurry; in both cases, the dissolution procedure started with the fine powder of $Ca(OH)_2$ which was weighed using an analytical balance, with a nominal precision of 0.0001 g. The powder was weighed on a watch glass or a Petri dish and directly poured in the solution, whereas the slurry was obtained by adding dropwise a small amount of seawater to the powder, using a glass rod for mixing (see fig 2.3 for the two forms of $Ca(OH)_2$).

After testing different slurries of high or low molarity, the concentration of 1.5 molarity (8.5 g of seawater every 1 g of $Ca(OH)_2$) was found to be a good compromise between low addition of water and sufficient fluidity of the slurry. To choose the molarity of the slurry, it should be considered that the release in the ocean will be probably performed piping the mixture through tubes.

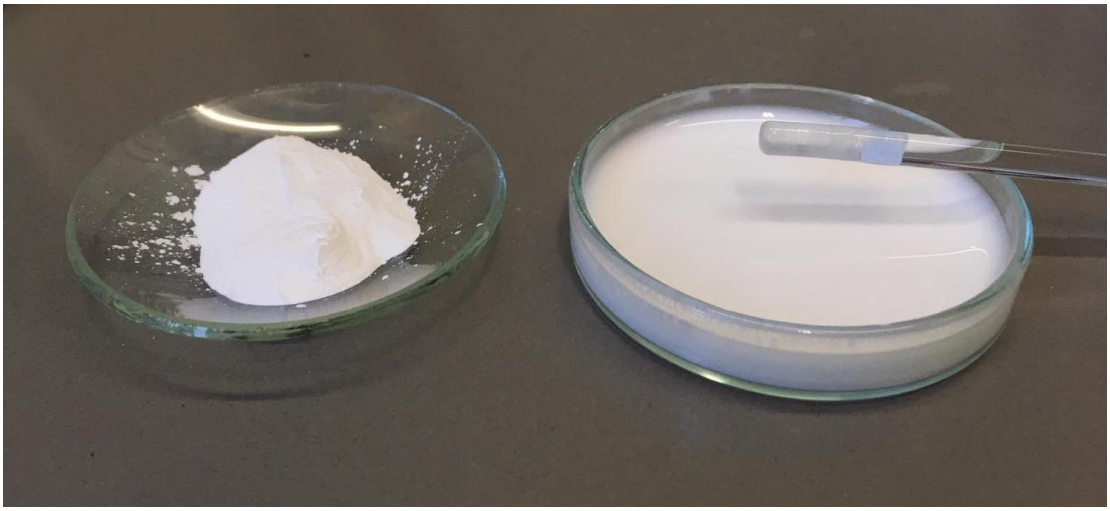

Figure 2.3. Comparison between 1 g of $Ca(OH)_2$ and 1 g of $Ca(OH)_2$ diluted in 1.5 M slurry

2.3. Temperature effect

Before spreading $Ca(OH)_2$, as powder or slurry, the water temperature was carefully controlled. From basic chemistry knowledge (Barron et al., 2005), it is known that the electrical conductivity is strictly correlated to temperature, as it emerged also from our experiments, fig. 2.4.

In a limited range of temperature, the relationship can be modelled linearly, with eq. 33 (25°C as reference).

$$C_{T_{25°}} = C_{T_{Solution}}[1 + \alpha(25 - T_{Solution})] \quad (33)$$

where:

$C_{T_{25°}}$ is the conductivity at reference temperature (25°C)

$C_{T_{Solution}}$ is the conductivity at temperature of measurement

α is the temperature coefficient of variation

$T_{Solution}$ is the temperature of the solution

α is specific for each solution: in case of fresh water is around 2%/°C, tab. 2.3 (Down et al., 2005), similar values are for basic solutions, while for acidic ones the coefficient is lower (Barron et al., 2005; Down et al., 2005).

Table 2.3. Temperature coefficient **α** for different types of solutions (Down et al., 2005).

Solution	**α temperature coefficient**
Acids	1.0-1.6%/°C
Basis	1.8-2.2%/°C
Salts	2.2-3.0%/°C
Fresh water	2.0%/°C

Two chemical mechanisms are responsible for the variation of conductivity. As the temperature rises, the mobility of the ions is increased, but also ion pairs, i.e. charged ions that aggregate in the solution and, as they are neutral, do not contribute to conduct electricity, are reduced.

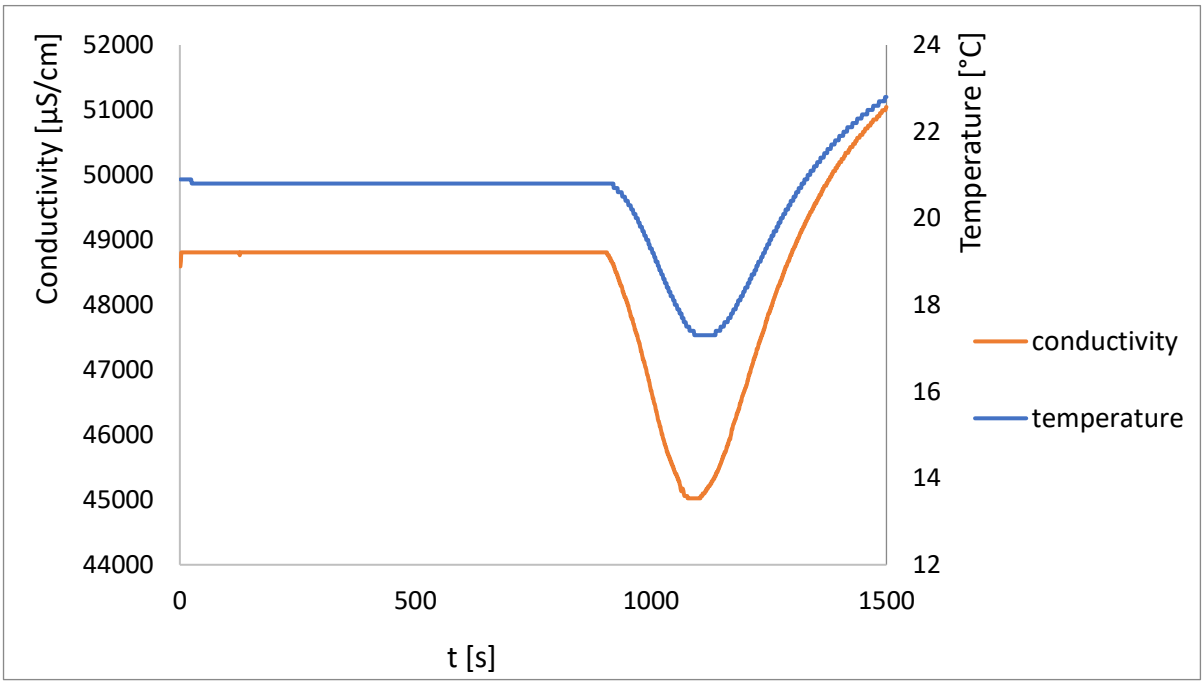

Figure 2.4. Plot of the conductivity (orange) and temperature (blue) of synthetic seawater under heating and cooling.

One may be tempted to think that it is possible to record experiments at whichever temperature and, afterwards, correct the conductivity with this calibration function. Although technically feasible, the resolution of the thermometer (both for the pH and conductivity sensor) is only 0.1 °C, leading to very poor results, fig. 2.5 blue trajectory.

The blue trajectory of fig. 2.5 shows two kinds of conductivity oscillations. The first one is directly linked to variations of temperature at time t (green trajectory, approximately at 700 and 1 900 seconds), the second one is due to the sensitivity of the instrument, which switches multiple times from a value to another when the output is close to a change. This last behaviour is clearly observable at second 1 000.

The first type of noise was canceled evaluating the average temperature that occurred during each experiment, and correcting then all the recorded values with that fixed difference from reference 25°C. In this manner, it was possible to cancel the dependance of read conductivities from sudden change of the temperature. The second type of noise, though, the “true” oscillating conductivity, remained. The result of this procedure is the red curve of fig. 2.5.

To evaluate an empirical coefficient of correction also at temperatures distant from 25 °C a measure of conductivity of seawater at 35‰ was performed over a gradient of temperature, fig. 2.6.

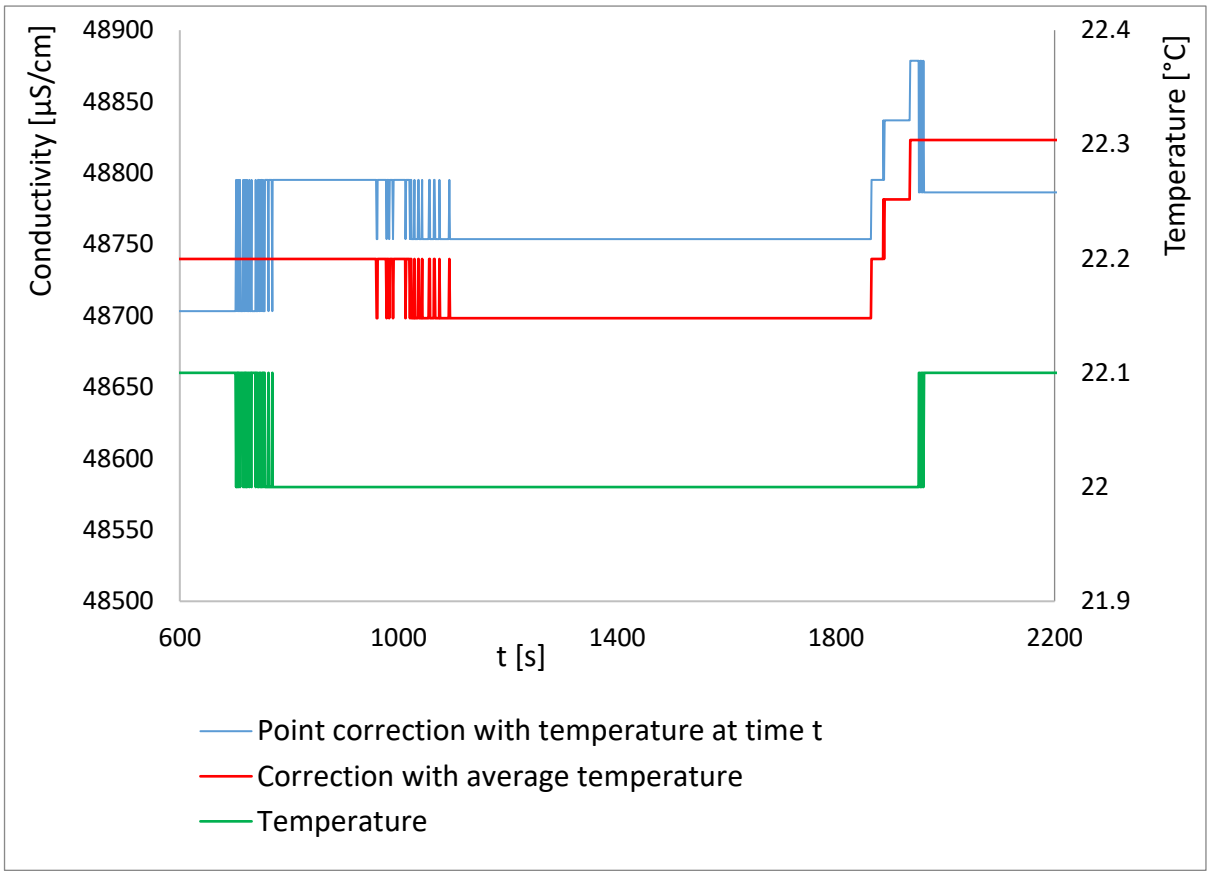

Figure 2.5. Measurement of conductivity with point correction with temperature at each instant (blue), conductivity corrected with average temperature during the test (red) and temperature (green). The scale for conductivities is on the left axis while for temperature is on the right.

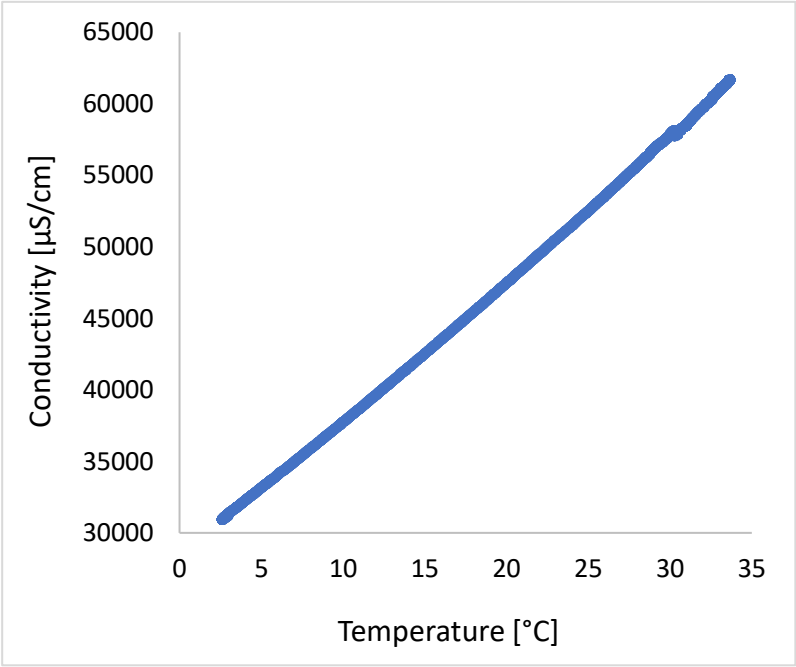

Figure 2.6. Conductivity measured as function of the temperature.

Starting from the value of conductivity registered at 25 °C, 52 504 μS/cm, it was possible to calculate the correction of conductivity on some selected temperatures. The results are shown in tab. 2.4.

Table 2.4. Registered conductivity, difference from registered conductivity at 25 °C and coefficient of correction for the temperatures at 5, 10, 20 and 30 °C.

Temperature [°C]	5	10	20	25	30
Conductivity [μS/cm]	33 158.0	37 743.2	47 483.9	52 504.2	57 825.4
Difference of conductivity from 25 °C [μS/cm]	19 346.2	14 761.0	5 020.3		-5 321.2
%/°C	0.0292	0.0261	0.0212		0.0184

These coefficients were used to correct the results in section 3.5.

The temperature of the solution also affects the measurement of the pH in a double manner, one concerns the internal procedure of value reading of the instrument, automatically corrected, the other is linked to the chemical composition of each solution. These aspects are explored in section 2.5.1, as the explanation of their relationship cannot be decoupled from the general description of the pH meter's functioning.

In our experiments each trial was recorded for at least 30 minutes to monitor the temperature of water before the pouring of calcium hydroxide. Afterwards, if the temperature was stable, the experiment was ready to begin. After the spreading of $Ca(OH)_2$, pH and conductivity were generally measured for half an hour, for an overall experimental measurement of one hour.

As practical experience suggests, it was very difficult to maintain the same temperature throughout an hour of test, thus, when looking at the final results and the recorded temperature evolution, we decided to save just those experiments with an inner variability of 0.1-0.2 °C in an hour.

2.4. Duration of the measurements

The duration of the experiment, referring just to pH and conductivity, was fixed at one hour: thirty minutes of to check the stabilization of parameters in seawater and thirty minutes of data collected after the dissolution of $Ca(OH)_2$ (cf chapter 2.3). This set up was chosen after many preliminary measurements lasting up to 72 hours.

In fact, after the release of $Ca(OH)_2$ in seawater it is evident that, except for the decrease of the pH due to the absorption of CO_2 (Han et al., 2011) and the subsequent formation of $CaCO_3$ (Van Eekeren et al., 1994), no other remarkable (or monitorable) event occurs. Because our goal is determining the kinetics of the dissolution process, a reasonable time-range to monitor the changes of physical properties is 30 minutes.

In fact, registering data for longer periods of time did not bring additional information, whereas, water evaporation became a non-negligible issue, as the conductivity tended to grow almost linearly in time, fig. 2.8-2.9.

A simple experiment was performed to estimate the magnitude of the evaporation: 1 liter of seawater was left, under magnetic agitation, recording temperature and conductivity for almost 63 hours. No external control of temperature was applied except for the room conditioning which was left at the same level all the time. In fig 2.7. are shown the values recorded during the experiment. Evaporation can clearly be seen after 150.000 seconds: as water evaporates, the concentration of diluted salts raises and the conductivity reflects this phenomenon.

To estimate the amount of conductivity gained during time two approaches were taken: the first consisted in evaluating the conductivity, by means of single points, when the temperature was at 25°C fig. 2.8. The second one considered all the values between 160 000 and 210 000 seconds, fig. 2.9, where the temperature moved just by 0.1 °C.

Fig. 2.8 shows three values of the conductivity at 25°C, respectively at 6 480, 68 400 and 90 480 seconds: points are aligned on a straight line, and the linear fitting returns an R^2 of 0.99.

Fig. 2.9, instead, reports the trajectory of temperature and conductivity in the interval 160 000 - 210 000 seconds: the estimation of a linear regression returns an R^2 of 0.98.

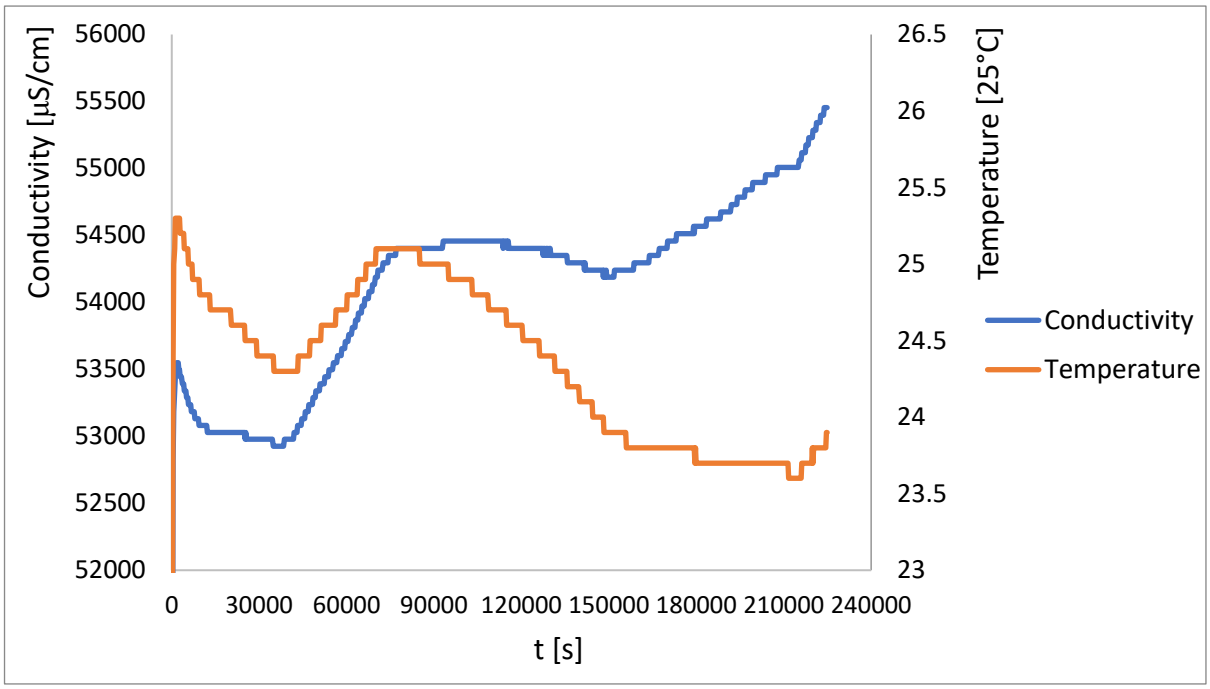

Figure 2.7. Measurement of the conductivity (blue) and the temperature (orange).

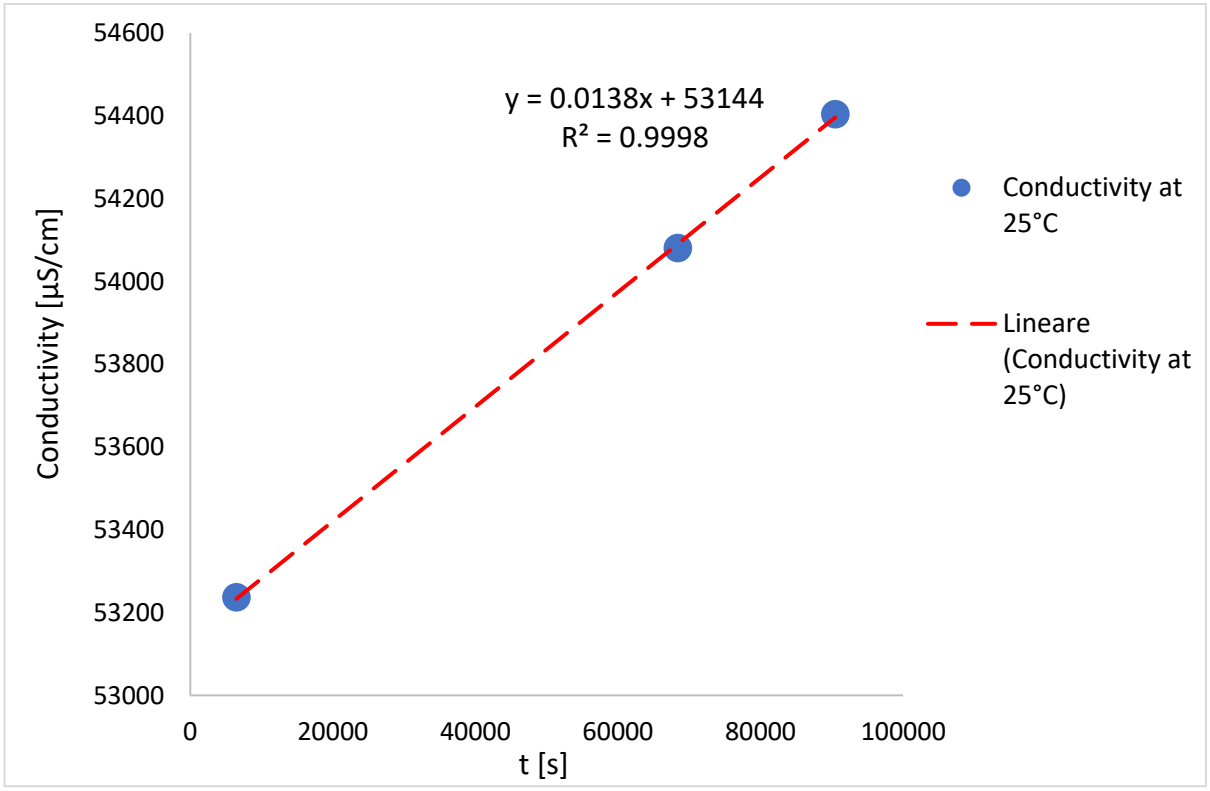

Figure 2.8. Conductivity (blue dots) at 25°C at different time steps. The red dashed line represents the linear regression of the points. The equation of the line and the R^2 correlation coefficient are reported too.

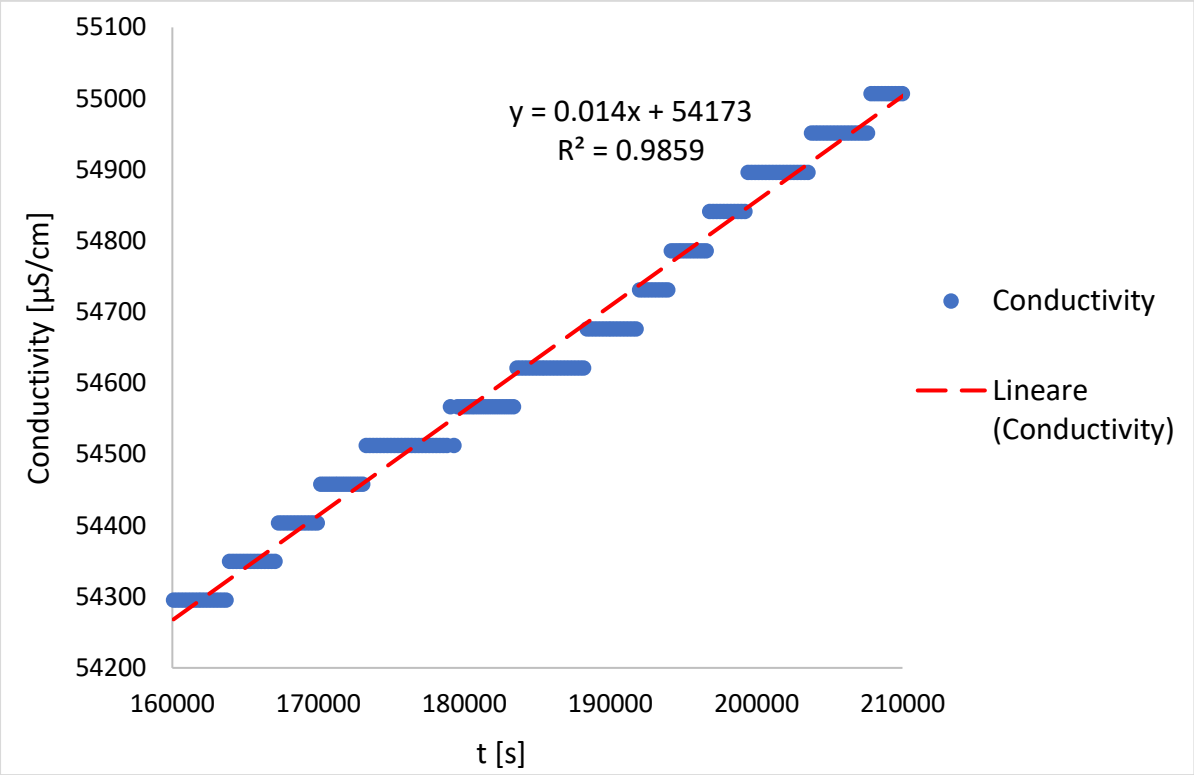

Figure 2.9. Plot of the conductivity (blue dots) in the time window of 160 000 and 210 000 seconds. The red dashed line represents the linear regression of the points. The equation of the line and the R^2 correlation coefficient are reported too.

From an average conductivity of seawater of 53 000 µS/cm it was possible to estimate, using the angular coefficient of the linear regression of both red trajectories of fig. 2.8 and 2.9, the amount of conductivity increase in one hour, the length of the most common experiment. The coefficient in fig. 2.8 leaded to the result of 49.68 µS/cm, while, using the second, resulted in 50.4 µS/cm.

This amount was close to the sensitivity of the conductometer when soaked into seawater (about 50 µS/cm). This issue became particularly relevant when performing experiments at very low concentrations of calcium hydroxide (0.05-0.2 g/L) because the gap of conductivity from the original value of seawater and the final one after dissolution was very limited. However, the series were not corrected, as the final result, assuming a linear function accounting for evaporation, would have returned unpractical results. The reason of this choice is that the estimation of the evaporation (which depends on not controllable variables: temperature, humidity of the air, presence of flowing air…) was extremely local and not reproducible and because the conductometer had an inner resolution of temperature of 0.1°C which caused problems in the estimation of the real value of conductivity (section 2.3).

In the end, measurements of conductivity for concentrations of 0.05-0.1 g/L, which produce limited conductivity variations, must be considered with this element in addition and further future investigation is needed.

2.5. Technical equipment

The standard tools involve a beaker of 2 or 5 liters of capacity that is filled with the solution and kept under agitation with a stirring equipment. The stirring machines used in these experiments were of two types: a conventional magnetic stirrer and a specific mechanical stirrer in order to simulate a non-perfect and homogeneous agitation as in a ship's wake.

Magnetic stirring works through an external rotating magnet: a magnetic bar at the bottom of the beaker fig. 2.11, follows the rotation of the magnet (fig. 2.10). This technique ensures a very good level of mixing as almost the whole volume is involved.

Figure 2.10. Magnetic bar placed at the bottom of the beaker (Bola.de).

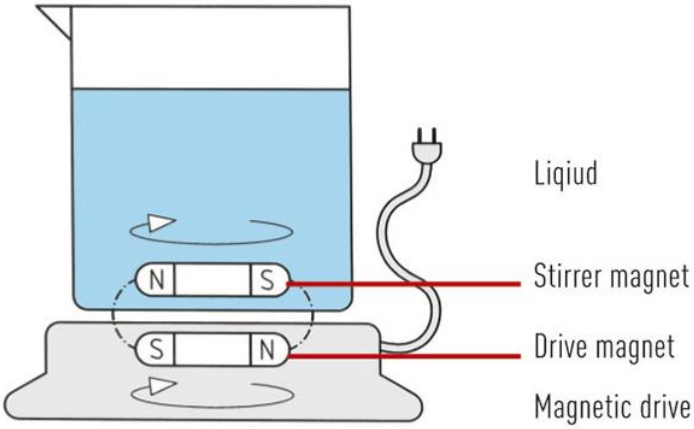

Figure 2.11. Simplified scheme of works of magnetic stirring agitation (Bola.de).

On the other hand, a mechanical stirrer consists of a rotating rod (moved by an engine at the top) with an impeller at its bottom, fig 2.12-2.13. Both items can be regulated at a specific rotating speed but the latter has the advantage that rotation can be triggered at the different height levels in the beaker. Mechanical stirring, at low velocities, however, ensures mixing just in the area nearby the impeller. Applying the stirring close to the surface of the solution, is the best way to simulate conditions of the turbulence left by a ship's propeller, as the volume closer to the bottom of the beaker experiences only a reduced agitation.

In tab. 2.5 the technical aspects of the mechanical stirrer are reported.

Table 2.5. Technical specifications of the mechanical stirrer.

Technical specification	**Measure**	**Unit of measure**
Stirrer diameter	50	mm
Shaft diameter	8	mm
Shaft length	400	mm
Max speed	2 200	rpm
Weight	0.165	kg

Figure 2.12. Detail of the mechanical stirrer's impeller. (www.ika.com)

Figure 2.13. Mechanical stirrer. (aliexpress.com)

2.5.1 pH-Meter

The pH-meter (Mettler-Toledo InLab Routine Pro-ISM, technical sheet in fig. 2.14) was a fundamental instrument for this research, it is composed by two electrodes, combined in a unique sensor. The first electrode is made by a glass membrane (permeable only to the hydrogen ions) and measures the electro-chemical potential of hydrogen ions between the solution and the filling solution of the electrode, with a fixed concentration of KCl; the second, called reference electrode, completes the electrical circuit. The value read by the instrument is in unit of mV and, after a conversion, a value in the classical pH scale 0-14, with 7 as neutral's value, is returned. The relationship linking mV and pH is defined by the Nernst equation, eq. 34:

$$E = E_0 + 2.3\frac{RT}{nF} log\ a_{H^+} \qquad (34)$$

Where:

E is the potential measured [mV]

E₀ is a constant [mV]

R is the universal gas constant

T is the temperature in Kelvin

n is the ionic charge

F is the Faraday constant

a_{H^+} is the activity of the hydrogen ions.

The part $2.3\frac{RT}{nF}$ is also called slope, E_n. A pH-Meter must integrate a measurement of temperature, that influences the pH measured and its value. Higher temperature causes a rise of the ions mobility in the solution, this effect is due to the chemistry of the solution and peculiar for each solution: this influence cannot be compensated by the instrument, that measures and returns the pH-value at the actual temperature. What is possible to compensate, through the measurement of the temperature, is the slope (E_n). At 298 K (25°C), E_n is -59.16 mV/pH, this is the slope known from the calibration of the electrode. Changing temperature of the solution brings a change in the coefficient (Meier and Lohrum, 1989; Mettler-Toledo, 2016).

The compensation can be done in two ways, manually or automatic, the pH-meter InLab Routine Pro-ISM uses an Automatic Temperature Compensation (ATC).

For a good accuracy, it is necessary to calibrate the instrument periodically using standard solutions of known pH. Different types of calibration can be done, with different accuracy levels but it is recommended to use a standard in the range of interest.

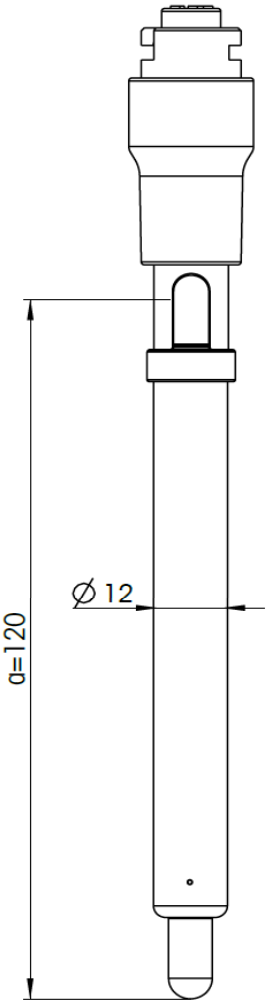

Sensor type	combined pH electrode
Order number	51344055
Specifications	
pH range	0...14
zero point (pH)	7.00 ± 0.25
temperature range	0...100 °C
temperature probe	NTC 30 kΩ
shaft material	glass
membrane glass	HA
membrane resistance	< 600 MΩ
reference system	ARGENTHAL™
reference diaphragm	ceramic
reference electrolyte	3 mol/L KCl
bridge electrolyte	-
electrode head	MultiPin™
cable length	-
connector	-
cell constant (cm^{-1})	-
cell type	-
indicating metal	-
Storage	
InLab storage solution (30111142) or 3 mol/L KCl (51350072)	

Figure 2.14. Representation of the pH-meter's sensor with its specification (Mettler-Toledo).

2.5.2 Conductivity-meter

The Conductivity-meter (Mettler-Toledo InLab 731-ISM, technical sheet in fig. 2.15) was one of the sensors soaked in the seawater during experiments, its role was to measure the conductivity of the sample solution. The conductivity is the inverse of the resistivity, the length specific current carrying ability, and it is measured in S/m or μS/cm.

The working principle of a 2-electrodes conductivity-meter is based on two electrodes close to each other at the tip of the sensor, with a specific cell constant. An AC tension is generated and a current flow between the two electrodes is established, creating a circuit. However, only charged particles present in solution can transport electricity. A known quantity of electricity passes from the first electrode to the other. The amount of electricity measured, is function of the conductivity of the solution.

For better measurement accuracy, a four electrode conductivity-meter should be used. The current, flowing in the solution, can cause a polarization of the electrons; to compensate that phenomenon, two electrodes are used like passive observers, these two added electrodes measure the difference of potential. From that measurement and the current recorded the instrument is able to calculate the conductivity (Ramos et al., 2008).

The conductivity-meter has an integrated thermometer on the sensor, to measure the temperature of the solution. This information is important because the conductivity is highly dependent from the temperature and must be compensated to a reference temperature, generally 25 °C, in this manner is possible to compare experiments performed over different range of temperatures (explained in section 2.3).

From practical experience it was noted that the sensitivity of the instrument downgraded as the amount of salts, and relative total conductivity, increased. At very low concentrations of salts (e.g. calcium hydroxide diluted in distilled water) the sensitivity was in the order of some units of μS/cm. At low salinities (e.g. 10‰) the gap was about 10 μS/cm, while for average seawater (35‰) the minimum detectable difference was 50 for μS/cm.

To use properly the instrument a periodic calibration is required. From the instruction manual provided by the manufacturer, a solution of known conductivity, called standard solution, is used to reset the instrument (including temperature correction). For better accuracy, it is recommended to use a standard in the range of measurements to be performed.

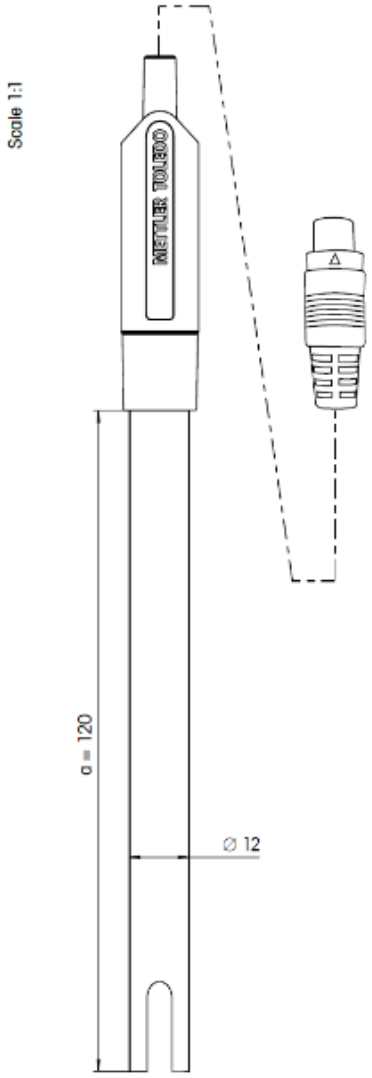

Sensor type	conductivity cell
Order number	30014092
Specifications	
measuring range	0.01…1000 mS/cm
zero point (pH)	-
temperature range	0…100 °C
temperature probe	NTC 30 kΩ
shaft material	epoxy
membrane glass	-
membrane resistance	-
reference system	-
reference diaphragm	-
reference electrolyte	-
bridge electrolyte	-
electrode head	-
cable length	1.2 m
connector	Mini-DIN
cell constant (cm^{-1})	0.67
cell type	4 graphite poles
indicating metal	-
Storage	
dry	

Figure 2.15. Representation of the conductivity's sensor with its specification (Mettler-Toledo).

2.5.3 Heating and cooling thermostat

To control the temperature during the trial and perform experiments over different range of temperatures, a heating and cooling thermostat was used. The thermostat, *Lauda Eco Silver*, allows to set the temperature with a discretization of 0.1°C, from -50 up to 200 °C. The instrument is filled with its specific oil, *Lauda Kryo 20*, that, heated or cooled, performs heat exchange. The oil exchanges heat through a steel coil, connected by tubes to the main body of the thermostat. The coil was not placed inside in the beaker, avoiding interference with the stirring of the solution. A tray filled with water was in touch with the coil and the beaker containing the seawater, where the monitored reaction takes place. The water in the tray was stirred by the mechanical agitator, to ease the heat transfer. The setting of the various described components is shown in fig. 2.16.

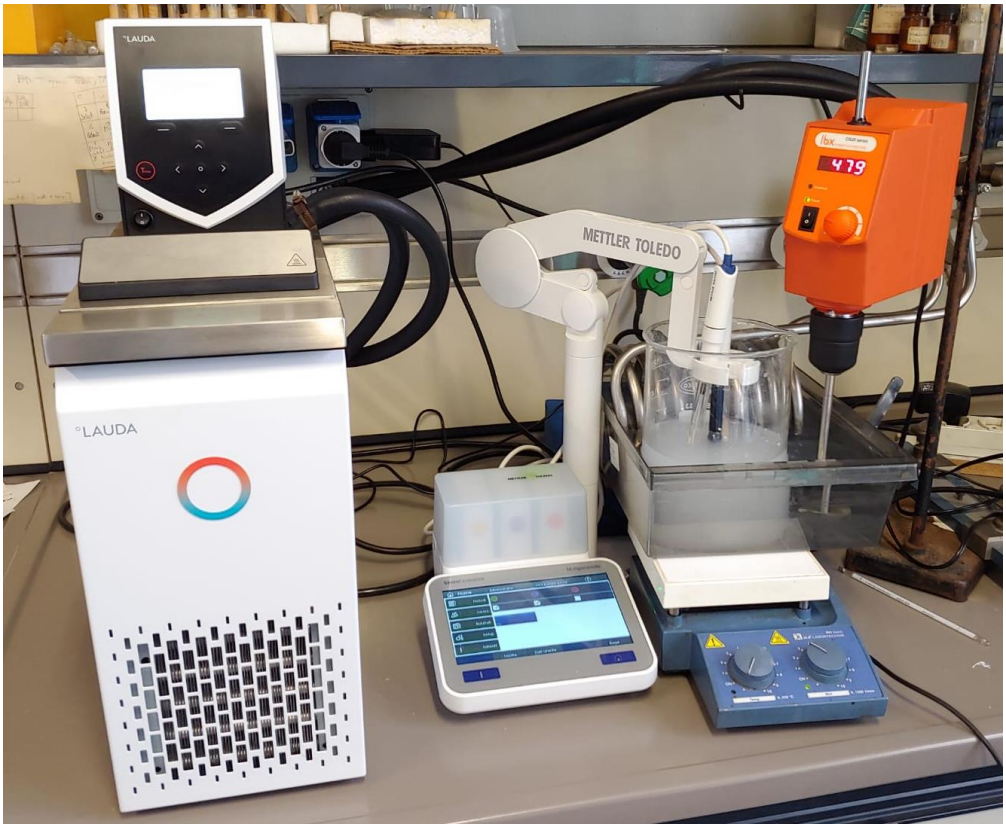

Figure 2.16. Picture of the technical equipment employed during the experiment with temperature control.

The majority of the experiments was done without the thermostat, it was necessary just for the set of measurements at 5 and 10°C. The other trials were controlled by setting and maintaining the air temperature of the laboratory constant.

2.5.4 Alkalinity automatic titrator

Other measurements of the work concerned the estimation of the total alkalinity, performed through an automatic titrator.

The alkalinity concept was a key aspect in our research: by means of its estimation, it is possible to determine, as first approximation, the exchange of CO_2 evaluating the Dissolved Inorganic Carbon (DIC) over time.

Alkalinity is defined as "*the number of moles of hydrogen ion equivalent to the excess of proton acceptors over proton donors in one kilogram of sample*" (Dickson and Goyet, 1994).

In a short expression alkalinity is the result of carbonates [CO_3^{--}], bicarbonates [HCO_3^-] and hydroxide [OH^-], ions in the solution minus the concentrations of hydrogen [H^+] ions. However, alkalinity includes also all contributions from borate, phosphates, silicates, and other base species present, eq. 35. Of these contributions, just S-containing ions played a role in our solution, as neither the salts or $Ca(OH)_2$ were containing minerals with B, P and Si.

$$TA = [HCO_3^-] + 2[CO_3^-] + [B(OH)_4^-] + [OH^-] + [HPO_2^{2-}] + 2[PO_4^{3-}] + [H_3SiO_4^-] + [NH_3] + [HS^-] + [H^+]_F - [HSO_4^-] - [HF] - [H_3PO_4] \quad (35)$$

The same definition can be obtained considering another term of the equation, the one regarding conservative ions: these ions are thus defined because their concentrations remain stable despite changes in pH, pressure or temperature. Generally conservative ions are: Na^+, K^+, Ca^{2+} , Mg^{2+} , Cl^-, SO^{2-} and NO^{3-} (Zeebe, 2002).

In order to perform a rapid and good-quality estimation of the alkalinity, an automatic titrator was used (Hanna Instruments HI-84531). An automatic titration, in facts, ensures an accuracy but most importantly a repeateability in the operation that is hardly reached when performed manually.

Titration is an estabilished tecnique that aims to determine an unknown concentration of a known substance in a sample; referring to alkalinity, this is obtained by adding a strong acid (or base) to the solution till reaching a fixed point of a certain variable (ex. pH) or an appropriate potentiometric value.

The instrument can provide two different types of alkalinities that are related to a fixed value of pH, commoly called endpoints. The first point is called Strong Alkalinity or Phenolphthalein Alkalinity, tipically at pH 8.3, the second one, which was employed, is the Total Alkalinity or Bromcresol Alkalinity, at pH 4.5 (Miner, 2006).

The addition of the titrant is slow in order to determine accurately the endpoint, however, in order to save time and avoid unwanted secondary reactions, the instrument finds automatically a compromise dispensing larger amounts of titrant when the curve of pH is flat (the buffer effect is still in charge) and reducing the rate when the buffer effect is broken and the selected endpoint is approaching.

The equipment used in the work, fig. 2.17, restitutes the result into mg/L of equivalent $CaCO_3$ dissolved. The instrument can use two types of acids, depending on the expected value of alkalinity. A Low Range acid (LR) is employed when the alkalinity is in the range of 30 – 400 mg/L of $CaCO_3$, while a High Range (HR) works between 300 and 4 000 mg/L.

For both possibilities it is requested to process strictly 50 mL of sample. However, it was verified that it was possible to titrate also lower amounts of sample, e.g. 25 mL, and then double the returned alkalinity. This procedure worked with good precision and enabled, using less than 50 mL, to extend the upper limit of detectable alkalinity by rescaling, at the end, of the process, the result.

Figure 2.17. Automatic titrator used for determination of alkalinity (Hanna Instruments).

2.5.5 X-Ray Diffraction

X-Ray Diffraction, (XRD), is a methodology used to analyse the structure of solid crystalline materials. Through this test it is possible to identify the crystalline phases of a material and obtain chemical information about the sample.

The X-rays beam are generated by a cathode ray tube and then directed toward the sample. The interaction of the sample with the incident wave produces a diffracted ray and a constructive interference, following Bragg's law, eq. 36.

$$n\lambda = 2d\ sin\ \theta \qquad (36)$$

Where:

n is an integer that expresses the diffraction order

λ is the wavelength of the ray

d is the interplanar spacing

θ is the angle between the wave vector and the incident plane wave.

Figure 2.18 represents a scheme of eq. 36.

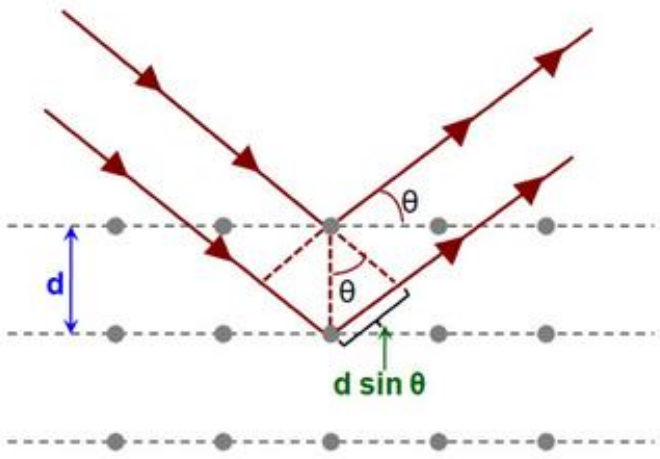

Figure 2.18. The Bragg's law representation, the grey dots represent the sample, beat by the x ray, in red. (Baskaran, 2010, fig.12).

The law links the diffraction angle to the wavelength of electromagnetic radiation and the lattice spacing in the sample. The diffracted rays are then detected and measured.

X-ray diffraction is often used to determine the structures of unknown materials, but it is also adopted to identify known phases in samples and quantify their amounts in mixtures.

Identification of crystals and phases is obtained by the comparison of data obtained during the test with reference values available on scientific literature, e.g. the results is the figure 2.19, that show the XRD spectra of $Ca(OH)_2$.

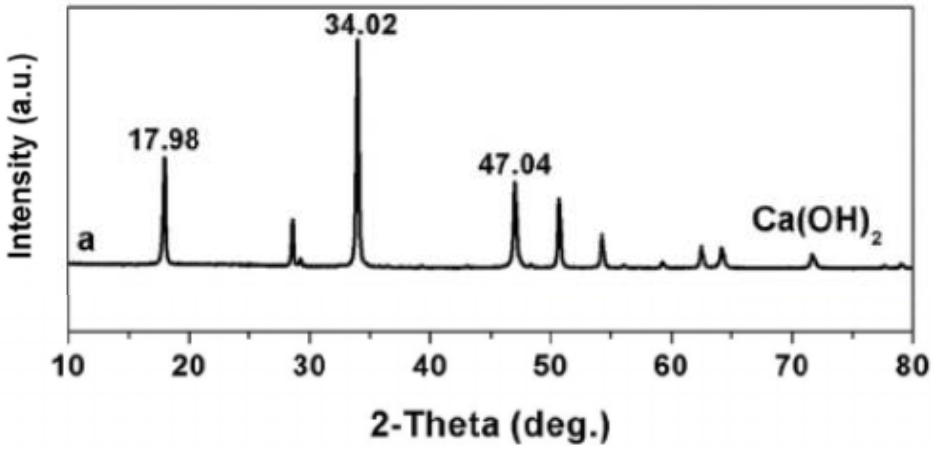

Figure 2.19. The XRD spectra of $Ca(OH)_2$ (Liang at el., 2018, fig. 4).

In this research it was used a Cu radiation diffractometer, set to 2 theta, in a range of 10-70°. The analyzed samples are obtained from the dried residues on the filter after the Buchner filtration process.

2.6. Basics of statistics

In this section it is reported a brief summary of the statistical tools and methods used to perform an analysis reported in section 3.8.

2.6.1 Linear regression

In statistics, linear regression refers to an approach of modelling the relationship between a variable Y and one or more dependents variables, $X_1, X_2, \dots, X_n$. The model is estimated from the data using linear functions linking the X_n variables to the Y.

If the objective of the model is prediction, linear regression can be used to fit a predictive model of an observed dataset, using the explanatory variables $X_1, X_2, \dots, X_n$. Once the model is set, it can predict or calculate the Y for new values of $X_1, X_2, \dots, X_n$.

Linear regression analysis can be applied both to quantify the strength of the relationship between Y and $X_1, X_2, \dots, X_n$, and assess which of the X_i may be unrelated to Y, as well as to identify which subsets of the $X_1, X_2, \dots, X_n$. contain redundant information about Y.

The relationship, of the variables Y and $X_1, X_2, \dots, X_n$, is expressed by the eq. 37, considering the error, in the form:

$$Y = f(X_1, X_2, \dots, X_n, \varepsilon) \qquad (37)$$

The linear model is based on a structure such as eq. 38:

$$Y = a_1 X_1 + \cdots + a_n X_n + b + \varepsilon \qquad (38)$$

Where:

a_i is the coefficient for each X

b is the intercept

ε the error of the model.

This relationship is called multiple linear regression and the parameters are estimated from the data, often using the Least Squares method (LS).

The main assumptions on the data, in a linear regression model where coefficients are evaluated by LS method, are the following:

1. The predicted variable, Y, should be measured on a continuous scale.

2. The predictor variables can be either continuous or categorical.
3. Observations must be independent (i.e., independence of residuals $Cov(\varepsilon_i, \varepsilon_j) = 0$).
4. Linearity: each predictor has a linear relationship with the outcome variable.
5. Normality: the residuals of the model are approximately normally distributed in the population.
6. Homoscedasticity: the residuals are distributed as a normal with average 0 and constant variance $Var(\varepsilon) = \sigma_2$
7. Non multicollinearity: two or more independent variables must not be highly correlated with each other.
8. There should not be significant outliers, high leverage points or highly influential points.

2.6.2 Pearson correlation index

The Pearson correlation index (also called linear correlation coefficient) between two statistical variables is an index expressing the linearity relationship between them.
Given two statistical variables the Pearson correlation index is defined as in eq. 39:

$$\rho(X,Y) = \frac{Cov(X,Y)}{\sigma_X \sigma_Y} \qquad (39)$$

Where:
$Cov(X,Y)$ is the covariance of X, Y
σ_X and σ_Y are the standard deviations of X and Y.

It can take a value between 1 and -1, where 1 corresponds to perfect positive linear correlation, 0 corresponds to nonlinear correlation and -1 corresponds to perfect negative linear correlation.

2.6.3 Forward method

The forward method is a procedure that can be used in the linear regression models. Its main feature, as suggested by the name, is to add, step by step, new predictors, starting from the intercept alone. Each predictor, $X_1, X_2, \dots, X_n$, is tested to verify whether it adds (and how much) information to the predictive model.
To procedure is iterative, the first variable to insert is the one with the highest direct correlation.

At that point a test is performed to evaluate the added variable is significative or not, generally it is performed through an F test ratio: if the value is higher than a selected value F_α where α is the significance, the variable is accepted otherwise is refused.
A typology of the first F test is reported in eq. 40:

$$F_{ratio} = \frac{MSR\ (X_1)}{MSE\ (X_1)} \tag{40}$$

Where:
MSR is the mean square root
MSE is the mean square error of the model with the selected variable X_1.
The value of significance employed, α can be found on specific tables.
After this the method proceeds adding another variable, X_2, and testing it through another F test. This time the partial F test calculates the contribute given by the new variable to the sum of squared residuals with respect to the already included variables, eq. 41.

$$F_{x_2} = \frac{SSR\ (X_2 \mid X_1\ )}{MSE\ (X_2, X_1)} \tag{41}$$

The variable with the highest F test is tested in order to refuse/accept it with the same rules as before. It is possible also use a *p-value* calculated specifically for the F test.

2.6.4 Variance Inflation Factor (VIF)

Variance inflation factor (VIF) is an index able to highlight the multicollinearity conditions in a linear regression analysis. Multicollinearity is a condition of correlation between predictors, these last should be by definition independent. The VIF calculates how much the variance of a regression model is ascribable to the multicollinearity present in the model.
VIF is calculated for each predictor, $X_1, X_2, \dots, X_n$, through a simple procedure: each time is taken a predictor, X_i, and regressed against all other predictors in the model. The calculated R_i^2 is inserted into eq. 42. Generally strong multicollinearity is detected when VIF is higher than 10, between 5 and 10 the result is acceptable and below the multicollinearity is almost negligible.

$$VIF = \frac{1}{1 - R_i^2} \tag{42}$$

2.6.5 Principal component analysis (PCA)

Principal component analysis (PCA) is a technique for reducing the size of data used when a large number of characteristics $X_1, X_2, \dots, X_n$ are involved in the probabilistic and statistical analysis.

The reduction is achieved by substituting $X_1, X_2, \dots, X_n$. by one or two (generally no more than 3) principal components $Y_1, Y_2, \dots, Y_n$ that are correlated with each other. These components must not lose relevant information on the total variability, trying to explain it as much as possible.

A geometrical representation of PCA can be done performing a transformation in a new coordinate system, obtained by rotating the original one, that has $X_1, X_2, \dots, X_n$ as the coordinates axes. The new coordinate system represents the directions in the p-dimensional space, trying to give a description of the covariance structure with less variable, losing the less possible information (Johnson & Wichern, 2014).

To compute the principal component analysis several steps are required:

- Standardization of the range of continuous initial variables, in this way each one of them weights equally to the analysis
- Covariance matrix calculation of the whole dataset to identify correlations
- Eigenvectors computation and the corresponding eigenvalues, to identify the principal components.
- Sorting the eigenvectors by decreasing eigenvalues and choose m eigenvectors with the highest eigenvalues (generally not more than 3), to form a $n \times m$ dimensional matrix W.
- Transforming the samples onto the new subspace applicating the matrix W ($n \times m$ eigenvector matrix)

2.6.6 Variance in PCA

The variance is commonly intended as a unique concept, however, it can be explained and subdivided into two main groups: common and unique. The information of the following paragraph is provided by a free web-document provided by UCLA Institute.

Suppose a dataset of observation $y_1, \dots y_p$ and a number of variables (descriptors) $X_1 \dots, X_n$.

The common variance is the amount of variance that is shared across the data sample. The communality is a definition of common variance that ranges between 0 and 1. Value close to 1 indicate that the variables/descriptors selected are able to explain well the variance of the data.

The unique variance can be subdivided instead into: specific variance, a kind of variance that is specific for that experiment/survey and error variance, ascribable to general errors of measurement.

The PCA has, as assumption, that all the expressed variance is explained by the communality, no unique variance is present. This preliminary test has to be performed before the beginning of the PCA analysis.

3. Results and discussion

In this chapter we report results of the most relevant experiments.

The observables that we measure are: a) pH and conductivity, monitored continuously with a time step of 1 second, evaluating the response time of the samples when a perturbation is applied (release of calcium hydroxide); b) alkalinity, by means of an automatic titrator; c) particulate of filtered solutions, using a XRD technique. The last two are measured just on some selected trials, and they cannot be performed in real time. The alkalinity needs, for the entire procedure, around 20 minutes, while the XRD is performed, generally, after the filtered matter has dried.

The variables that we test are either physical or methodological. Among the former it is possible to include: a) salinity, b) temperature; while, for the second, c) different concentrations of calcium hydroxide, d) two possible forms: powder or slurry; in addition to these e) agitation, employing a more conventional magnetic stirrer or a mechanical by means of a rotating impeller.

3.1 Concentration of $Ca(OH)_2$ in solution

The evolution of parameters is studied as function of concentration expressed in grams of $Ca(OH)_2$ in 1 liter of solution.

The concentrations taken into consideration for the experiments start from low concentration, 0.05 g/L, up to 8 g/L. These limit reflects the minimum detectable change readable by the instrument and, on the other side, a value well beyond the saturation in distilled water, 1.57 g/L (Johannsen and Rademacher, 1999). Between the upper and lower limits are tested the concentrations at 0.1, 0.2, 0.4, 0.6, 0.8, 1, 2, 3, 4, and 5 g/L.

pH and the conductivity grow as the concentration rises. For the pH, figures 3.1 and 3.2 show different tests, listed according to the increasing concentration. In fig. 3.1, the baseline of the seawater shows low variability in the range of pH between 6.5 and 6.9. This can be explained by the fact that a pH close to 7 is very sensitive to even small random changes, like temperature, concentration of salts or possible residues of contaminating substances on the glassware.

The curves observed in figure 3.1, show a rapid increase, due to the release of the calcium hydroxide after 1 800 second, followed by a decrease of the pH values. Only the experiment with the highest concentration, 8 g/L, does not show any decrease of the pH (after 1 800 seconds), fig. 3.2.

Data in the following section refer to tests performed with magnetic stirring and calcium hydroxide in form of slurry at the temperature of 25 °C.

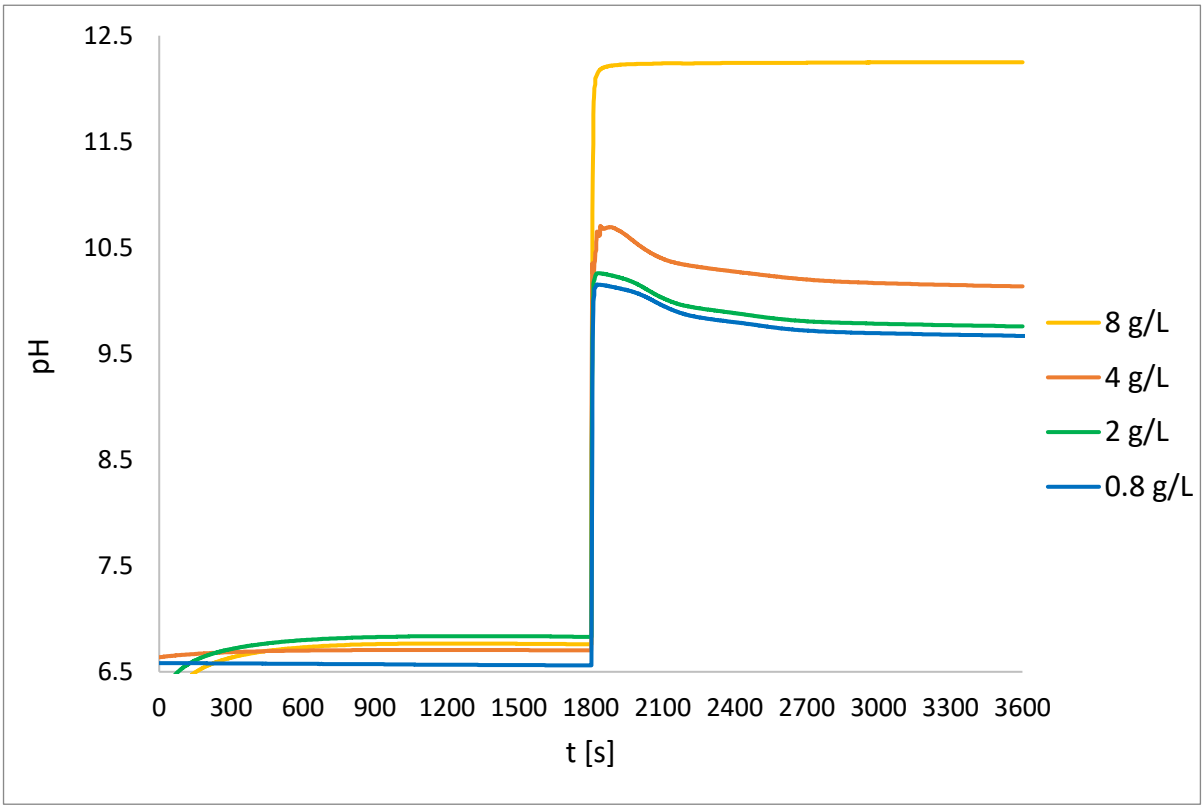

Figure 3.1. pH for different concentrations of calcium hydroxide. $Ca(OH)_2$ was released at t= 1 800 s.

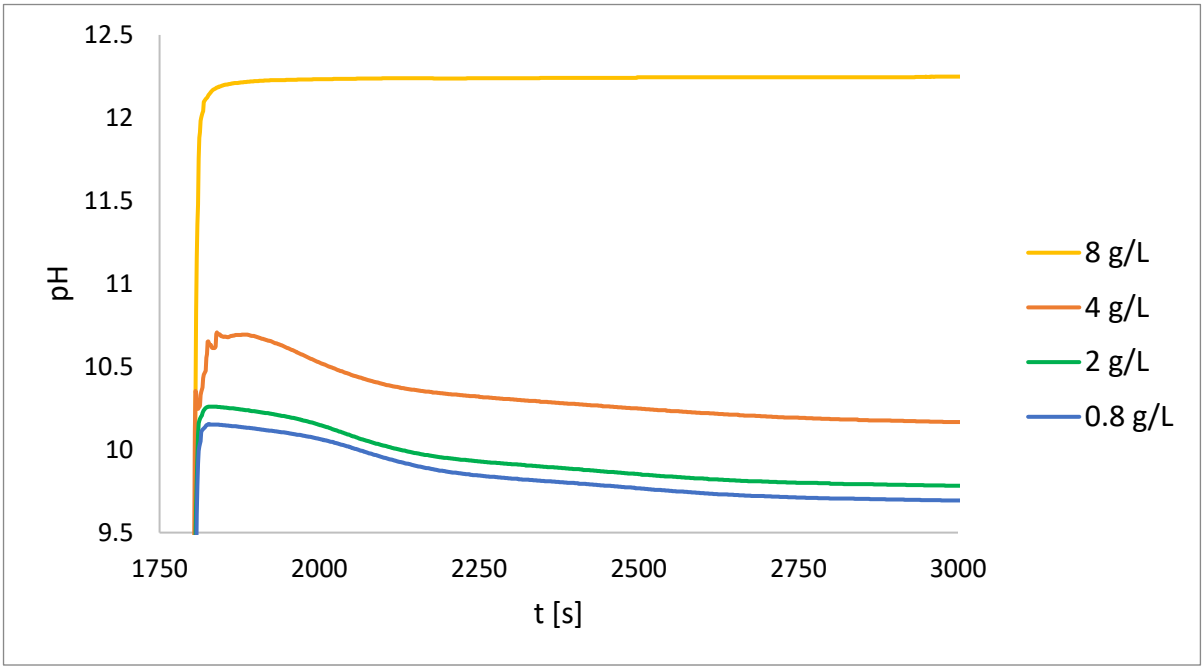

Figure 3.2. A magnification of figure 3.1 in the t range 1 750 -3 000 s and pH range 9.5-12.5.

Fig. 3.3 shows the evolution in time of the value of pH and molar concentration of hydronium ions [H^+] with respect to the concentration of $Ca(OH)_2$ in seawater. Blue dots represent the ratio between the pH measured at t= 3 600 s and the highest pH registered, the scale is on the left axis of fig. 3.3. Orange triangles, instead, convey a similar information in terms of the ratio between hydronium ions scale (shown on the right axis). pH decreases in time until the concentration of 4 g/L, whereas, above, it changes behaviour. After 30 minutes from the release, the decrease is hardly visible seen at 5 g/L and does not appear at 8 g/L.

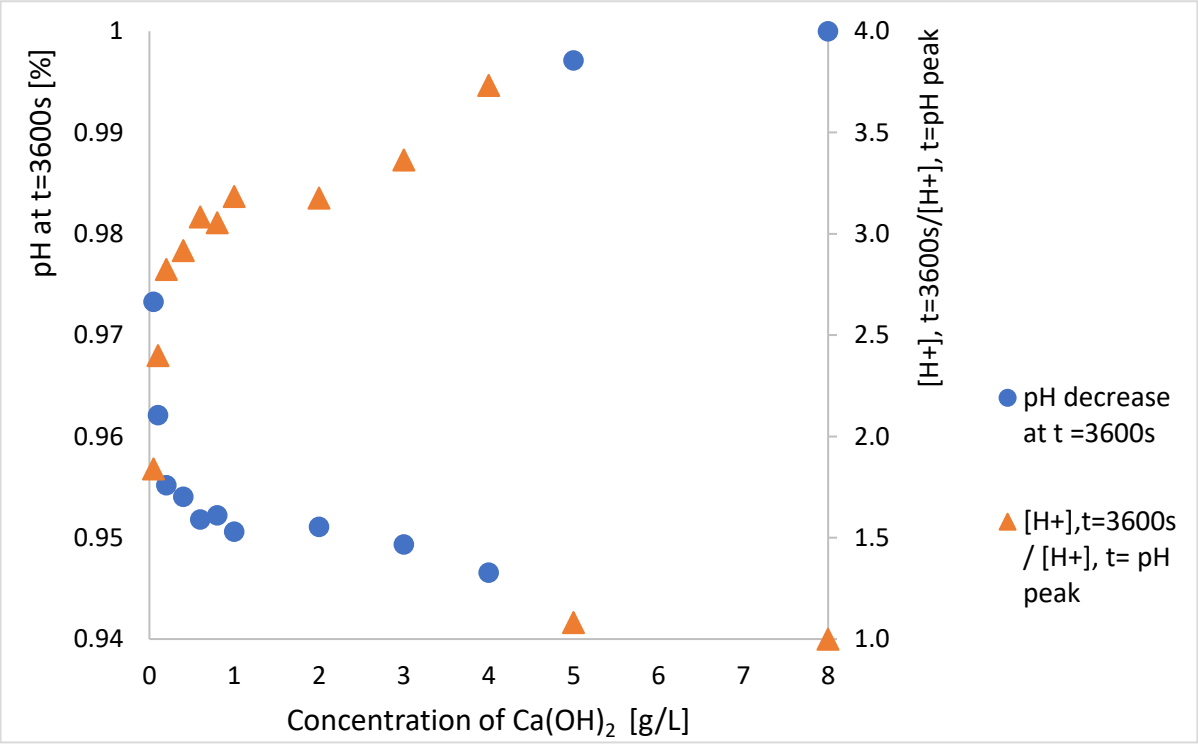

Figure 3.3. Percentage of pH decrease, blue dots, after 30 minutes from the release. Orange triangles indicate, instead, the ratio between H^+ ions registered at second 3 600 and at maximum pH registered. $Ca(OH)_2$ was released at t= 1 800 s

Another info on data about pH is the time employed to reach the peak, fig. 3.4. The peak is reached within a minute since the delivery, with a couple exceptions, especially for the concentration of 8 g/L. Other outliers are for 5 g/L (135 seconds) and 0.05 g/L (242 seconds). The latter may be the result of local effects and non-homogeneous mixing.

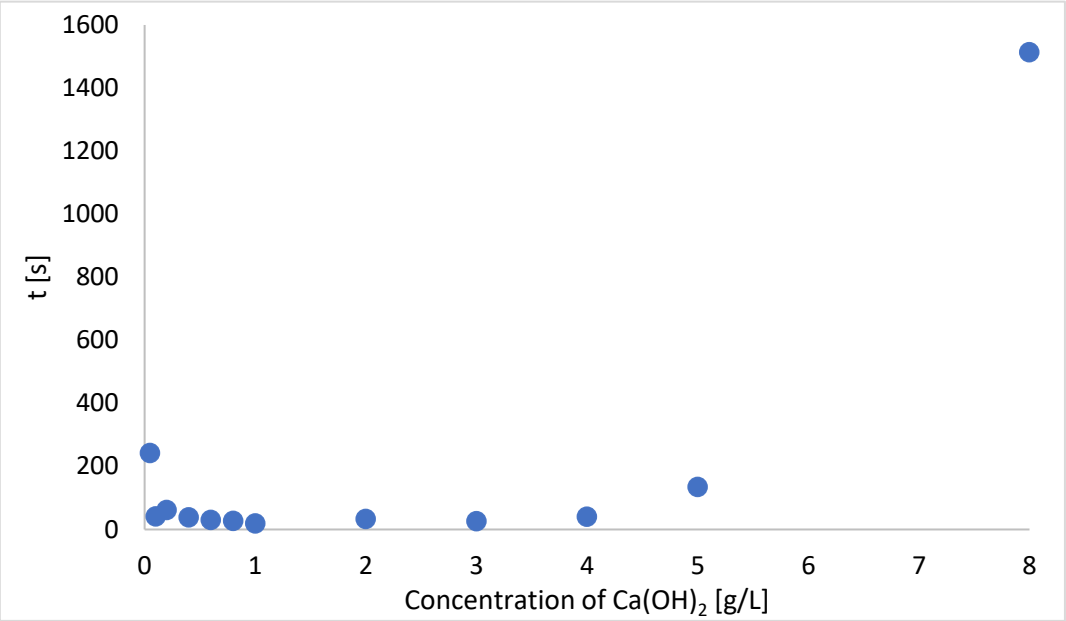

Figure 3.4. Time to reach the maximum pH, for different concentration, from the release of the calcium hydroxide.

The concentration affects the conductivity, reported in terms of increment (µS/cm) from the baseline of seawater. In this way, it is possible comparing variations of conductivity that would, otherwise, be compressed to the baseline value of seawater and appear difficult to identify. This representation of conductivity is the same across all the chapter of results.

In fig.3.5 the test with 8 g/L is out of scale, reaching a Δ of 6 014 µS/cm, after 3 000 seconds.

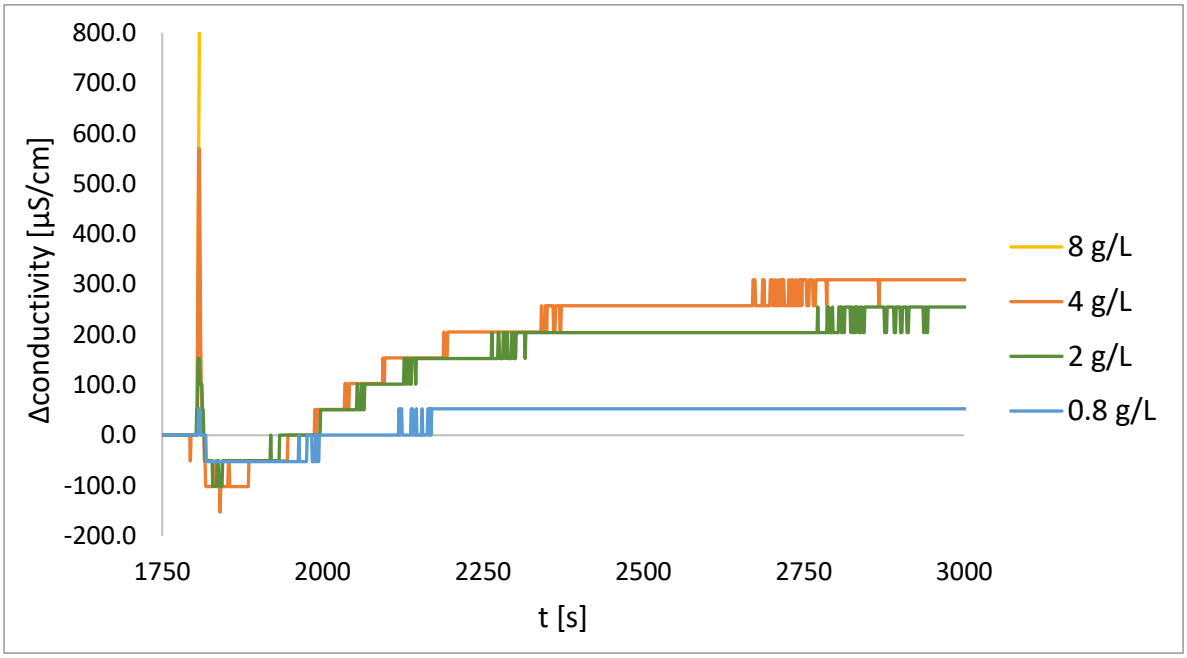

Figure 3.5. Change of conductivity for different concentrations of calcium hydroxide. In yellow it is reported the values for 8 g/L, in red 4 g/L, in green 2 g/L and in blue 0.8 g/L Release of hydroxide after 1 800 seconds. The experiment of 8 g/L is out of scale, reaching an increment of conductivity of 6,014 µS/cm, at 3 000 seconds.

From fig. 3.6 and it emerges that a significant increase of both pH and conductivity occurs for concentration of $Ca(OH)_2$ above 4 g/L. Fig 3.6 reports the maximum pH reached (right vertical axis) and the variation of conductivity (left vertical axis) as a function of the amount of calcium hydroxide released.

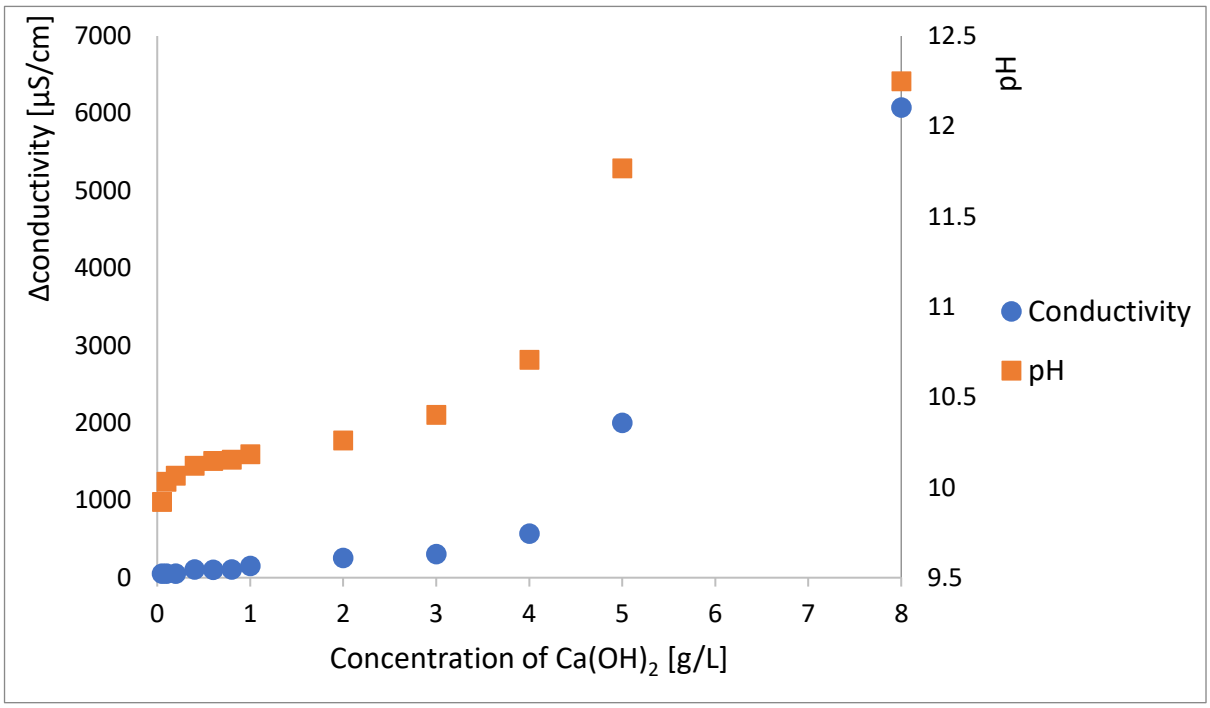

Figure 3.6. Maximum pH reached at different concentrations, represented as orange squares, and variation of conductivity during the experiments, blue dots.

3.2 Form of $Ca(OH)_2$

We test two ways of dissolving $Ca(OH)_2$ in seawater: a) as a dry powder, or b) as a slurry, upon mixing with seawater.

Usually, the measurements with powder show small delays, compared to the slurry. The latter is partly pre-diluted and, in general, results more homogeneous, the curves in fig. 3.7 show this delay. Additional elements to take into consideration are the surface tension of water and the variability caused by local effects near the sensor. In fig. 3.7 all the curves have the first value of pH different from the baseline (seawater alone) aligned at t= 1 800 s. This is particularly relevant for the curves obtained from powder where the delay caused by surface tension, that maintains the powder on the surface, is not negligible.

The data in the following section refer to trials performed with magnetic stirring agitation at the temperature of 25 °C.

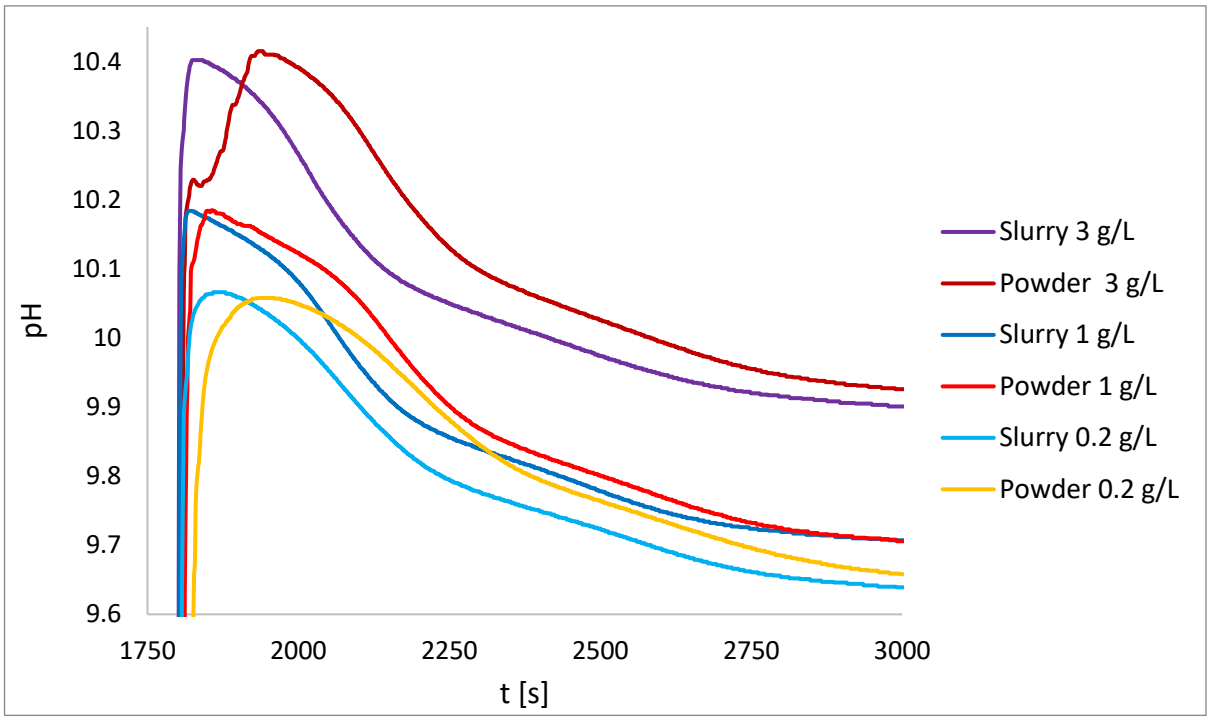

Figure 3.7. pH for 0.2, 1 and 3 g/L of $Ca(OH)_2$. Slurry is represented with cold colours while powders are shown with a warm palette. $Ca(OH)_2$ was released at t= 1 800 s.

Fig. 3.8 shows the difference between the powder, orange triangles, and the slurry, blue dots. The behavior is similar, but differences decrease at higher $Ca(OH)_2$ concentrations, although above 4 g/L, they start increasing again. Values at 8 g/L are excluded due to the fact that they do not reach a maximum of pH even long time after the end of the experiment at 30 minutes.

Tab 3.1 summarizes the pH comparison between powder and slurry.

From tab. 3.1 it emerges that slurry, on average, is 56% faster to reach pH maximum than powder and even the standard deviation of data regarding time is slightly lower. The % of pH decrease at t= 3 600 s, with respect to its registered maximum, are quite close.

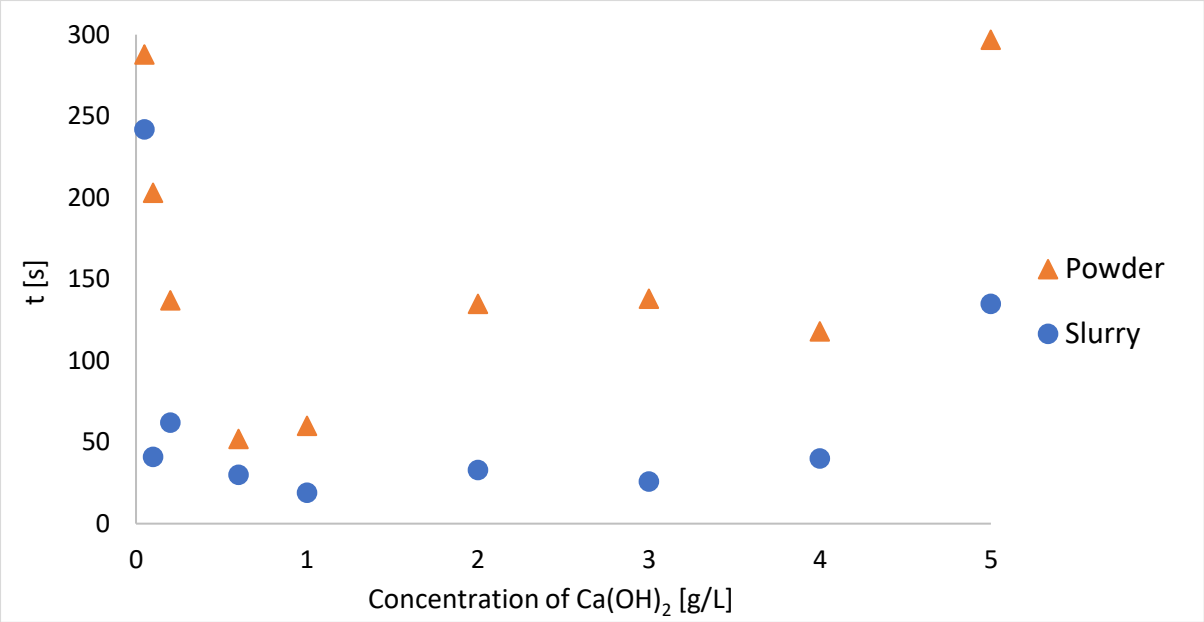

Figure 3.8. Comparison between powder (orange triangles) and slurry (blue dots) of the time to reach the maximum pH value of the experiments, at different concentration.

Table 3.1. Comparison between powder and slurry: time needed to reach the maximum pH value and % of pH value at 3 600 seconds with respect to the maximum value, concentrations at 0.05, 0.1, 0.2, 0.6, 1, 2, 3, 4, 5 g/L.

Powder			Slurry		
Concentration [g/L]	time pH peak [s]	% of pH at 3600 s	Concentration [g/L]	time pH peak [s]	% of pH at 3600 s
0.05	288	0.981	0.05	242	0.973
0.1	203	0.964	0.1	41	0.962
0.2	137	0.957	0.2	62	0.955
0.6	52	0.950	0.6	30	0.952
1	60	0.951	1	19	0.951
2	135	0.951	2	33	0.951
3	138	0.950	3	26	0.949
4	118	0.956	4	40	0.947
5	297	0.998	5	135	0.997
Average	158.7		Average	69.8	
Std	88.1		Std	73.4	

Another difference concerns the variation of conductivity: for high amounts of calcium hydroxide, (where the signal is amplified), a larger increase is registered compared with the slurry, fig. 3.9.

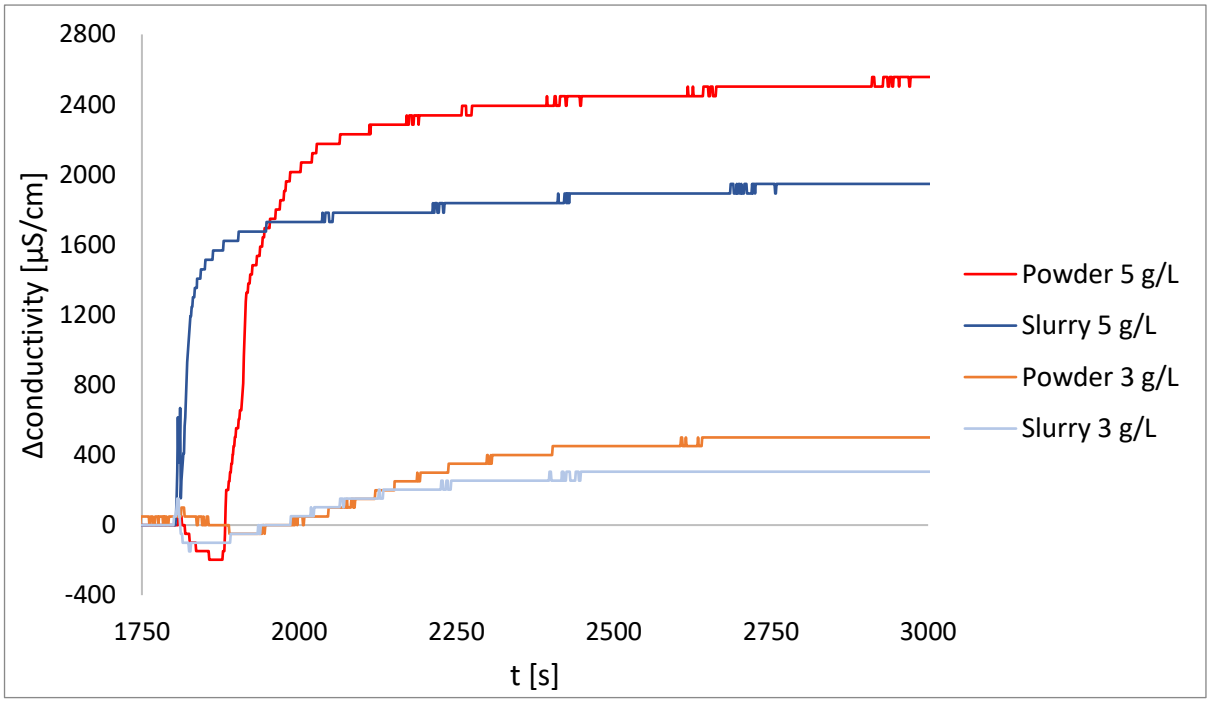

Figure 3.9. Variation of conductivity for 3 and 5 g/L. Slurry is represented with cold colours while powders are shown with a warm palette. $Ca(OH)_2$ was released at t= 1800 s

This difference is partly explained with the adding of water to form the slurry that dilutes the solution. A dilution means a minor effective concentration, respectively 4.80 instead of 5 g/L and 2.93 instead of 3 g/L. However, the dilution effect is not enough to explain the observed difference. It covers only 13.6% of conductivity difference between slurry and powder for 5 g/L and just 2.5% in the case of 3 g/L. These % refer to measurements of conductivity at t = 3 000 s.

3.3 Salinity

Three levels of salinity are tested: an average 35‰, which is the value of large oceans (Atlantic), 40‰, closer to high salinity seas like Mediterranean and 10‰, typical of seas with high freshwater inflows.

The data in the following section refer to tests performed with magnetic stirring, addition of calcium hydroxide in the form of slurry, and temperature of 25 °C.

Two figures for each concentration are reported: for low concentration, 3.10 and 3.12, and high concentrations fig 3.11 and 3.13.

In fig. 3.10 and 3.11, we see that the higher the salinity the lower the value of pH is.

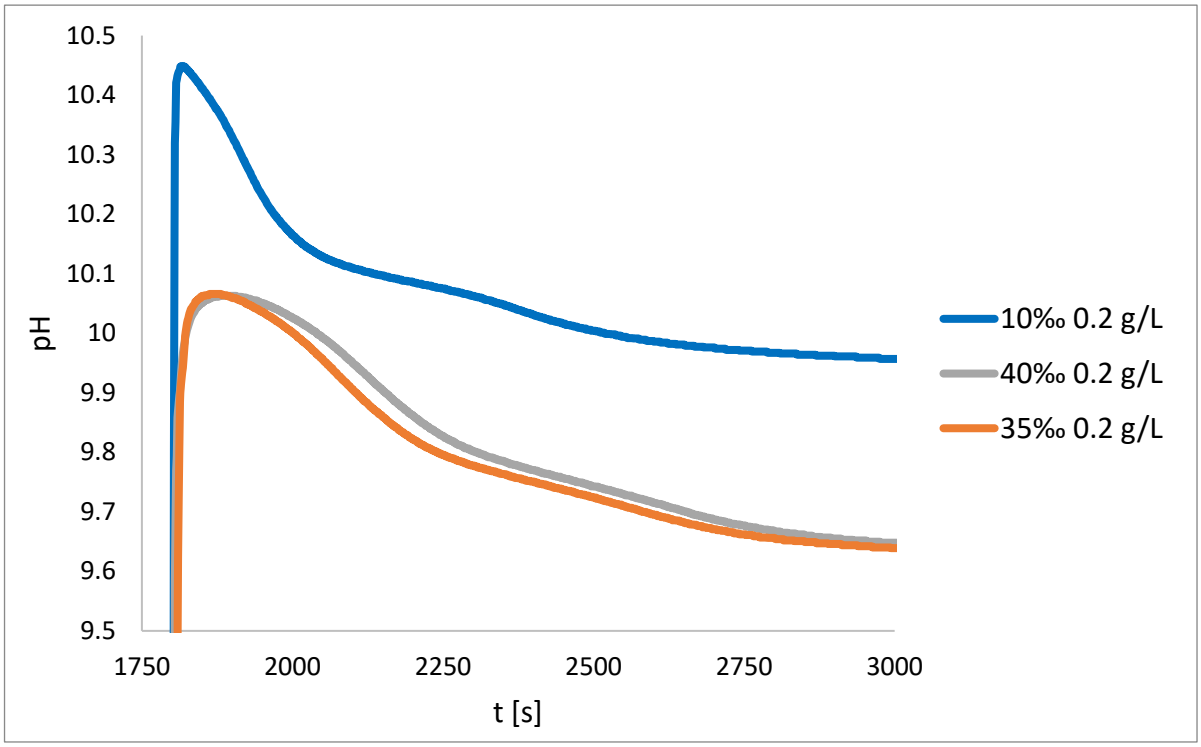

Figure 3.10. pH at concentration of 0.2 g/L. The blue curve indicates water at 10‰ salinity, the orange at 35‰ and grey at 40‰. $Ca(OH)_2$ was released at t= 1 800 s.

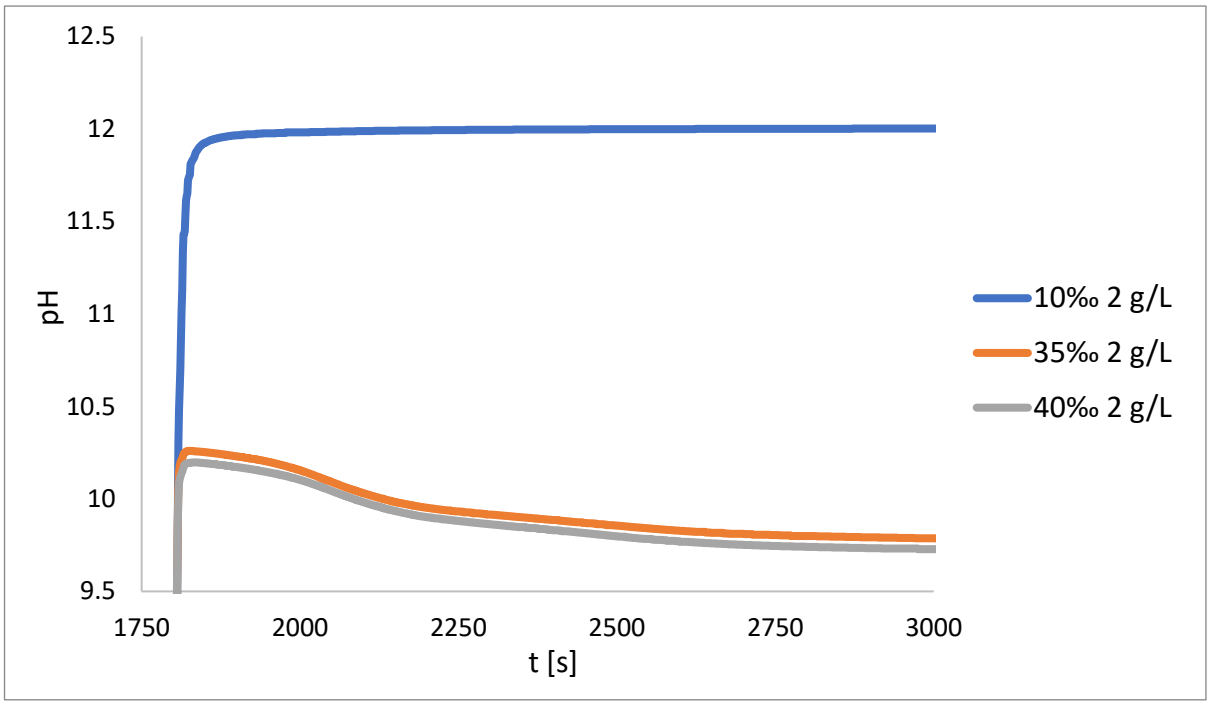

Figure 3.11. pH at concentration of 2 g/L. The blue curve indicates water at 10‰ salinity, the orange at 35‰ and grey at 40‰. $Ca(OH)_2$ was released at t= 1 800 s.

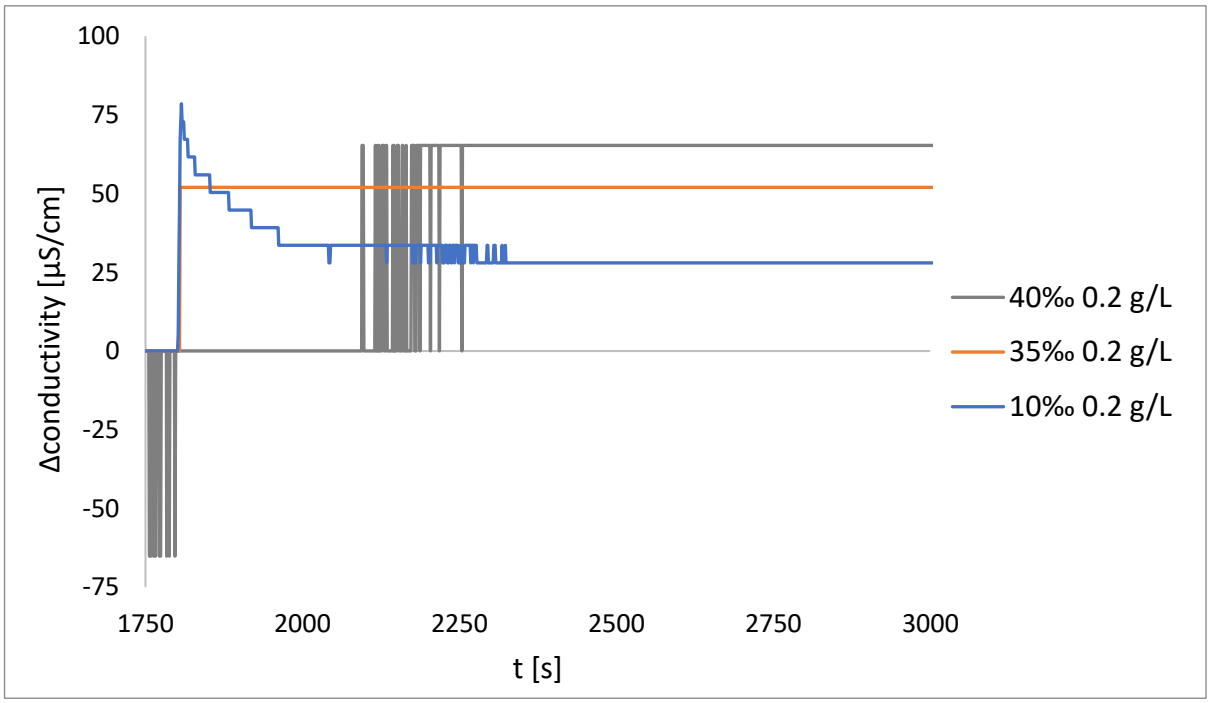

Figure 3.12. Variation of conductivity at concentration of 0.2 g/L. The blue curve indicates water at 10‰ salinity, the orange at 35‰ and grey at 40‰. $Ca(OH)_2$ was released at t= 1 800 s.

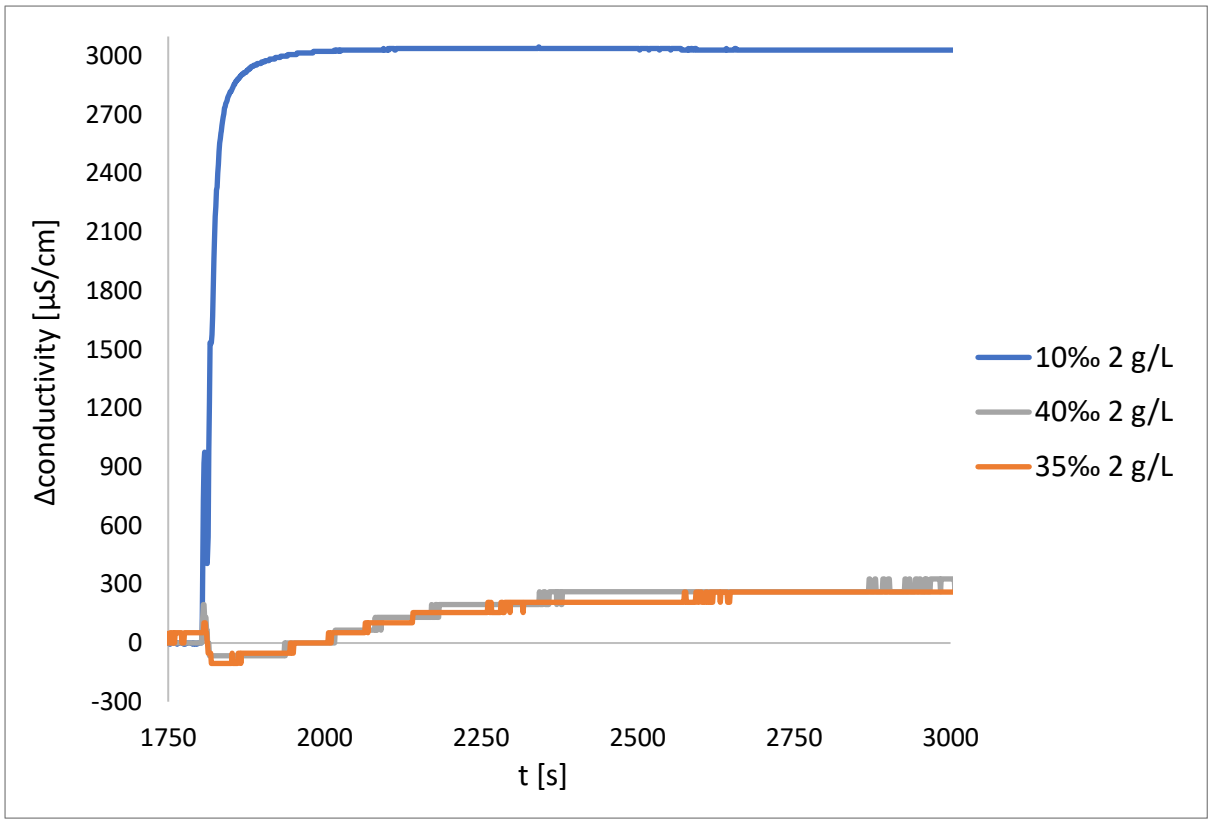

Figure 3.13. Variation of conductivity at concentration of 2 g/L. The blue curve indicates water at 10‰ salinity, the orange at 35‰ and grey at 40‰. $Ca(OH)_2$ was released at t= 1 800 s.

Considering conductivity, the concentration of 2 g/L shows clear difference of behaviour among the three salinities tested: the low salinity seawater reaches the highest increase of conductivity, fig. 3.13. A difficult interpretation, however, concerns the data shown in fig. 3.12. As order of magnitude, the variations are comparable among the three. However, as explained in section 2.5.2, a high concentration of salts decreases the sensitivity of the instrument, because of the increased overall conductivity. This leaves unclear whether the increase in the curve at 35‰ and 40‰, after $Ca(OH)_2$ release, is entirely ascribable at the increase of conductivity, or at the contribute of random temperature variations or evaporation.

Figure 3.14 offers an overview of salinities, showing the maximum value of pH reached during the trial for each concentration of $Ca(OH)_2$. pH peaks rise with increasing concentrations and the curves are placed in opposite order with their salinity. Highest recorded values of pH are those of the lowest salinity, 10‰, followed by 35‰ and 40‰. For each concentration, a rapid increment of the pH is observed, respectively around 2, 5 and 6 g/L for 10‰, 35‰ and 40‰ salinities.

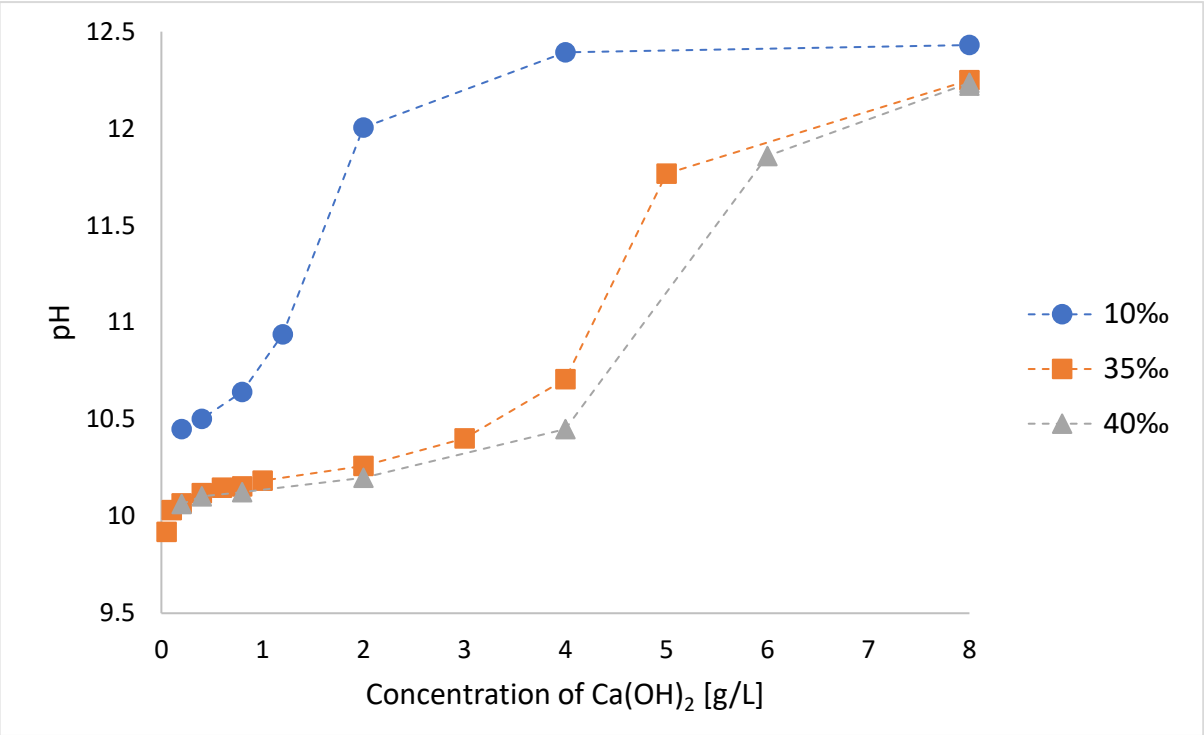

Figure 3.14. Maximum pH value reached during the experiment, for each concentration. The three series of data represent the tested salinities. The concentrations 0.2, 0.4, 0.8, 2, 4 and 8 g/L have been tested for each salinity, while additional tests were carried out with 0.05, 0.1, 0.2, 0.6, 1.2, 5 and 6 g/L only for some of them. $Ca(OH)_2$ was released at t= 1 800 s.

Tab. 3.2 reports the time needed to reach the pH peak, the maximum pH and the value of pH after 3 600 s, for the three salinities and concentrations at 0.2, 0.4, 0.8, 2, 4 and 8 g/L.

Tab. 3.2 shows a clear tendency: until the pronounced pH increase at $Ca(OH)_2$ concentration of 2 g/L for 10‰ seawater, the lowest salinity water is the fastest to reach the peak for 0.2, 0.4 and 0.8 g/L. This behaviour stops when the pH seems to "saturate" (at 2 g/L). For higher concentration, it is the high salinity seawater to reach the pH peak faster.

Table 3.2. Time needed to reach the maximum pH value and % of pH value at t= 3 600 s with respect to the maximum value, for concentrations of 0.2, 0.4, 0.8, 2, 4, 8 g/L

	10‰		35‰		40‰	
Concentration [g/L]	time pH peak [s]	pH peak	time pH peak [s]	pH peak	time pH peak [s]	pH peak
0.2	16	10.449	62	10.066	78	10.063
0.4	19	10.502	38	10.120	35	10.103
0.8	29	10.641	27	10.154	26	10.125
2	1 505	12.004	33	10.260	30	10.198
4	1 400	12.394	40	10.707	46	10.450
8	1 405	12.429	1 513	12.250	1 143	12.236

3.4 Stirring

Two methods are tested to mix the solution, a mechanical impeller and a magnetic stirring. The mechanical agitation tries to simulate an imperfect mixing, closer to the real condition of the sea, while the magnetic one, kept constant at 360 rpm, performs a more homogeneous mixing, but far from actual agitation. The speed of rotation of the former is selected after analysing the results performed at 50, 100 and 200 rpm.

As expected, a higher rotational speed ensures better mixing. In order to see differences with respect to the common magnetic stirring, a compromise is necessary between very high speed (too rapid mixing) and very low speed, for which the addition, either in form of powder or slurry, precipitates immediately at the bottom of the beaker without any dissolution. The choice of 100 rpm represents a good, although not perfect, mixing.

It is noteworthy that, to simulate higher volume of water around the impeller, all the tests performed with the mechanical agitation are made in beakers containing 2 litres of seawater. Two positions of the impeller were tested: on the surface or partially immersed in the solution. No remarkable difference was observed.

The data in the following paragraph refer to tests performed adding calcium hydroxide in the form of slurry with the impeller placed at half of the height of the solution.

The two mechanisms show similar behaviours, however the dissolution for the mechanical stirring is less effective than the other one: at equal concentrations, the pH takes more time to reach the peak at lower values, see figure 3.15. At the end of the experiment, after 30 minutes, a difference of pH between the two types of agitations is still observed but the values of the mechanical stirring are closer to magnetic ones.

Like the pH, the conductivity shows lower values measured for the mechanical agitation with respect to the magnetic stirring case, fig. 3.16. Some of the experiments data are summarized in tab. 3.3.

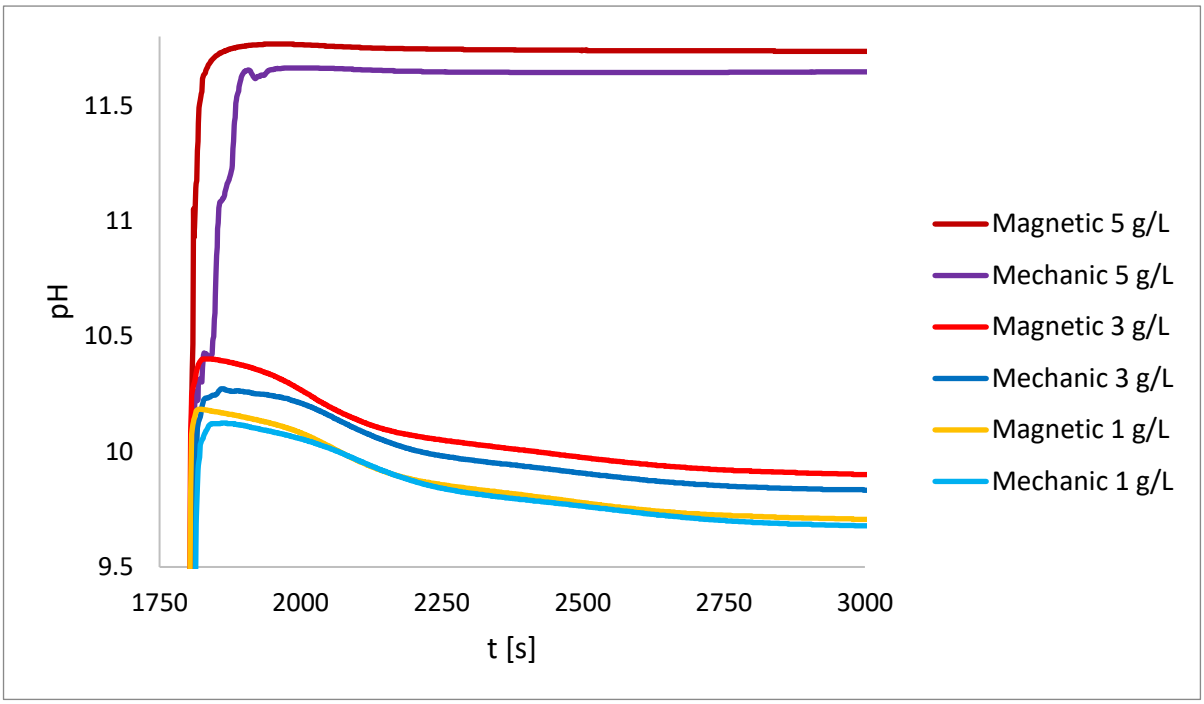

Figure 3.15. pH measure to compare magnetic and mechanical agitation. Magnetic agitation is represented with warm colours while mechanical agitation is shown with a cold palette. $Ca(OH)_2$ was released at t= 1 800 s.

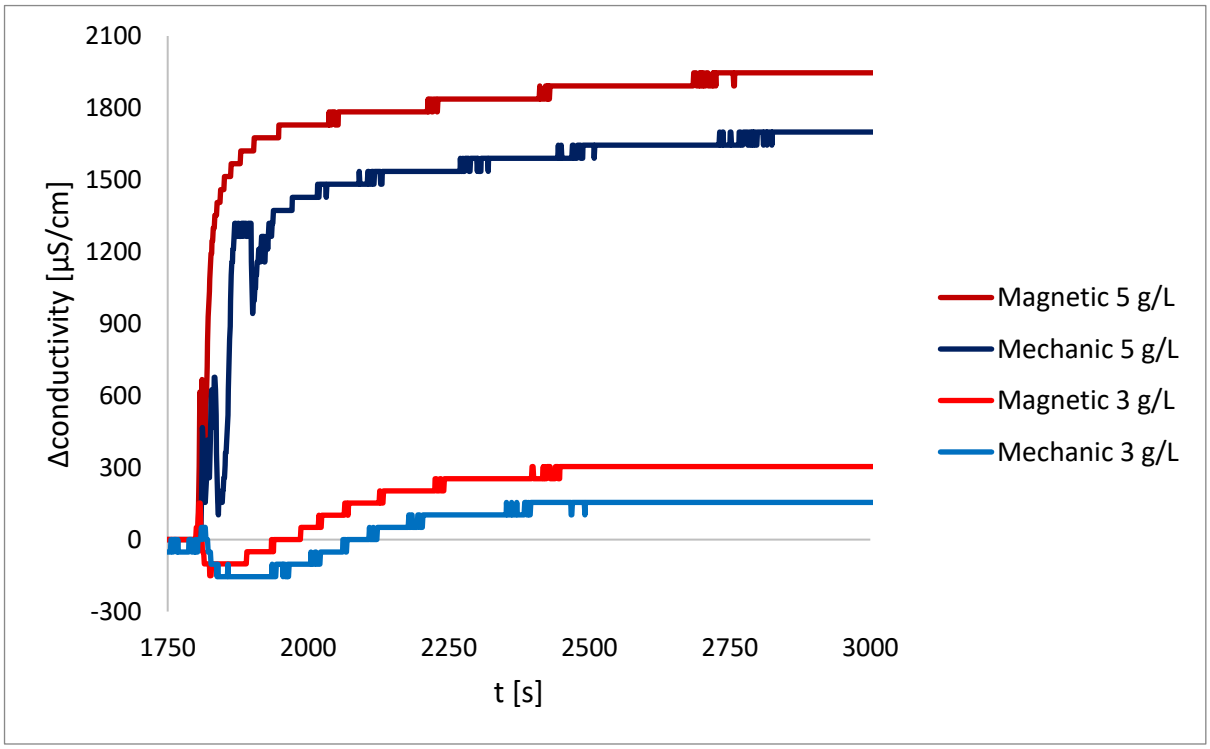

Figure 3.16. Same as in figure 3.15, but referring to conductivity.

Table 3.3. pH peak and its time needed to reach the maximum value, concentrations at 0.2, 0.6, 1, 3, 5 g/L.

	Magnetic		Mechanical	
Concentration [g/L]	pH peak	pH peak time [s]	pH peak	pH peak time [s]
0.2	10.066	62	10.054	127
0.6	10.147	30	10.120	51
1	10.184	19	10.124	59
3	10.402	26	10.272	59
5	11.767	135	11.664	170

3.5 Temperature

Four temperatures are tested to evaluate the dissolution of calcium hydroxide in seawater. The seawater employed has a salinity of 35‰ and stirring is performed with a magnetic bar.

From fig. 3.17 and 3.18 a trend is observed: as the temperature decreases, the pH is higher. Fig. 3.19 displays the highest pH reached as function of the concentration of $Ca(OH)_2$.

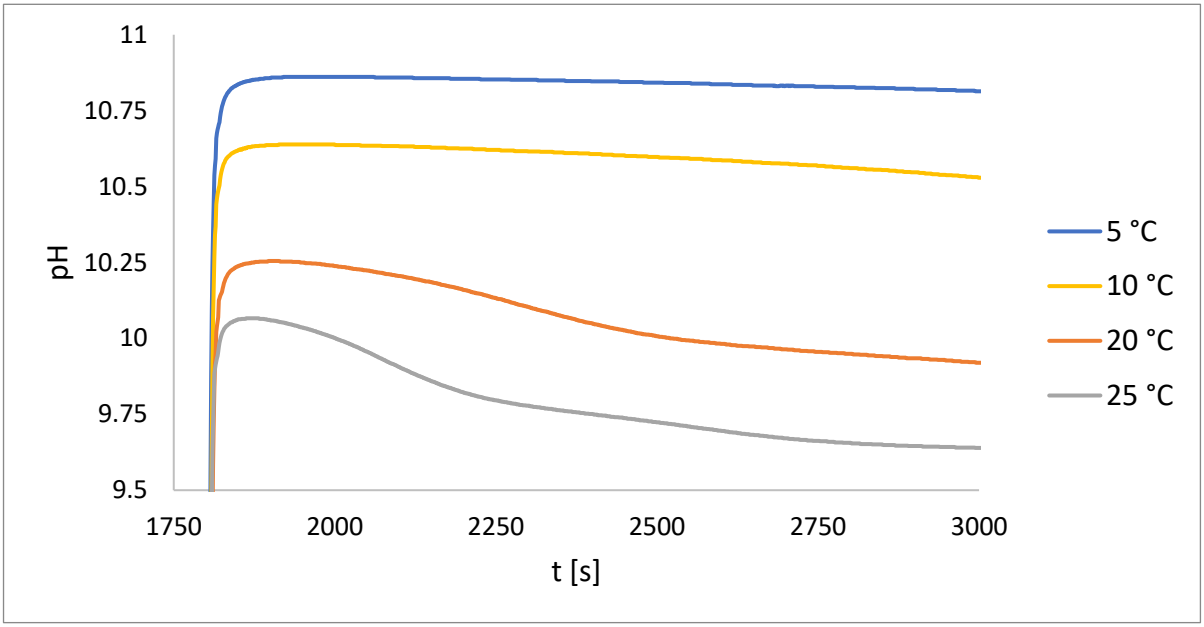

Figure 3.17. pH measurement for different temperature with a concentration of 0.2 g/L of $Ca(OH)_2$,. The temperature is ordered from the lowest curve (25°C) to the uppest (5°C) in descending order. $Ca(OH)_2$ was released at t= 1 800 s.

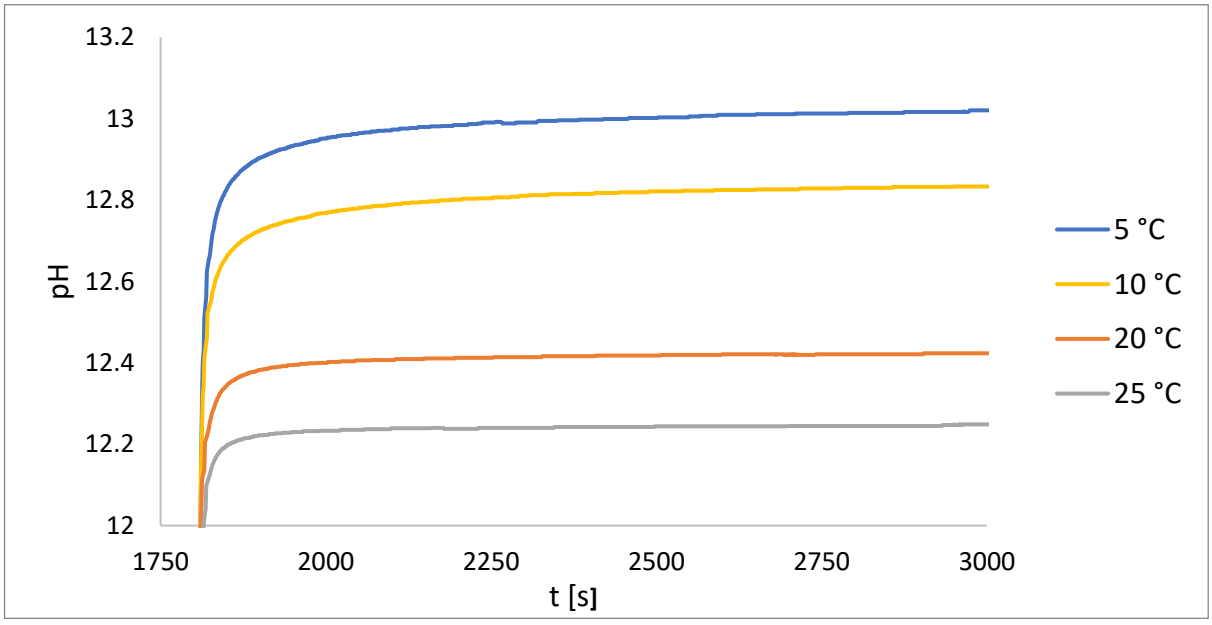

Figure 3.18. pH measurement for different temperature with a concentration of 8 g/L of $Ca(OH)_2$,. The temperature is ordered from the lowest curve (25°C) to the uppest (5°C) in descending order. $Ca(OH)_2$ was released at t= 1 800 s.

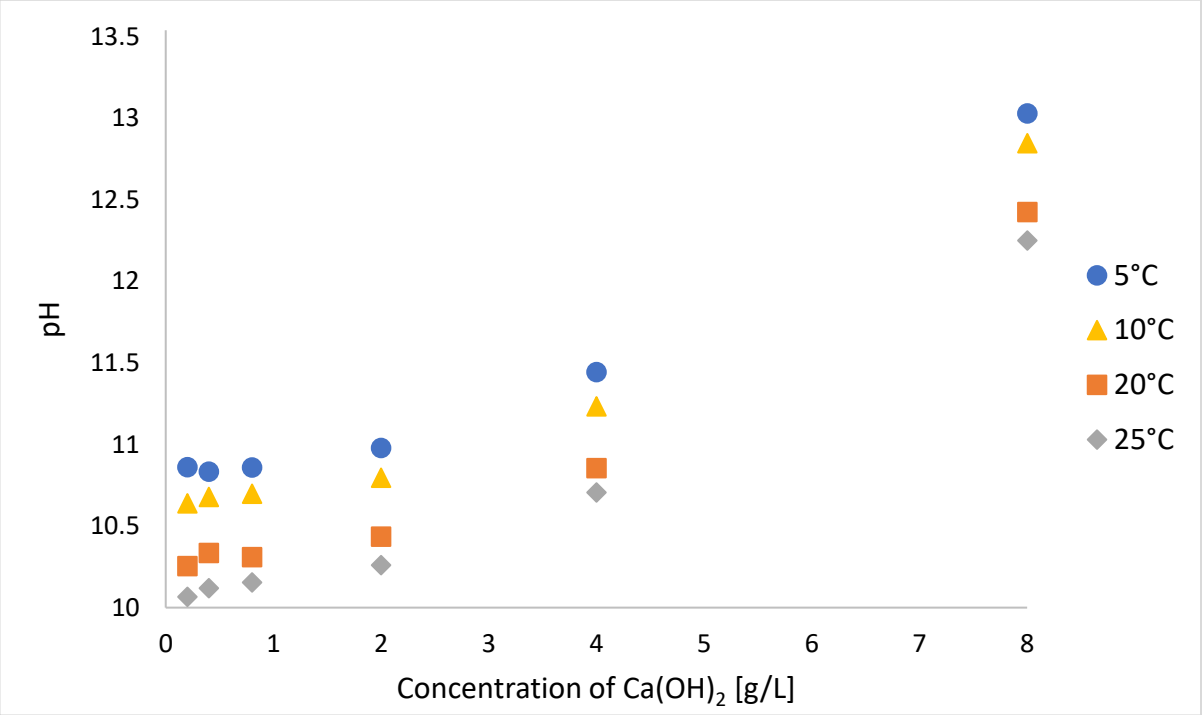

Figure 3.19. Maximum pH reached, during the experiment, for different concentration. Each temperature is represented by a different symbol.

The interpretation of conductivity measurements is complex, due to the limitations discussed in section 2.3 and 2.5.2.

At low concentrations of $Ca(OH)_2$ (0.2, 0.4 g/L), it does not emerge a clear tendency. At 0.8 g/L the behaviour is similar to 8 g/L (as shown in fig. 3.21, with the curves ordered inversely to their temperature). At 2 and 4 g/L, instead, the pH curves are ranked with the highest increments belonging to the highest temperatures (fig. 3.20, 2 g/L).

The measure of conductivity can be interpreted as an indicator of presence of conductive ions in the solution. Data in fig. 3.21, well above the saturation limit of $Ca(OH)_2$, suggest that the reaction of dissolution may be favored at low temperatures. This hypothesis is confirmed also looking at the standard enthalpies of formation of the reactions, eq. 43 and 44.

$$Ca(OH)_2 \leftrightharpoons Ca^{2+} + 2OH^- \tag{43}$$

$$\Delta H_f = 2 \cdot \Delta H_{OH^-(aq)} + \Delta H_{Ca^{2+}(aq)} - \Delta H_{Ca(OH)_2(s)} = -16.72 \frac{kJ}{mol} \tag{44}$$

As the resulting value is negative, the reaction is exothermal (NIST Chemistry WebBook), i.e. generates heat, and according to Le Chatelier's principle, decreasing the temperature favors the forward reaction (the dissolution of $Ca(OH)_2$) which raises the number of ions in the solution.

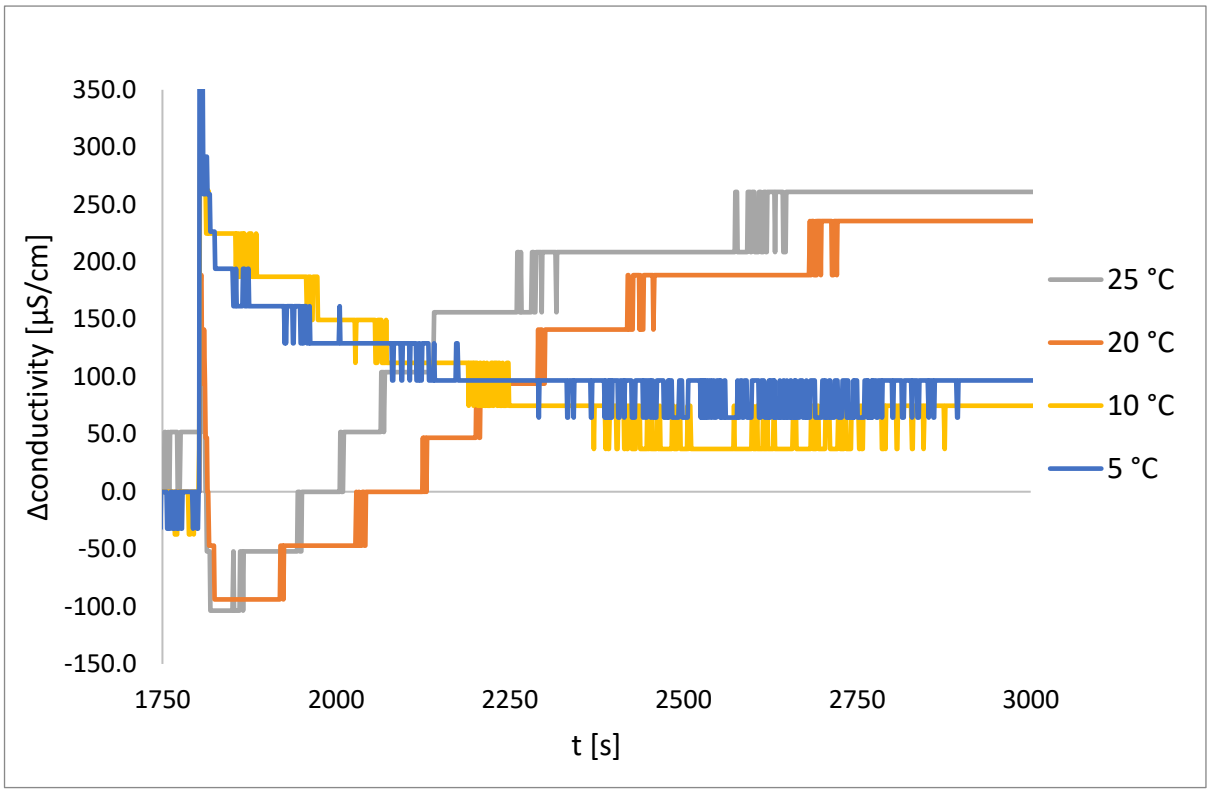

Figure 3.20. Variation of conductivity for 2 g/L of $Ca(OH)_2$ at different temperatures. Release of calcium hydroxide at t= 1 800 s.

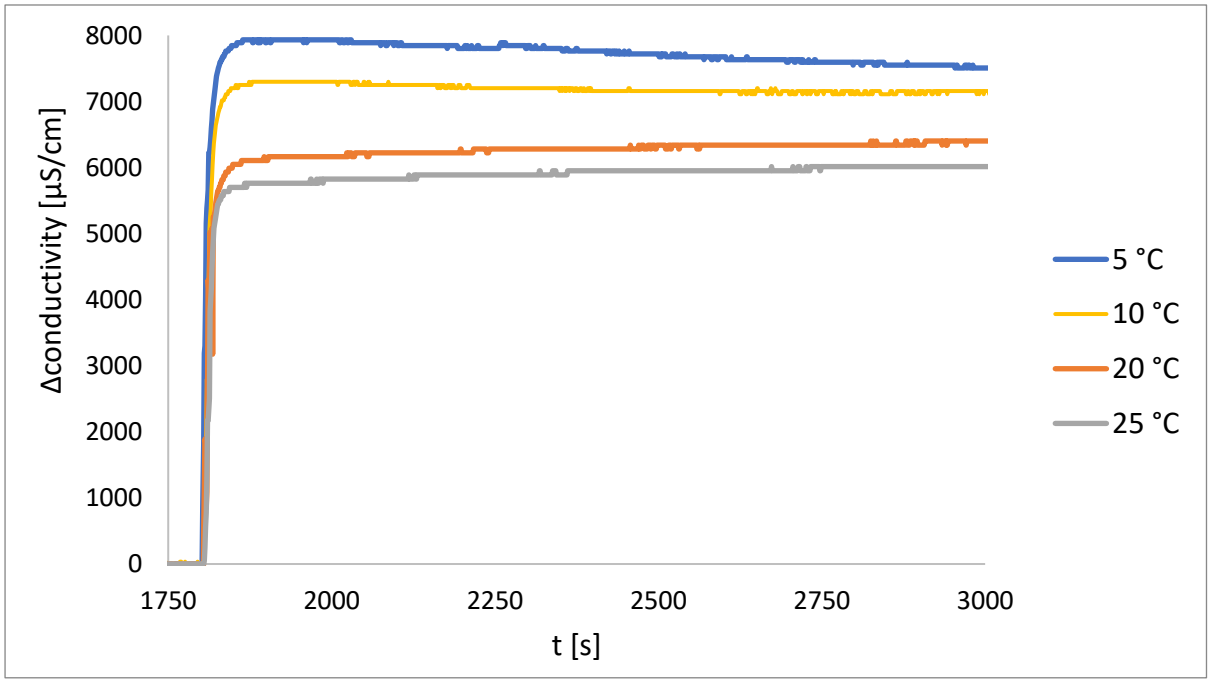

Figure 3.21. Variation of conductivity for 8 g/L of $Ca(OH)_2$ at different temperatures. Release of calcium hydroxide at t= 1 800 s.

3.6 Alkalinity measurements

The alkalinity estimation is performed through an automatic titrator (Hanna Instruments HI-84531), as described in section 2.5.4.

At the beginning, to test the consistency of the data, a sample of seawater is analyzed, obtaining, as a result, a value below the lower detectable limit. Artificial seawater employed, has, in fact, alkalinity close to zero.

First attempts are made extracting samples from the solution, kept in agitation, proceeding directly with titration. Fig. 3.22 shows the results obtained from powder, blue dots, and slurry, orange triangles, at different concentrations of $Ca(OH)_2$. The samples are extracted from the solution when the pH reaches its peak. The points align on a straight line, with slightly higher values for slurry. The results at concentration of 5 g/L are obtained using just 25 ml of the solution while at 8 g/L the amount was 20 ml.

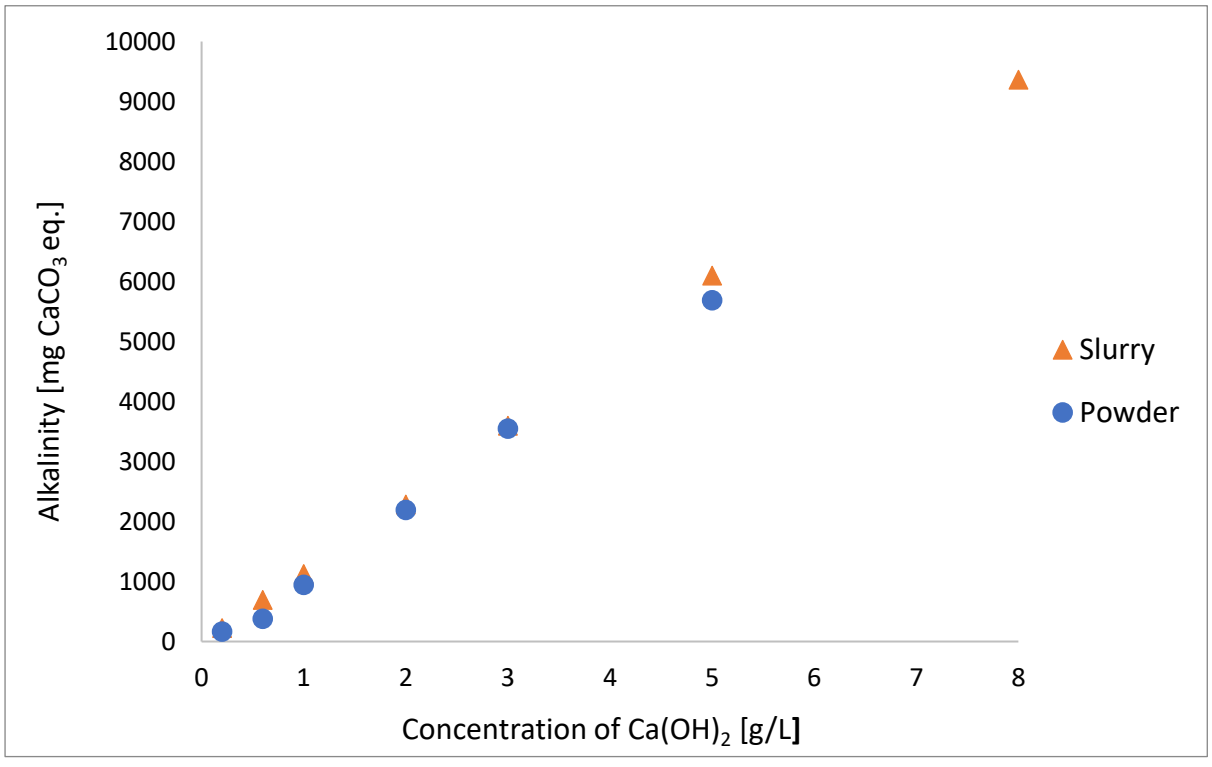

Figure 3.22. Comparison of alkalinity results, without filtration, between slurry (orange squares) and powder, (blue dots). Concentrations at 0.2, 0.6, 1, 2, 3 ,5 g/L. Additional value at 8 g/L for slurry.

The straight line, even at high concentrations, is not what expected as it was thought that, above a fixed concentration threshold, a saturation phenomenon would have occurred.

This suggests that, with that titration procedure, the adding of HCl progressively make the solution more acidic, favouring dissolution of undissolved or previously precipitated particles.

To avoid this, all the results hereinafter presented are obtained after a filtration (single or double) of the solution performed through a Büchner funnel with a paper filter inside. The funnel is connected to a side-arm flask by means of an adapter, with a rubber tube leading to a vacuum pump, fig. 3.23. The pump speeds up the process, sucking the solution through the filter.

Figure 3.23. Büchner funnel used for solution filtering. A paper filter is shown beside the side-arm flask. The rubber tube is connected to a vacuum pump.

With this procedure a new test is planned. Starting from 1 litre of seawater, 4 g of $Ca(OH)_2$, slurry, are released. The solution is at 20 °C and kept, with magnetic stirring, at 360 rpm. Four samples are extracted and filtered: the first at the time the pH reaches its maximum, then, at 30 minutes, 1 hour and 3 hours from the release. Part of the filtered solutions at pH peak and 30 minutes is used immediately in the titration, while the remaining is kept, under agitation, for 6 hours since the release of calcium hydroxide.

After 6 hours, the unfiltered, original solution is filtered and titrated. This procedure, filtering and titration, is repeated also for the samples taken at the pH peak and after 30 minutes, already filtered and left under stirring.
Tab. 3.4 summarizes the results for the alkalinity, all expressed in mg $CaCO_3$ equivalent. Two values are reported for the alkalinity after 6 hours: due to the number of magnetic stirrers available, the experiment had to be repeated twice.

Table 3.4. Comparison of pH values between 1st and 2nd filtration at different time steps.

Time of samples extraction	pH peak	30 minutes	1 hour	3 hours	6 hours	
1st filtration	81.3	912.75	1499	859	508.4	638
	at the 6th hour from $Ca(OH)_2$ release					
2nd filtration	31.4	127.5	/	/	/	/

What emerges from tab. 3.4 is that the value of alkalinity, considering just the first filtration, evolves in time with a sharp increase and a subsequent slow decrease.
Looking instead at the results after the 2nd filtration, it is clear that some precipitation occurs during time. The precipitation is captured by the filter leading to values of alkalinity 61% and 86% lower.
The consistency of data and the repeatability of the experiment is, however, not perfect: the double value at 6 hours shows a 20% variation from a trial to another.

After this another test is implemented: the evolution of results is studied under different concentrations of $Ca(OH)_2$ released, in particular 1, 4, 5 and 8 g/L, in slurry form. For the first two concentrations 0.5 L of seawater at the temperature of 20 °C and magnetic stirring at 360 rpm are used. Due to the time employed for filtering, (that affects the final result of alkalinity) just 0.25 L are used to test 5 and 8 grams of $Ca(OH)_2$. Filtrations and following titration are performed just when pH reaches its peak.
In these experiments it is calculated also the total amount of filtered matter once the filter, previously weighted, has dried out of the water. All the results in that part are rescaled to a hypothetic 1 litre of solution, multiplicative factors are, respectively, 2x for 0.5 L and 4x for 0.25 L solutions.

All the above-cited methods and procedures are used, moreover, for a single trial at 4 g/L in powder form. The reason behind this is a possible matter precipitation during the slurry preparation that we want to avoid.

Fig. 3.24 shows the alkalinity measured for four different concentrations of $Ca(OH)_2$: 1, 4, 5 and 8 g/L. The shape resembles the conductivity in fig. 3.6.

Fig. 3.25, presents the total amount of filtered matter rescaled on 1 litre solution.

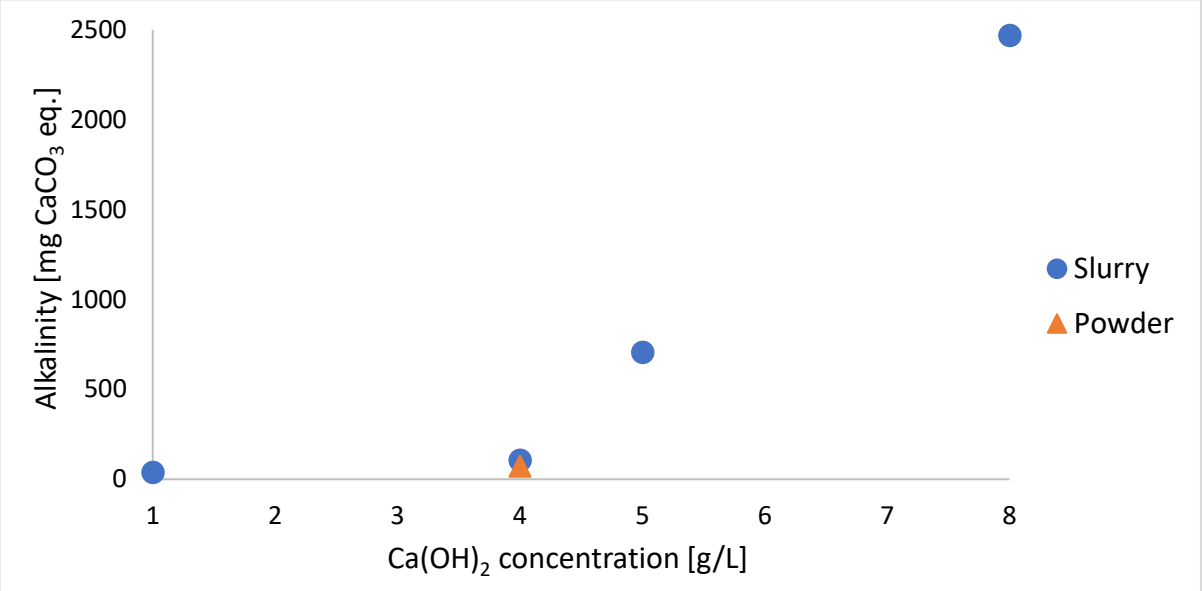

Figure 3.24. Comparison of alkalinity values at concentrations of 1, 4, 5 and 8 g/L. Blue dots represent slurry measurements while the orange triangle is the measure for powder, (4 g/L).

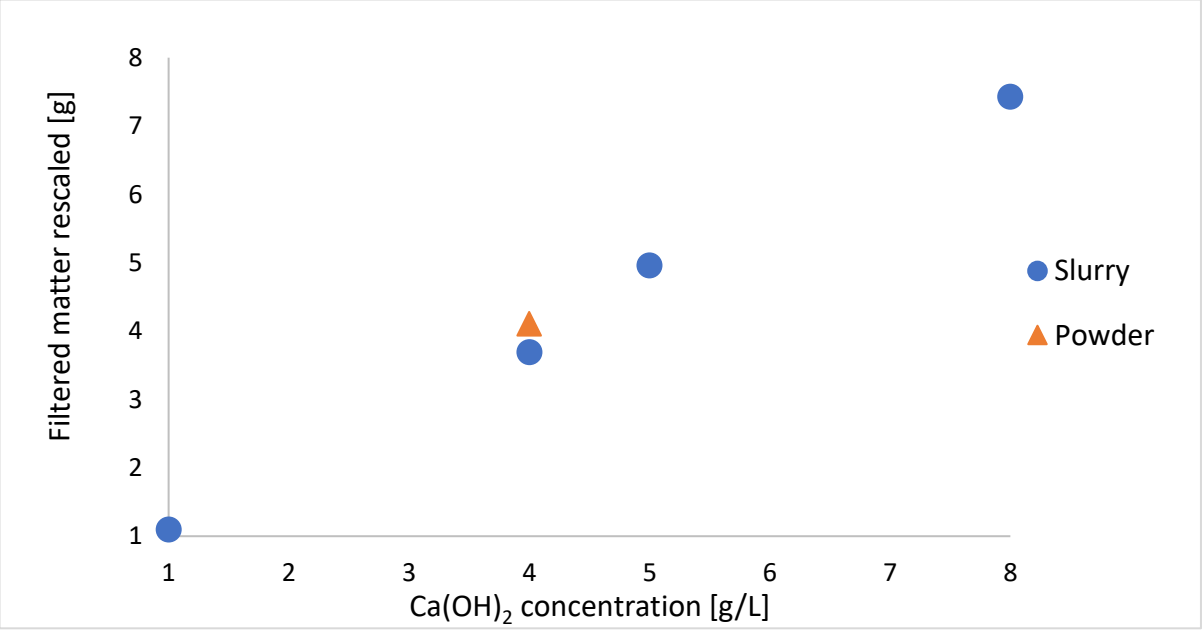

Figure 3.25. Comparison of the mass of filtered matter at concentrations of 1, 4, 5 and 8 g/L. Blue dots represent slurry measurements while the orange triangle is the measure for powder, (4 g/L).

The results of fig. 3.24 and 3.25 are summarized in tab. 3.5.

Table 3.5. Numerical summary of the results represented in fig. 3.24 and 3.25.

Volume of the solution [L]	**$Ca(OH)_2$ concentration [g/L]**	**Form**	**Alkalinity [mg $CaCO_3$ eq.]**	**Multiplicative factor**	**Filtered matter rescaled [g]**
0.5	4	Powder	72	2x	4.10
0.5	1	Slurry	38.4	2x	1.10
0.5	4	Slurry	105.3	2x	3.69
0.25	5	Slurry	706	4x	4.96
0.25	8	Slurry	2 470	4x	7.43

From fig. 3.25 it emerges that there is close correspondence, in terms of mass, between the amount of $Ca(OH)_2$ released in water and the mass extracted from the filter. As the amount of filtered matter is slightly higher, for the powder case at 4 g/L, with respect to the slurry, there is no significant variation in the process of precipitation.

3.7 X-ray diffraction

The X-ray diffraction technique is applied to the powders resulting from the Buchner filtration process. Once dried and prepared for the experiment, the sample is analyzed by means of a X-ray powder diffractometer, equipped with Cu Kα radiation source, in the 2θ range 10-70°. The diffraction experiments are performed on samples with different $Ca(OH)_2$ concentrations, 1, 4 and 8 g/L in slurry form and powder at 4 g/L. Tests at different filtration times from the release of calcium hydroxide are carried out too.

Before investigating those samples, the $Ca(OH)_2$ powder itself was tested, to check its purity having literature values as reference (Rruff Database). Figure 3.26 shows a clear consistency between the two spectra of $Ca(OH)_2$; however, traces of calcite (a polymorph form of $CaCO_3$) and coesite (a polymorph form of SiO_2) are found. The latter is not shown in fig. 3.26, because the observed peaks fall outside the displayed range.

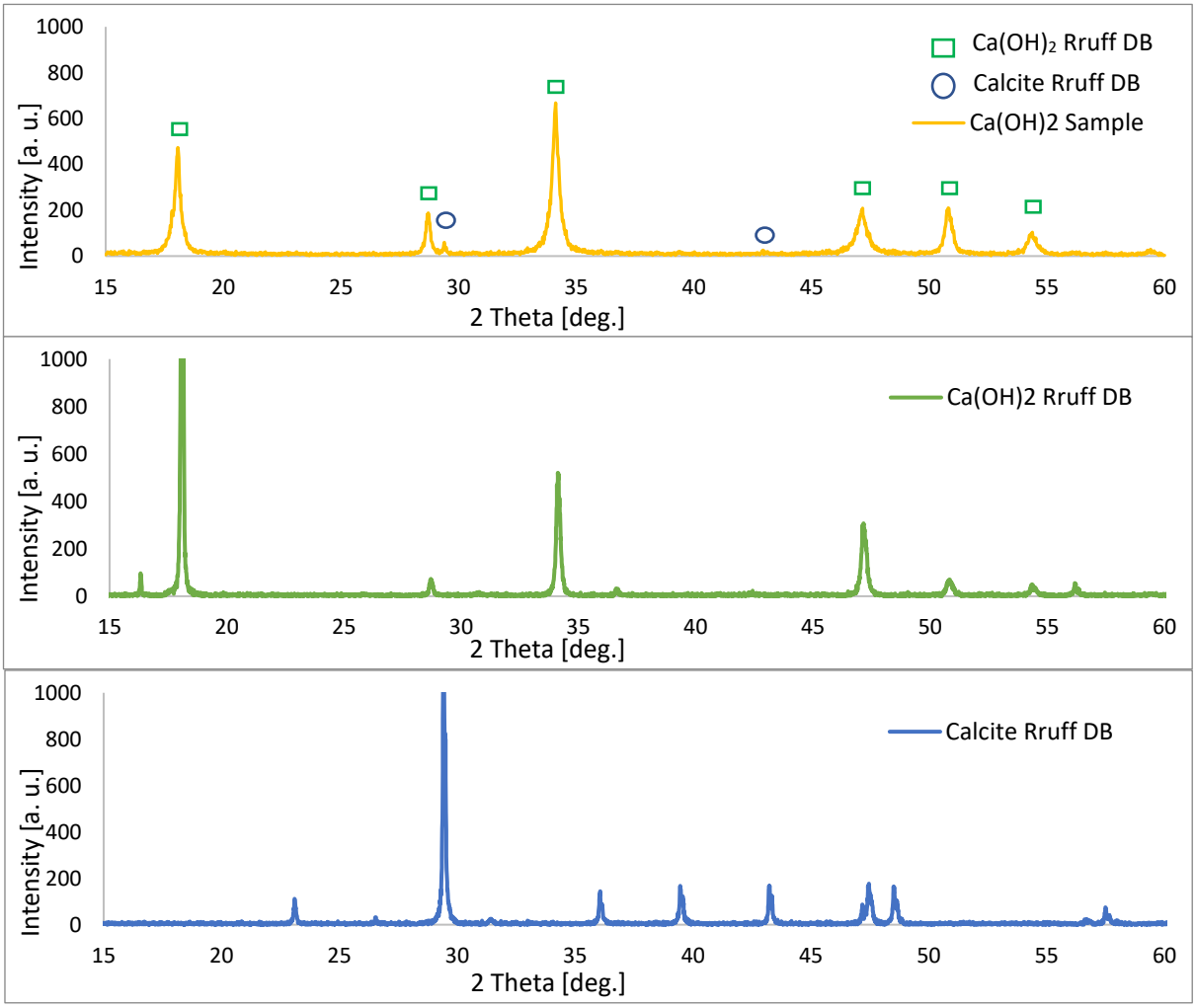

Figure 3.26. Diffraction pattern of calcium hydroxide sample and relative matching pattern of calcium hydroxide and calcite.

The main phases of the filtered matter, represented by peaks of fig. 3.27, are: calcite, brucite (magnesium hydroxide) and sodium chloride. Noteworthy, sodium chloride is not directly linked with the calcium hydroxide addition and it is due only to the salt in seawater. Other compounds, aragonite (mineral made by $CaCO_3$) and cristobalite (polymorph mineral, SiO_2), are found in traces. Instead, the diffraction pattern of $Ca(OH)_2$ is not detected.

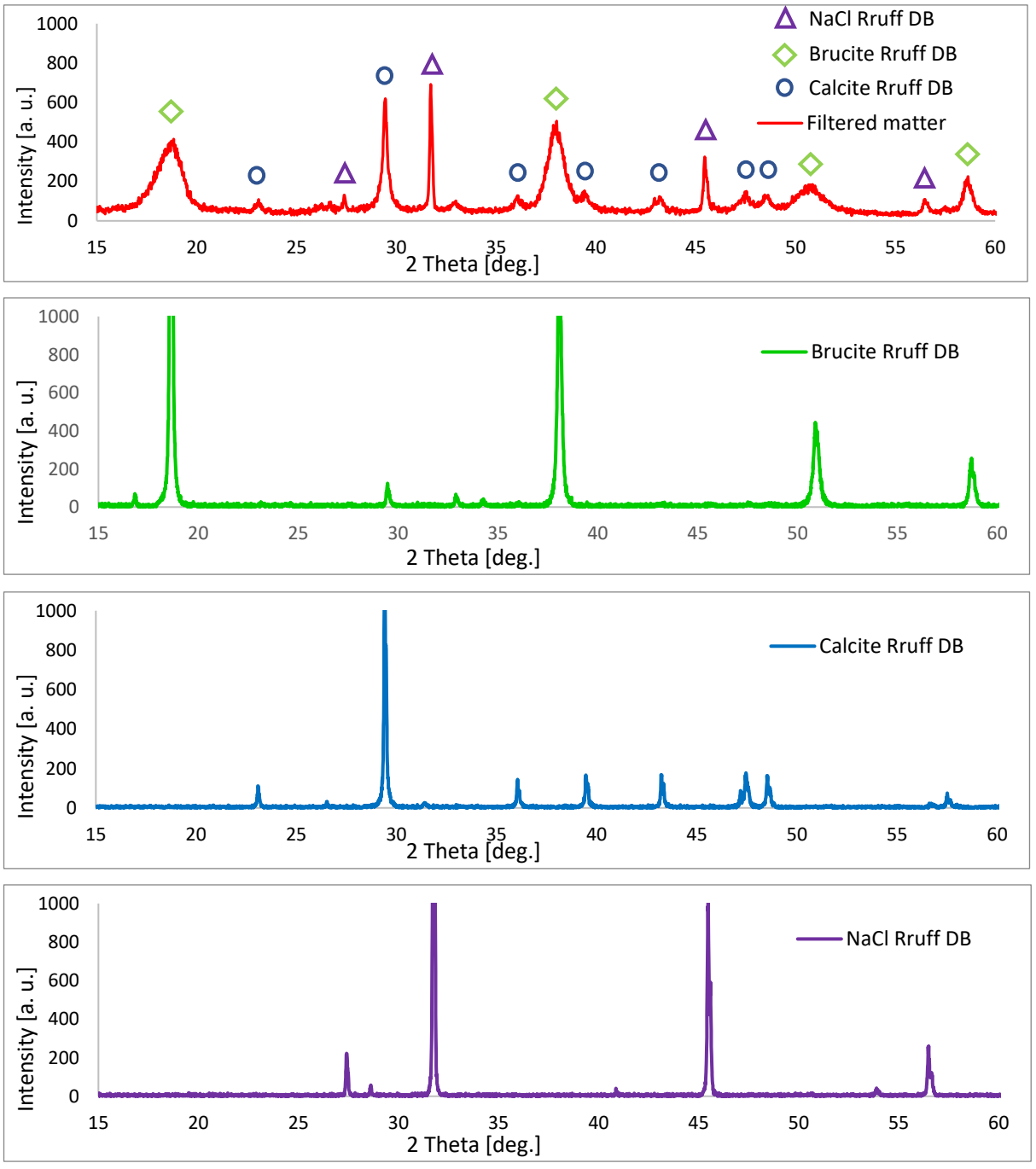

Figure 3.27. Diffraction pattern of the filtered matter of seawater with $Ca(OH)_2$ diluted. Sample obtained using a concentration of 8 g/L and calcium hydroxide in form of slurry. Brucite and NaCl graphs limited in the figures to 1 000 (a. u.).

Different concentrations are tested, 1, 4 and 8 g/L in fig. 3.28. Between 1 and 4 g/L, a small increase of the peaks is observed but no significant variation of the phases. The 8 g/L experiment shows a variation of the proportions between the phases, the brucite decreases in favour of the calcite. The NaCl increases as well. In addition, an unknown impurity is detected at 44,6°, growing its intensity as the concentration decreases.

The experiments performed at different times from the release of $Ca(OH)_2$, show no significant differences. This implies that the time does not influence the formation of different phases.

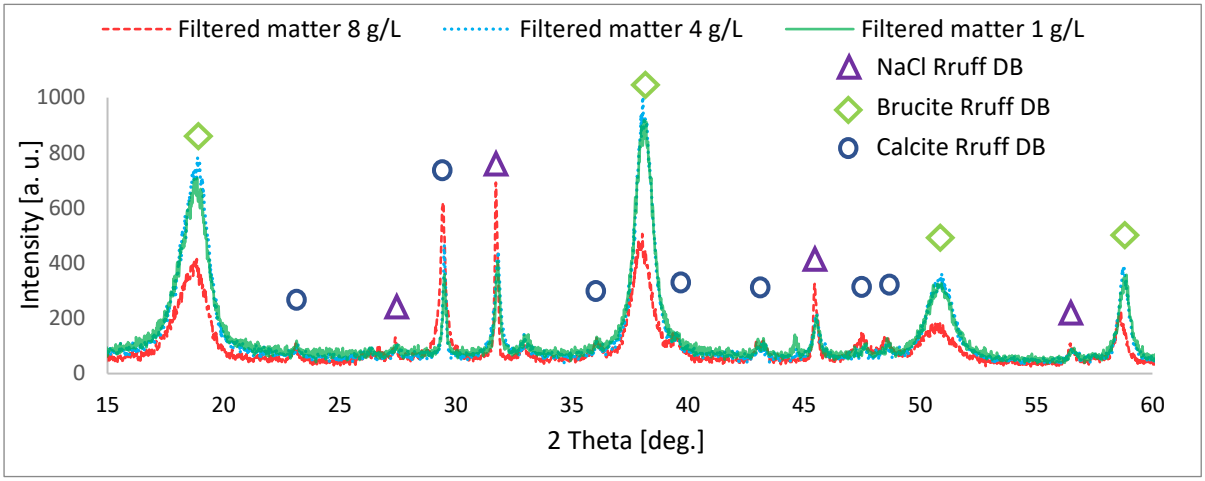

Figure 3.28. Diffraction pattern of filtered matter, for different concentrations (1, 4, 8 g/L) of $Ca(OH)_2$ diluted. Sample obtained using calcium hydroxide in form of slurry.

The formation of brucite, $Mg(OH)_2$, could be responsible for the "fastest" decrease phase of the pH of fig. 3.2. The same data, plus the concentrations at 0.2 g/L are reported in fig 3.29, the conditions of the experiment are: temperature 25 °C, slurry from and magnetic stirring. In fig. 3.29 it is clearly visible the point where the trend changes its decreasing pace, around 2100-2200 s.

At that time the precipitation of brucite, characterized by small crystals, as it can be understood from the spectra of fig. 3.28, may be ended. From that moment on, we presume that the predominant responsible for the pH decrease becomes the CO_2 absorption from the atmosphere into the solution. Anyway, further investigation is needed.

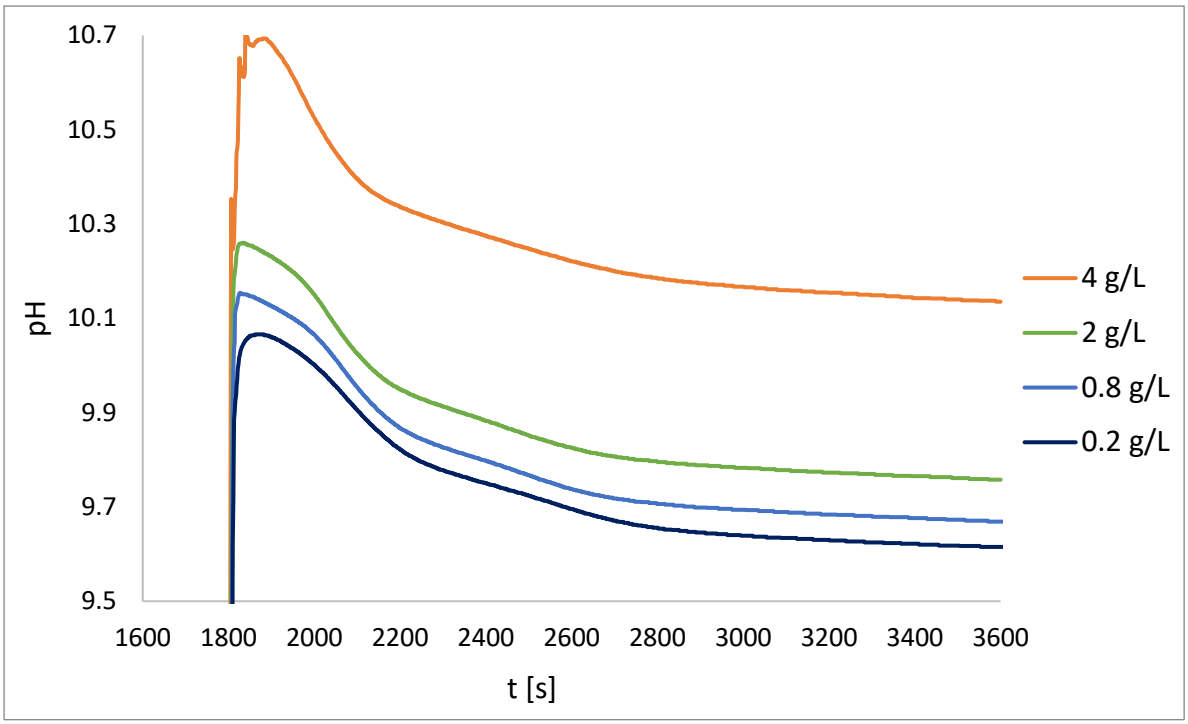

Figure 3.29. pH for different concentrations of calcium hydroxide. $Ca(OH)_2$ was released at t= 1 800 s.

The presence of brucite is unexpected, thus we checked whether it forms during the preparation of the slurry. Fig. 3.30 contains the spectra of a 1.5 M and a 6 M slurry. These XRD measurements are performed directly on the freshly prepared slurry. The 1.5 M sample is in amorphous form, with a small calcium hydroxide peak, while the 6 M sample shows a clear $Ca(OH)_2$ pattern with a trace of calcite. No presence of brucite is observed.

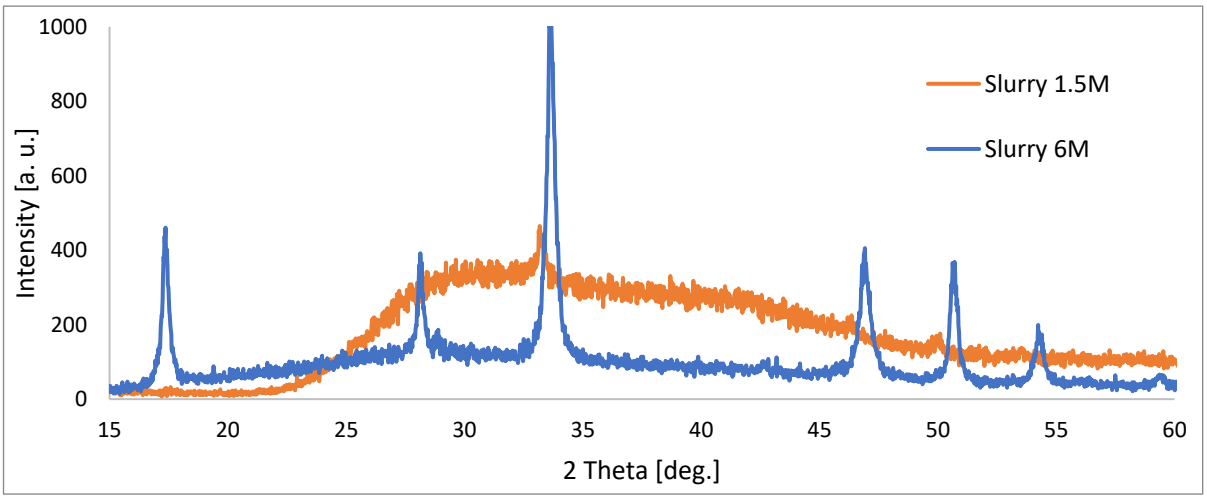

Figure 3.30. Spectra of 1.5 and 6 M slurry in comparison.

Eventually, a comparison between the solid obtained from the filtration of a solution prepared using powder or slurry was performed. The test on powder does not differ from the slurry with the same concentration (4 g/L), as shown in fig. 3.31. Therefore, the form of the $Ca(OH)_2$ does not affect the formation of solid phases during dissolution.

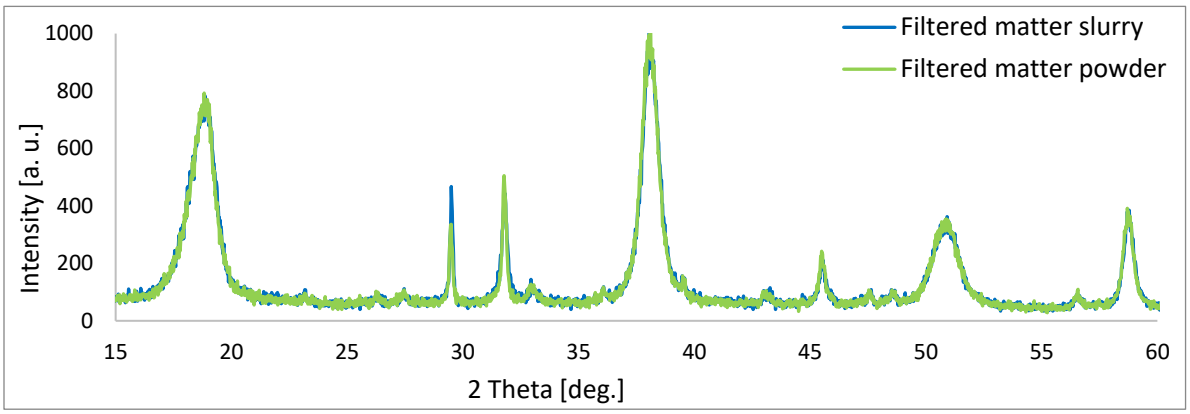

Figure 3.31. Comparison of diffraction patterns of filtered solid obtained from dissolution of $Ca(OH)_2$ in form of slurry (blue) and powder (green). For each form a concentration of 4 g/L is used.

3.8 Statistics results

In the following section the results of both the linear regression and the PCA are reported. All the statistical processing has been performed through the software *SPSS*, property of *IBM*.

3.8.1 Linear regression results

As a preliminary study, 65 samples are utilized for a brief statistical analysis. The data taking into consideration for each sample are both variables and numerical parameters: maximum pH reached, concentration, temperature, salinity, Δ conductivity, time to reach the maximum pH, pH after 30 minutes from the release, form of $Ca(OH)_2$ and the methodology of the stirring.
In tab 3.6 is shown the matrix of covariance, that gives the correlation index for each variable.

Table 3.6. Matrix of covariance for the whole dataset, all variables and parameters are considered.

	Concentration	Salinity	Temperature	Max pH	time max pH	pH at 3600s	Conductivity
Concentration	1	-0.02	-0.05	0.87	0.75	0.84	0.84
Salinity	-0.02	1	-0.14	-0.26	-0.32	-0.24	-0.27
Temperature	-0.05	-0.14	1	-0.30	-0.04	-0.37	-0.04
Max pH	0.87	-0.26	-0.30	1	0.84	0.99	0.89
time max pH	0.75	-0.32	-0.04	0.84	1	0.84	0.90
pH at 3600 s	0.84	-0.24	-0.33	0.99	0.84	1	0.88
Conductivity	0.84	-0.27	-0.04	0.89	0.90	0.88	1

It turns out that the highest positive correlations are among the variables: maximum pH, time to reach maximum pH, pH at 3 600 s and conductivity with one parameter, the concentration. This is not very surprising as the amount of $Ca(OH)_2$ is the direct responsible for the perturbation of these.
It is noteworthy to report, instead, the correlation for the other two parameters: salinity and temperature. The salinity does not show significant connections, they are all negative and lower than 0.300 except for time to reach maximum pH (-0.317). Even the temperature presents the same behavior: all the correlation are weakly negative, the strongest is with the maximum pH, -0.300.
After this, it is created a linear model able to replicate the maximum pH value, the most interesting (and potentially harmful) variable. The database of the considered experiments covers the whole range of parameters tested: concentration, form of the calcium hydroxide,

stirring type, salinity, temperature. However, in the model creation, the distinction is possible just for numerical parameters.

Considering as Y the maximum pH, the forward method of the linear regression restitutes as best predictors: the pH at 3 600s, the concentration and salinity. The model considers, as input concentrations between 0.05 and 4 g/L, where the linearity of pH is stronger (cf fig. 3.6 section 3.1) and has an R^2 of 0.987.

This information is reported for the statistic's sake of completeness, however it is evident that using as a predictor the pH after 30 minutes from dissolution provides a significant help to the model. In addition to this, the pH at 3 600 s is a variable to monitor, not a parameter that is possible to control.

With this consideration, it is developed a predictive model, to do this are taken into account only the known variables at the beginning of the experiments, concentration, salinity and temperature. Two models are constructed: the first one with all the concentrations (0.05-8 g/L), the second just in the interval 0.05-4 g/L.

For both model the R^2 obtained shows a good fit for the data: 0.814 for low concentrations and 0.901 considering all concentrations. However, looking at the normality tests of the residuals, Shapiro-Wilk and Kolmogorov-Smirnov, no model passes the test.

Concerning the homoscedasticity, a visual interpretation suggests that the residuals of the low-concentrations model fig. 3.32 are better distributed than the complete model, fig. 3.33. Outliers are present in both figures. It is decided to remove those data showing a regression standardized residual value > |2|. The removed outliers are shown in tab. 3.7 (low-concentration model) and in tab. 3.8 (complete model)

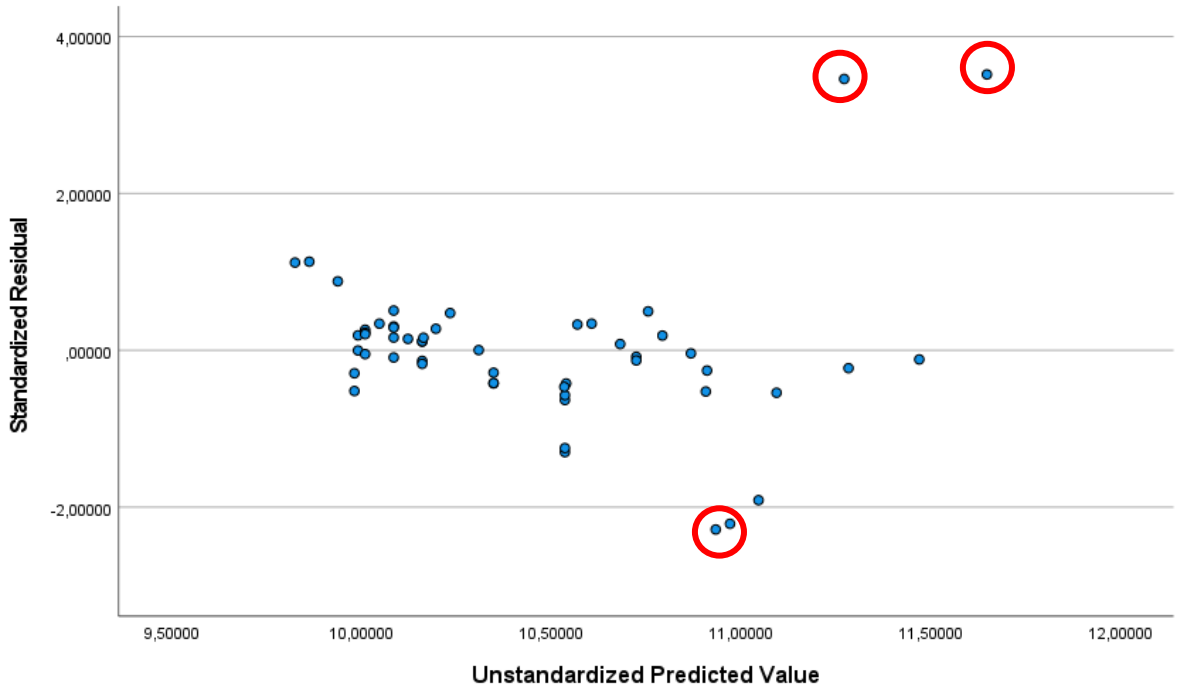

Figure 3.32. Scatterplot of the maximum pH for the low-concentration model. On the x-axis it is represented the predicted pH of the regression, on the y-axis, instead, the standardized residuals of the model are shown. The circled dots represent the removed outliers.

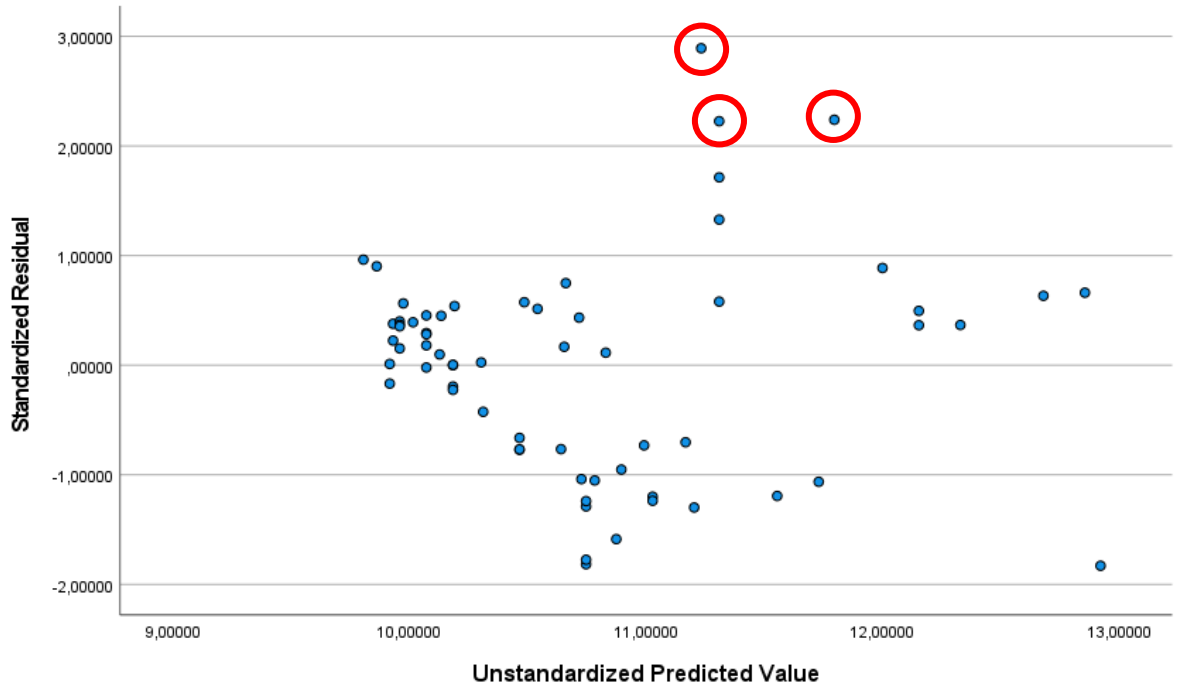

Figure 3.33. Scatterplot of the maximum pH for the complete model. On the x-axis it is represented the predicted pH of the regression, on the y-axis, instead, the standardized residuals of the model are shown. The circled dots represent the removed outliers.

Table 3.7. Removed outliers in the low-concentration model.

Test name	Concentration [g/L]	Form	Salinity	Stirring	Temperature	Max pH
2_6_10	0.2	Slurry	10	magnetic	25	10.45
3_6_10	0.4	Slurry	10	magnetic	25	10.50
5_6_10	2.0	Slurry	10	magnetic	25	12.01
6_6_10	4.0	Slurry	10	magnetic	25	12.39

Table 3.8. Removed outliers in the complete model.

Test name	Concentration [g/L]	Form	Salinity	Stirring	Temperature	Max pH
4_2_9	5.0	Powder	35	magnetic	25	11.90
5_6_10	2.0	Slurry	10	magnetic	25	12.01
6_6_10	4.0	Slurry	10	magnetic	25	12.39

Once removed the outliers, new models are computed. The R^2 improves in both models, for the low-centration reaching the value of 0.96, while for the complete one up to 0.934.

In the low-concentration model the values removed are those at low salinity (10‰), just one experiment remains, at 0.08 g/L. This, on one side, improves a lot the quality of the model, as shown by the R^2, but reduces too much the abundance of the dataset on that specific aspect.

The low-concentration model alone passes the normality test of the residuals in the Shapiro-Wilk and Kolmogorov-Smirnov tests.

The distribution of the standardized residuals is shown in fig. 3.34, reduced model, and in fig. 3.35, complete model.

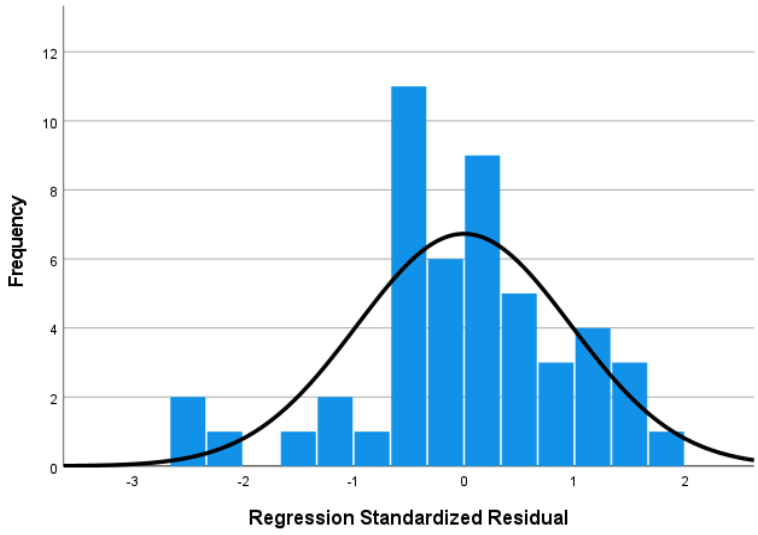

Figure 3.34. Histogram of the standardized residuals of the low-concentration model.

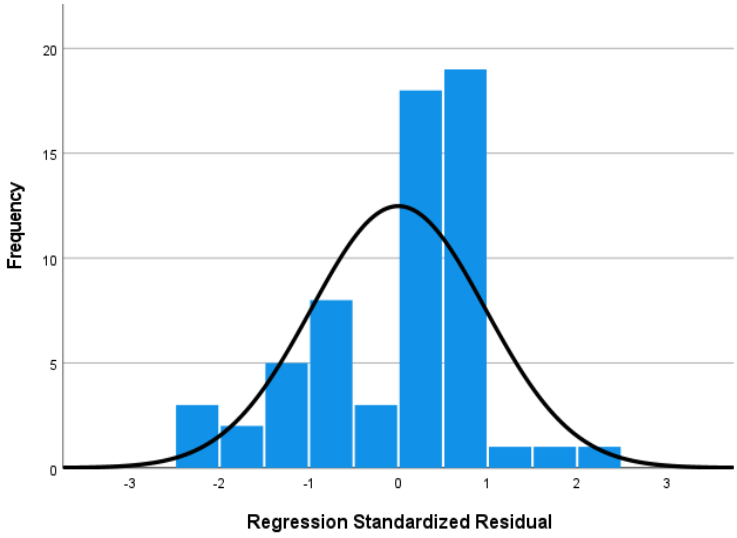

Figure 3.35. Histogram of the standardized residuals of the complete model.

More information about the standardized residues is provided in tab. 3.9.

Table 3.9. Statistical specifications on the residues for both the regression models.

	Low-concentrations model	**Complete model**
Residues standardized mean	$1.5 * 10^{-15}$	$1.37 * 10^{-14}$
Residues std deviation	0.071	0.975
Number of samples	49	61

Other conditions that must be verified to accept the linear model are: linearity of the predictors with the predicted output *Y* and absence of multicollinearity.

The first condition is not acceptable as shown in fig 3.36, 3.37 and 3.38. These figures show the relationship of each predictor with the output in the case of the restricted model (0.05 – 4 g/L concentration). A similar output is obtained in case of the complete model, the only difference is that the linear relationship for the couple pH-concentration is fairly respected.

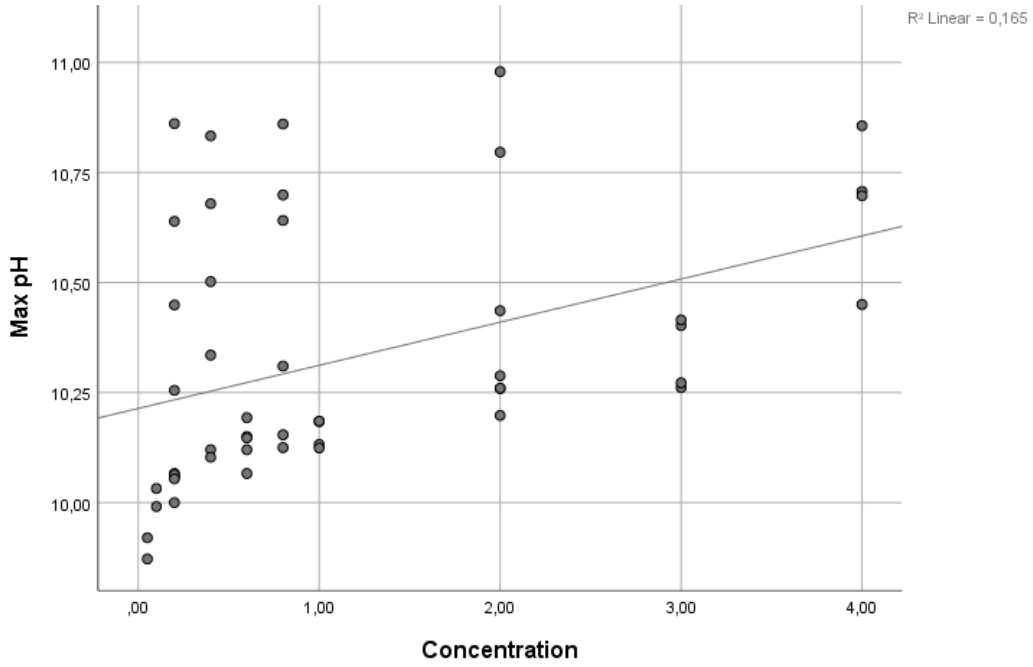

Figure 3.36. Linear regression on the maximum pH using as a unique predictor the concentration.

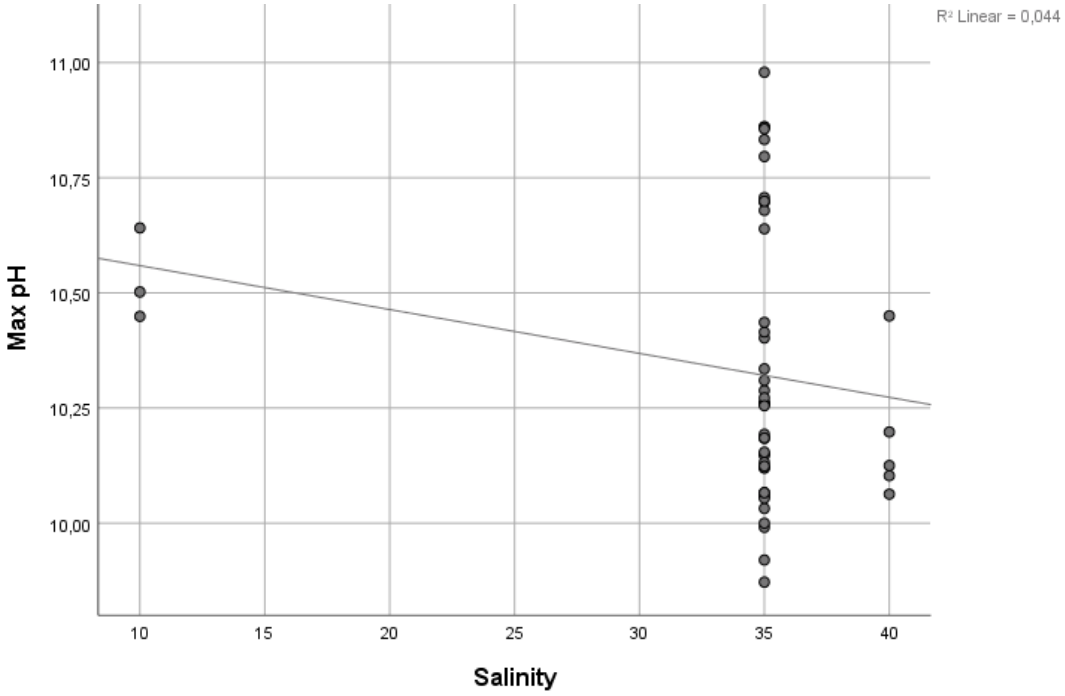

Figure 3.37. Linear regression on the maximum pH using as a unique predictor the salinity.

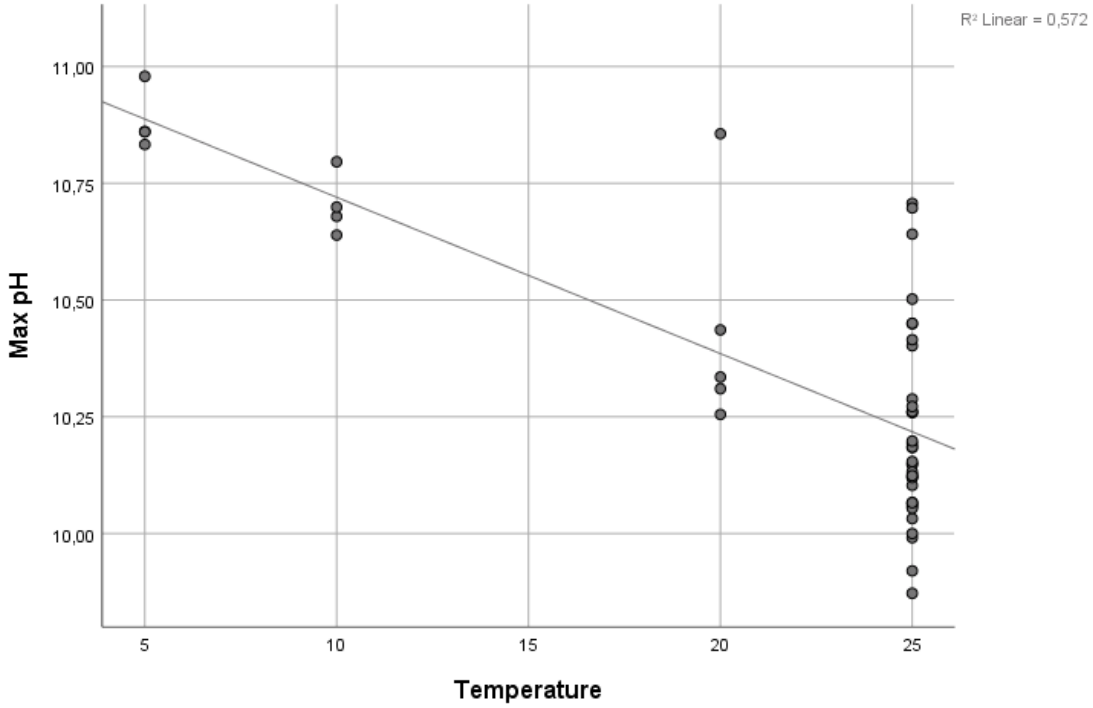

Figure 3.38. Linear regression on the maximum pH using as a unique predictor the temperature.

The second condition instead, absence of multicollinearity among predictors, shows good results as reported in tab. 3.10 with the VIF index.

Table 3.10. VIF index for each parameter of the reduced and complete model.

Parameter	**Reduced model**	**Complete model**
Concentration	1.009	1.005
Salinity	1.005	1.015
Temperature	1.004	1.010

Each model returns the linear equation as output: they are both reported in eq. 45 (low-concentration) and 46 (complete model).

$$Max\ pH = 11.626 + 0.142 \cdot Concentration - 0.018 \cdot Salinity - 0.039 \cdot Temperature \qquad (45)$$

$$Max\ pH = 11.456 + 0.274 \cdot Concentration - 0.017 \cdot Salinity - 0.037 \cdot Temperature \qquad (46)$$

The reduced model presents the highest R^2 and eq. 45 can be employed to evaluate the maximum pH reached in the interval 0.05-4 g/L, remembering that it should be simulated around the value of salinity at 35‰.

Even if the normality test of residuals is not satisfied, it is possible to exploit eq. 46 to simulate the maximum reached pH under a wider range of conditions concerning both concentration, temperature and salinity.

The graph confirms the correlation described in the covariance matrix and allows to simulate conditions not tested in laboratory.

The lines represented in fig. 3.39 are less significant when moving at low concentrations. In this case the explanation is immediate: extending the lines at concentration of 0 g/L would result in unrealistic levels of pH (range 9.4 – 11.4) when the pH of the artificial seawater varied between 6.5 and 7.

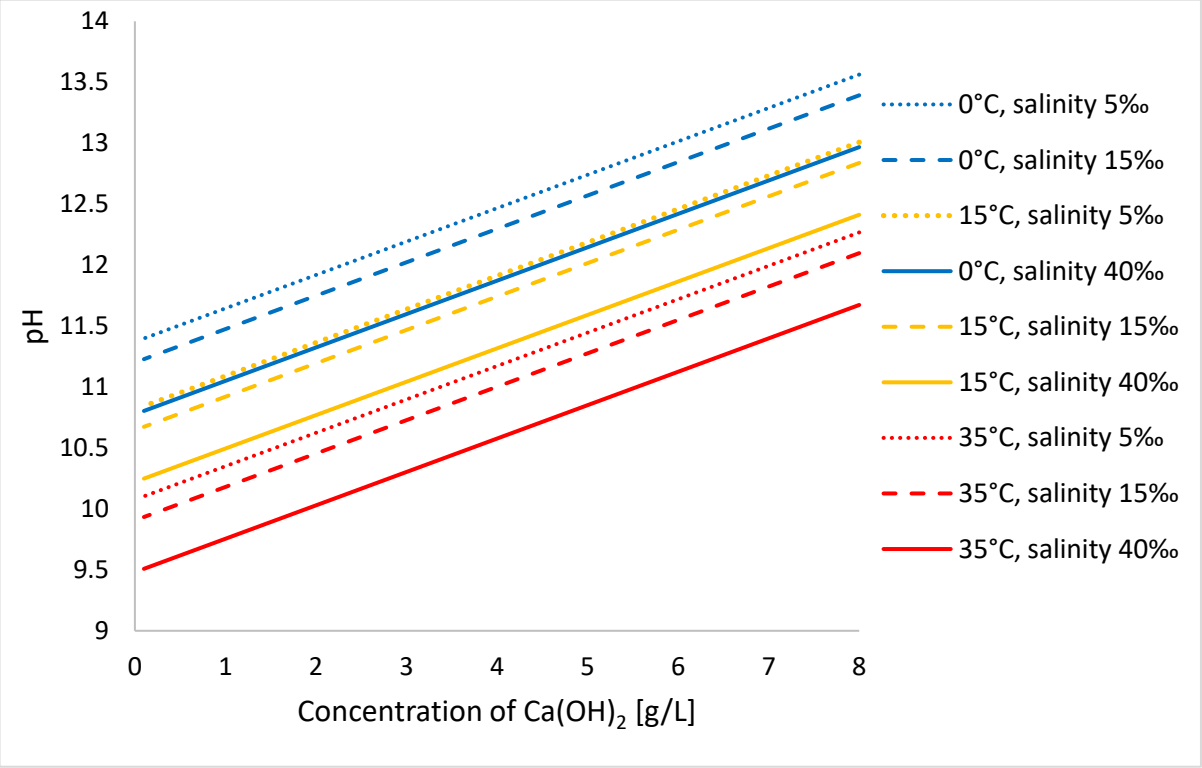

Figure 3.39. Maximum pH represented as function of three parameters: concentration, temperature and salinity. The concentration is represented on the x axis. The temperature is specified by the colour: blue lines represent simulations at 0°C, orange at 15 °C and red at 35°C. The style of the line indicates the salinity: dots stand for salinity at 5‰, dashed line for salinity at 15‰ and the solid line for salinity at 40‰.

The application of the model must be accompanied by an awareness of the limitations of its outputs. Fig. 3.40 shows the comparison between the output of the model (orange line), at conditions of salinity 35‰ and temperature of 25°C, with the experimental data at the same conditions, blue diamonds. The model linearly interpolates the data, with a maximum error of about 0.5 units of pH when the curve changes its trend at 4 g/L.

A possibility to increase the precision of the prediction is to use different models for various range of concentrations, or a non-linear model, that can better describe the behavior of the data.

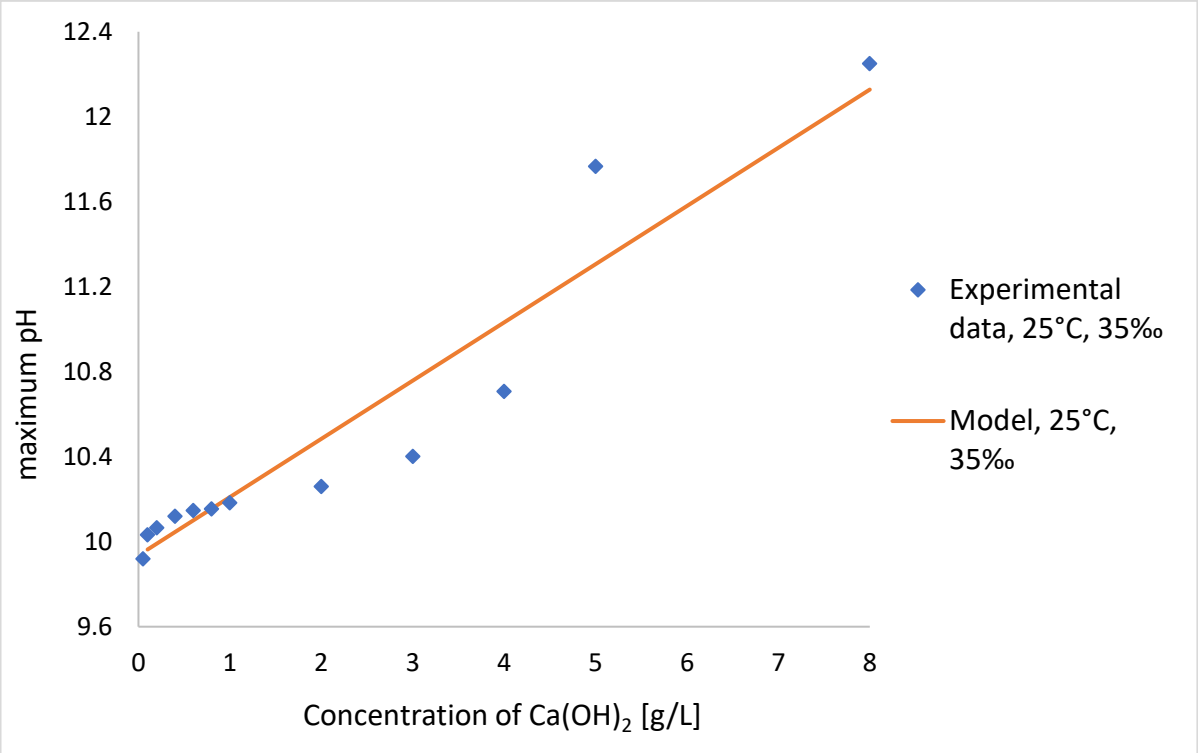

Figure 3.40. Comparison between the maximum pH reached by experimental data, blue diamonds and the output of the model, orange line.

3.8.2 PCA results

A principal component analysis is carried out on the complete dataset, to understand the most relevant variables and possibly reduce the dimensionality of the problem.

The variables and numerical parameters considered are: maximum pH reached, concentration, temperature, salinity, Δ conductivity, time to reach the maximum pH, pH after 30 minutes from the release.

The first preliminary analysis is performed on the kind of present variance. The results, shown in tab. 3.11, suggest that PCA technique can be applied to this dataset, as, except for salinity, the other variables and parameters have coefficients higher than 0.7.

Table 3.11. Communalities extracted for each variable/parameter of the dataset

Variable/parameter	Initial	Extraction
Max pH	1.00	0.97
Concentration	1.00	0.80
Conductivity	1.00	0.92
time Max pH	1.00	0.86
pH at 3600 s	1.00	0.96
Salinity	1.00	0.53
Temperature	1.00	0.71

The scree plot in fig. 3.41, gives a visual interpretation of the number of principal components to consider, as a rule of thumb it is suggested to maintain just eigenvalues higher than one, bringing the number of considered PC to 2. Moreover, the variance explained with two components is higher than 80%, reaching a value of 82.314 %, tab. 3.12.

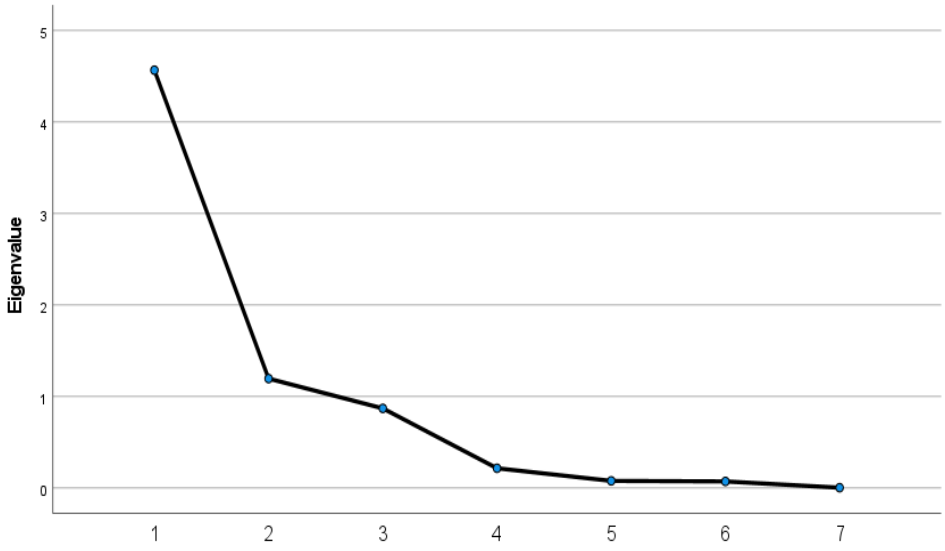

Figure 3.41. Scree plot of the eigenvalues, in decreasing order of relevance for each principal component.

Table 3.12. Variance and cumulative variance explained by each principal component.

Component	Total	% of Variance	Cumulative %
1	4.57	65.23	65.23
2	1.20	17.08	82.31
3	0.87	12.43	94.74
4	0.22	3.08	97.82
5	0.08	1.11	98.93
6	0.07	1.02	99.95
7	0.01	0.05	100.00

The component matrix, table 3.13, interprets the correlation of each variable with the component, values range from -1 to +1. The component 1, PC1, shows higher correlation with all variables, except salinity and temperature. These last are highly explained by the component 2, PC2.

Table 3.13. Component matrix, values for each component for parameter or variable.

Parameter/variable	Component 1	Component 2
Concentration	0.89	-0.07
Salinity	-0.29	-0.67
Temperature	-0.19	0.82
Max pH	0.98	-0.11
time Max pH	0.92	0.16
pH at 3600 s	0.97	-0.13
Conductivity	0.95	0.12

The component matrix is then rotated, approaching a simple structure to improve the interpretation. The orthogonal rotation is performed through *varimax* type rotation. The rotated component plot, in fig. 3.42, represents the variables/parameters plotted in an orthogonal space. The values shown are the result of a rotation and normalization of the extracted values from the components matrix.

Data show five variables, maximum pH reached, concentration, Δ conductivity, time to reach the maximum pH, pH after 30 minutes from the release, clustered with high positive values for

the PC1 and nearly zero for PC2. Salinity and temperature are, instead, negative concerning PC1, while, for PC2, they present an opposite sign.

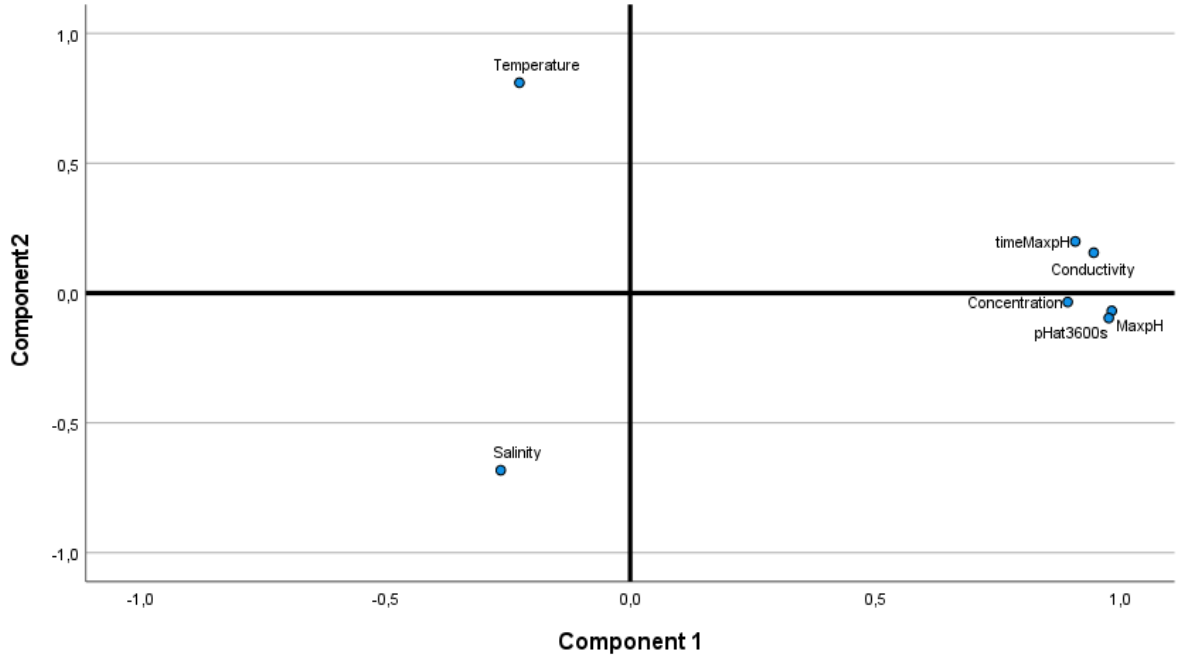

Figure 3.42. Component plot in the rotated space, the axes are the 2 principal components.

The representation of the samples according to the score obtained for each of the two principal components is shown in fig. 3.43. From the figure, it is possible to identify several clusters of data which reflect the above-cited considerations.

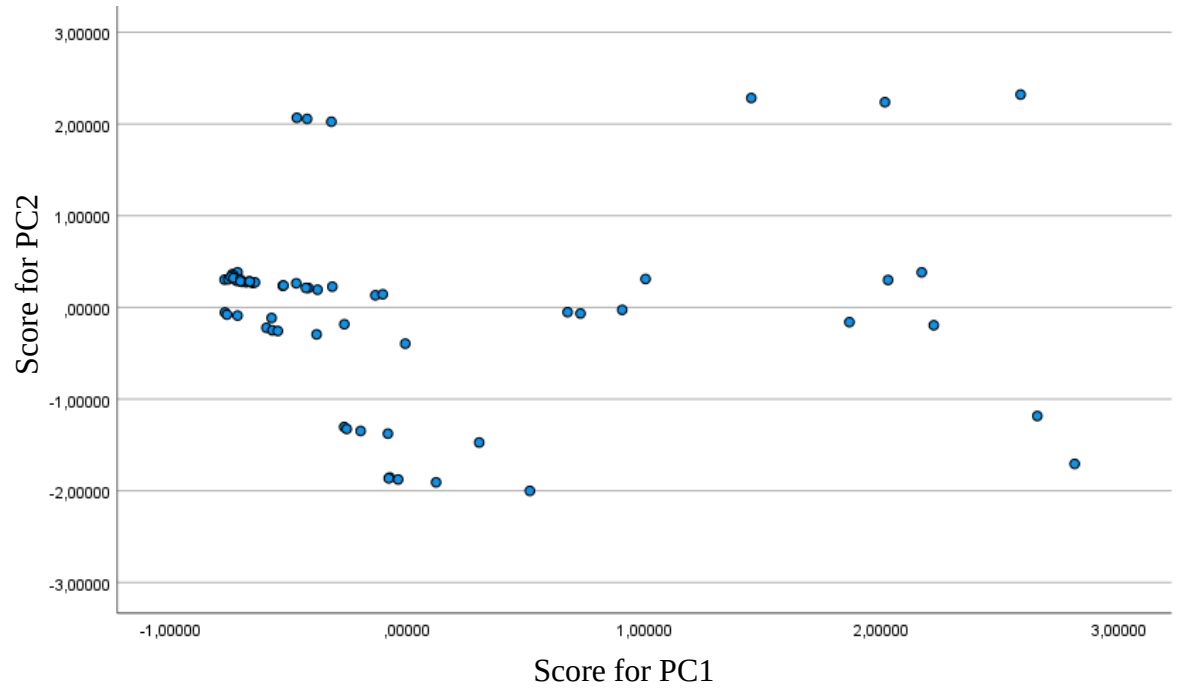

Figure 3.43. Scatterplot of samples in the principal components space.

Focusing just on the x-axis (PC1), the samples are mostly placed following the increasing concentration, fig. 3.44.

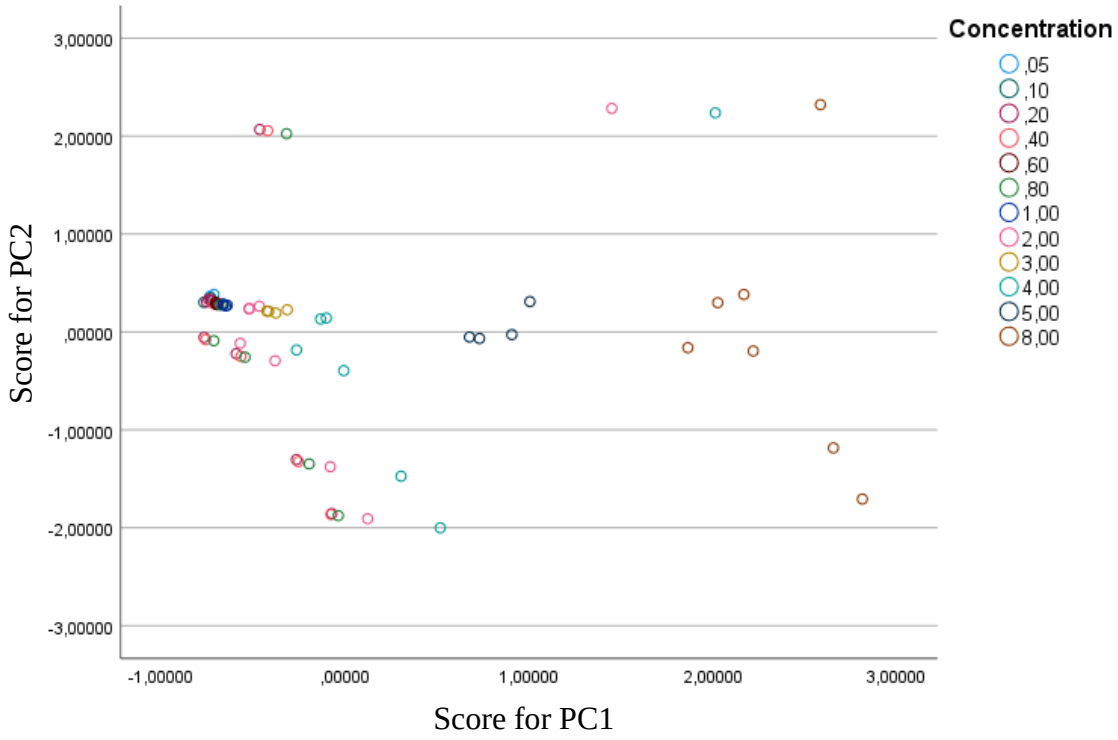

Figure 3.44. Scatterplot of the samples in the principal components spaces. Concentrations are highlighted by use of a color palette.

Looking at y-axis (PC2), the main differences are determined by salinity and temperature. Fig. 3.45 presents data colored according to the temperature of the experiment. The experiments are ordered from bottom to the top with ascending temperature.

Fig. 3.46 reports, instead, samples colored with respect to the value of salinity. It is evident the partition between high-salinity data, central and lower part of the graph, and low-salinity, upper part. However, there is no clear distinction in the pattern between 35‰ and 40‰ salinity.

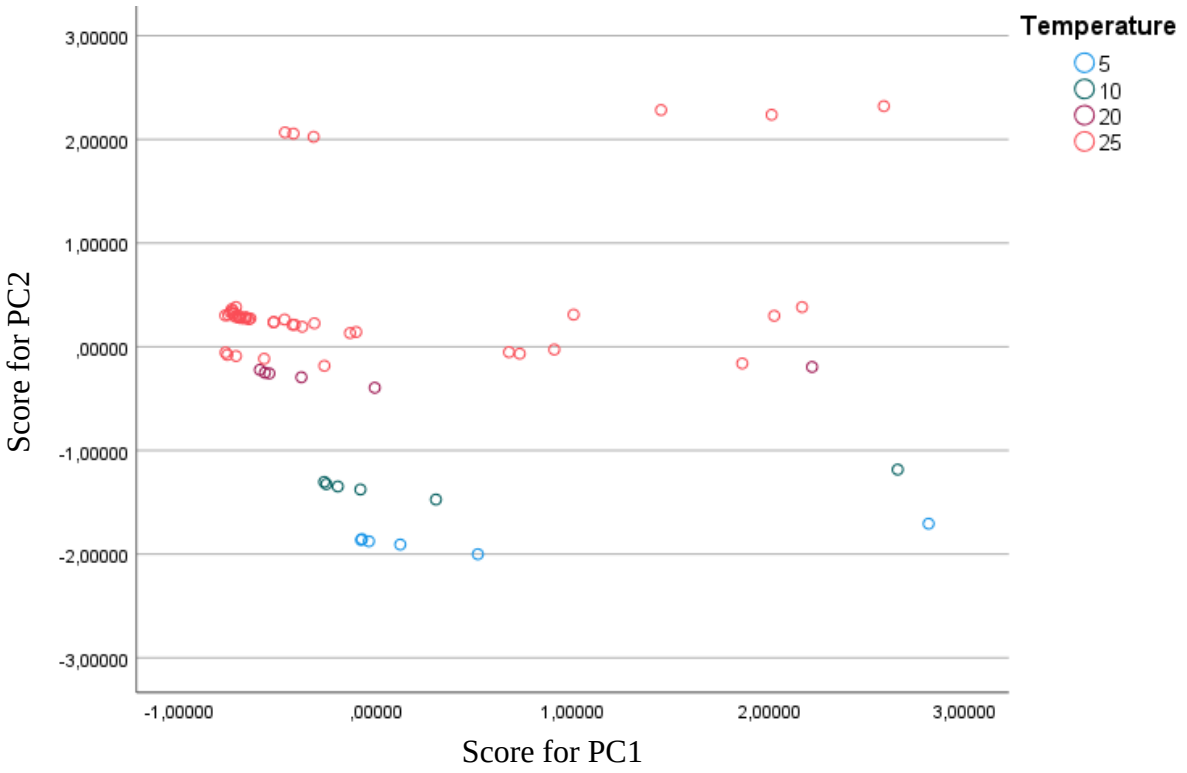

Figure 3.45. Scatterplot of the samples in the principal components spaces. Temperatures are highlighted by use of a color palette.

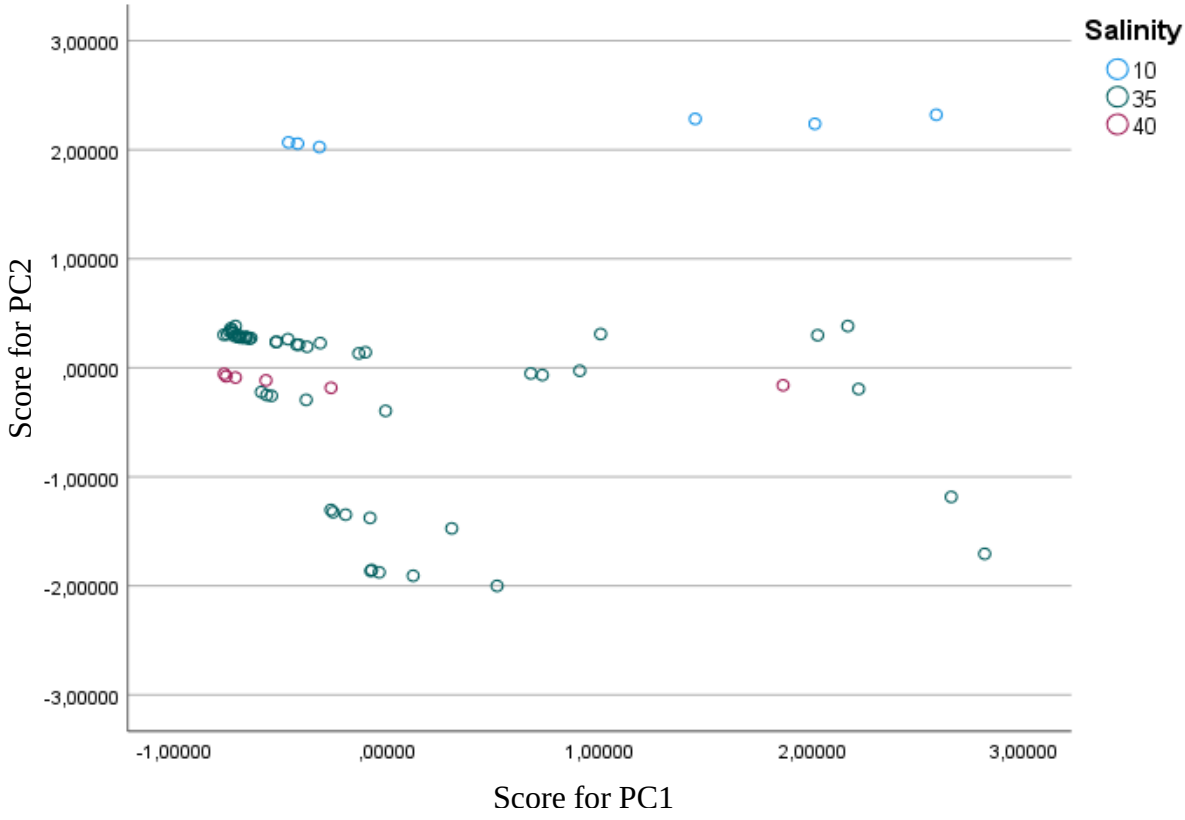

Figure 3.46. Scatterplot of the samples in the principal components spaces. Salinities are highlighted by use of a color palette.

4. Conclusion

This research presents a preliminary description of the dissolution kinetics of $Ca(OH)_2$ in seawater, confirming it to be a good candidate for ocean alkalization techniques.

Using the pH peak caused by the rapid release of the OH^- ions as reference, we can conclude that the dissolution is reached on average within a minute, for $Ca(OH)_2$ concentrations below 4 g/L. Afterwards, the pH decreases probably due to two concomitant factors: a) a fast precipitation of brucite, $Mg(OH)_2$; b) a slow and continuous absorption of CO_2 from the atmosphere. For concentrations of $Ca(OH)_2$ above 5 g/L, the pH peak reduces its pace after a sharp increase and the curve seems to reach a plateau.

The conductivity measurements suffer from many issues, extensively described in the previous sections. The conductivity registers variations in the order of 10^1 μS/cm for the concentrations lower than 0.2 g/L, of 10^2 μS/cm for concentration up to 4 g/L and of 10^3 μS/cm for values higher than 5 g/L.

It is likely that measurements are affected also by a delay while registering, as confirmed by the results obtained in dissolution tests performed in distilled water where most of the increment is reached within a minute. In seawater, instead, the lower the concentration, the higher is the time needed to register a well-defined and stable variation. This is about ten minutes or more for values lower than 0.2 g/L while it is in the order of a couple of minutes for concentrations higher than 5 g/L.

The main difference between the powder and the slurry form of $Ca(OH)_2$ is that the former dissolves more slowly. The pH peaks are almost equal in value, while the increments in conductivity are higher for the powder.

The salinity of seawater influences the maximum pH. Using the same $Ca(OH)_2$ concentrations, the pH is always higher in low salinity seawater, with the curves, from top to the bottom, ordered by increasing salinity.

The temperature variable, explored in section 3.5, has returned results of complex interpretation. Even though the dissolution reaction is exothermal and favored at low temperatures, the pH curves are placed alternatively in ascending or descending order according to the temperature.

The mechanism of dissolution is influenced also by the stirring method. A less effective method, i.e. the mechanical one, produces lower values of both pH and conductivity, also slowing the reaction in time.

Concerning alkalinity two observations can be outlined. Firstly, it increases rapidly (for ca. one hour) with a subsequent slow decrease. Secondly, a significant increase of alkalinity is registered when measuring samples at concentration higher than 4 g/L.

The analysis of the filtered matter by XRD demonstrates that, during the dissolution, there is a concurrent formation of brucite and calcite. Small amounts of aragonite and cristobalite are found as well, whereas no traces of calcium hydroxide are found.

This thesis represents a good starting point to develop future works. A series of experiments with real seawater will be necessary, as the seawater used was laboratory-made. Moreover, a quantitative assessment of the effected CO_2 absorbed by the solution is needed.

A feature and limitation of the research is the limited volume of solution, all the experiments were performed without any possibility to dilution. Broadening the outlook to the Desarc-Maresanus project, studies that consider major volumes and the dilution effect should be conducted.

Another possible development concerning the research is using different grain sizes of $Ca(OH)_2$, a parameter that was not included in the current study but that could strongly affect the dissolution.

Data obtained from this work will be useful to create and train a model able to reproduce the kinetic of dissolution of $Ca(OH)_2$, and provide information for an effective spreading of the lime without damaging the marine biota.

This work may also help to assess the correct amount of $Ca(OH)_2$ to use in the spreading phase, depending on the conditions of salinity and temperature.

The study provides useful information and data for the successful development of the Desarc-Maresanus project, confirming, by experimental data, that ocean liming determines an increase of the pH.

5. Bibliography

Caserini, S., et. al. (2020). Analisi dei dati del traffico marittimo per la stima delle emissioni di co2 dalle navi e del potenziale di alcalinizzazione del mar Mediterraneo. *Ingegneria Dell'ambiente*, *7*(3). https://doi.org/10.32024/ida.v7i3.274

Aminu, M. D., Nabavi, S. A., Rochelle, C. A., & Manovic, V. (2017). A review of developments in carbon dioxide storage. *Applied Energy*, *208*, 1389–1419. https://doi.org/10.1016/J.APENERGY.2017.09.015

Baláš, M., Lisý, M., Milčák, P., & Pospíšil, J. (2017). Influence of steam temperature on biomass gasification process. *Waste Forum*, *5*, 372–378.

Barron, J., Ashton, C., & Geary, L. (2005). The Effects of temperature on pH measurement. *Tsp*, *1*(2), 1–7. http://www.reagecon.com/pdf/technicalpapers/Effects_of_Temperature_on_pH_v4-_TSP-01-2.pdf

Bell, David A., Brian F. Towler, and M. F. (2010). *Coal gasification and its applications.* William Andrew.

Bradshaw, A. L., & Schleicher, K. E. (1980). Electrical Conductivity of Seawater. *IEEE Journal of Oceanic Engineering*, *5*(1), 50–62. https://doi.org/10.1109/JOE.1980.1145449

Brasseur, P., Beckers, J. M., Brankart, J. M., & Schoenauen, R. (1996). Seasonal temperature and salinity fields in the Mediterranean Sea: Climatological analyses of a historical data set. *Deep-Sea Research Part I: Oceanographic Research Papers*, *43*(2), 159–192. https://doi.org/10.1016/0967-0637(96)00012-X

Butenschön, M., Lovato, T., Masina, S., Caserini, S., & Grosso, M. (2021). Alkalinization Scenarios in the Mediterranean Sea for Efficient Removal of Atmospheric CO2 and the Mitigation of Ocean Acidification. *Frontiers in Climate*, *3*(March), 1–11. https://doi.org/10.3389/fclim.2021.614537

Campo, F., Caserini, S., Pagano, D., Dolci, G., Grosso, M., Milano, P., Dipartimento, D., Del, A., Di, C., Di, V., Processo, U. N., La, V., & Atmosferica, C. O. (2020). *Ingegneria dell'Ambiente n. 1-2020*.

Campo, F. P. (2019). Life cycle assessment of a carbon dioxide removal process. *Methods*, *310420*, 22–29.

Caserini, S., Barreto, B., Lanfredi, C., Cappello, G., Ross Morrey, D., & Grosso, M. (2019). Affordable CO2 negative emission through hydrogen from biomass, ocean liming, and CO2 storage. *Mitigation and Adaptation Strategies for Global Change*, *24*(7), 1231–1248. https://doi.org/10.1007/s11027-018-9835-7

Caserini, S., Dolci, G., Azzellino, A., Lanfredi, C., Rigamonti, L., Barreto, B., & Grosso, M.

(2017). Evaluation of a new technology for carbon dioxide submarine storage in glass capsules. *International Journal of Greenhouse Gas Control*, *60*, 140–155. https://doi.org/10.1016/J.IJGGC.2017.03.007

Caserini, S., Pagano, D., Campo, F., Abbà, A., De Marco, S., Righi, D., Renforth, P., & Grosso, M. (2021). Potential of Maritime Transport for Ocean Liming and Atmospheric CO2 Removal. *Frontiers in Climate*, *3*(April), 1–18. https://doi.org/10.3389/fclim.2021.575900

Chou, C. T., Chen, F. H., Huang, Y. J., & Yang, H. S. (2013). Carbon dioxide capture and hydrogen purification from synthesis gas by pressure swing adsorption. *Chemical Engineering Transactions*, *32*(1995), 1855–1860. https://doi.org/10.3303/CET1332310

Corinne Le Quéré et al. (2018). *Global Carbon Budget 2018*. *10*(4).

Couto, N., Rouboa, A., Silva, V., Monteiro, E., & Bouziane, K. (2013). Influence of the Biomass Gasification Processes on the Final Composition of Syngas. *Energy Procedia*, *36*, 596–606. https://doi.org/10.1016/J.EGYPRO.2013.07.068

Dickson, A G and Goyet, C. (1994). *Handbook of methods for the analysis of the various parameters of the carbon dioxide system in sea water. Version 2*. https://doi.org/10.2172/10107773

Down, Randy D., Jay H. Lehr, E. (2005). *Environmental instrumentation and analysis handbook*. John Wiley & Sons.

EPA. (2021). https://www.epa.gov/, Accessed on November 2021

Fuss, S., Canadell, J., Peters, G. et al. (2014). Betting on negative emissions. *Nature Clim Change*, *4*, 850–853. https://doi.org/https://doi.org/10.1038/nclimate2392

Fuss, S., Lamb, W. F., Callaghan, M. W., Hilaire, J., Creutzig, F., Amann, T., Beringer, T., De Oliveira Garcia, W., Hartmann, J., Khanna, T., Luderer, G., Nemet, G. F., Rogelj, J., Smith, P., Vicente, J. V., Wilcox, J., Del Mar Zamora Dominguez, M., & Minx, J. C. (2018). Negative emissions - Part 2: Costs, potentials and side effects. *Environmental Research Letters*, *13*(6). https://doi.org/10.1088/1748-9326/aabf9f

G. Cappello & D. Ross Morrey, *CO2APPS Patent PCT/IB2018/050336 19/1/2018 patent n° 102017000006623*. (2018).

Giles, D. E., Ritchie, I. M., & Xu, B. A. (1993). The kinetics of dissolution of slaked lime. *Hydrometallurgy*, *32*(1), 119–128. https://doi.org/10.1016/0304-386X(93)90061-H

Gim, B. M., Hong, S., Lee, J. S., Kim, N. H., Kwon, E. M., Gil, J. W., Lim, H. H., Jeon, E. C., & Khim, J. S. (2018). Potential ecotoxicological effects of elevated bicarbonate ion concentrations on marine organisms. *Environmental Pollution*, *241*, 194–199. https://doi.org/10.1016/J.ENVPOL.2018.05.057

Han, S. J., Yoo, M., Kim, D. W., & Wee, J. H. (2011). Carbon dioxide capture using calcium

hydroxide aqueous solution as the absorbent. *Energy and Fuels*, *25*(8), 3825–3834. https://doi.org/10.1021/ef200415p

Hansen, J., Kharecha, P., Sato, M., Masson-Delmotte, V., Ackerman, F., Beerling, D. J., Hearty, P. J., Hoegh-Guldberg, O., Hsu, S. L., Parmesan, C., Rockstrom, J., Rohling, E. J., Sachs, J., Smith, P., Steffen, K., Van Susteren, L., Von Schuckmann, K., & Zachos, J. C. (2013). Assessing "dangerous climate change": Required reduction of carbon emissions to protect young people, future generations and nature. *PLoS ONE*, *8*(12). https://doi.org/10.1371/journal.pone.0081648

IPCC. (2014). Climate Change 2013 - The Physical Science Basis. In Intergovernmental Panel on Climate Change (Ed.), *IPCC.ch*. Cambridge University Press. https://doi.org/10.1017/CBO9781107415324

IPCC. (2021a). *IPCC, 2021: Climate Change 2021: The Physical Science Basis. Contribution of Working Group I to the Sixth Assessment Report of the Intergovernmental Panel on Climate Change [Masson-Delmotte, V., P. Zhai, A. Pirani, S.L. Connors, C. Péan, S. Berger, N. Cau*. Cambridge University Press. https://www.ipcc.ch/report/ar6/wg1/

IPCC. (2021b). IPCC 2021 Technical Summary. *Ipcc*, *August*, 150. https://www.ipcc.ch/report/ar6/wg1/downloads/report/IPCC_AR6_WGI_TS.pdf

IPCC SR 1.5°. (2018). Global warming of 1.5°C. An IPCC Special Report on the impacts of global warming of 1.5°C above pre-industrial levels and related global greenhouse gas emission pathways, in the context of strengthening the global response to the threat of climate change,. *Ipcc - Sr15*, *2*(October), 17–20. www.environmentalgraphiti.org

Janssen, F., Schrum, C., & Backhaus, J. O. (1999). A climatological data set of temperature and salinity for the Baltic Sea and the North Sea. *Deutsche Hydrographische Zeitschrift*, *51*(9 Supplement), 5–245. https://doi.org/10.1007/BF02933676

Johannsen, K., & Rademacher, S. (1999). Modelling the kinetics of calcium hydroxide dissolution in water. *Acta Hydrochimica et Hydrobiologica*, *27*(2), 72–78. https://doi.org/10.1002/(SICI)1521-401X(199902)27:2<72::AID-AHEH72>3.0.CO;2-H

Johnson, R. A., & Wichern, D. (2014). *Applied multivariate statistical analysis* (Pearson).

Kweku, D., Bismark, O., Maxwell, A., Desmond, K., Danso, K., Oti-Mensah, E., Quachie, A., & Adormaa, B. (2018). Greenhouse Effect: Greenhouse Gases and Their Impact on Global Warming. *Journal of Scientific Research and Reports*, *17*(6), 1–9. https://doi.org/10.9734/jsrr/2017/39630

Logan, C. A. (2010). A Review of Ocean Acidification and America's Response. *BioScience*, *60*(10), 819–828. https://doi.org/10.1525/bio.2010.60.10.8

Meier, Peter, Albert Lohrum, and J. G. (1989). *Practice and theory of pH measurement*. Ingold Messtechnik AG, Urdorf, Switzerland.

Mettler-Toledo. (2016). A Guide to pH Measurement. *Theory & Practice of Laboratory PH Applications*, 1–52. www.mt.com/pH

Millero, F. J. (2007). The marine inorganic carbon cycle. *Chemical Reviews*, *107*(2), 308–341. https://doi.org/10.1021/cr0503557

Miner, G. (2006). (2006). *Standard Methods for the Examination of Water and Wastewater* (American Water Works Association (Ed.)). https://www.proquest.com/scholarly-journals/standard-methods-examination-water-wastewater/docview/221578868/se-2?accountid=28385

Minx, J. C., Lamb, W. F., Callaghan, M. W., Fuss, S., Hilaire, J., Creutzig, F., Amann, T., Beringer, T., de Oliveira Garcia, W., Hartmann, J., Khanna, T., Lenzi, D., Luderer, G., Nemet, G. F., Rogelj, J., Smith, P., Vicente Vicente, J. L., Wilcox, J., & del Mar Zamora Dominguez, M. (2018). Negative emissions—Part 1: Research landscape and synthesis. *Environmental Research Letters*, *13*(6), 063001. https://doi.org/10.1088/1748-9326/aabf9b

MTR-Membranes. (2017). *MTR membranes for CO2 removing from syngas*. https://www.mtrinc.com/our-business/refinery-and-syngas/co2-removal-from-syngas/

NIST Chemistry WebBook. https://webbook.nist.gov/, Accessed on November 2021

NOAA. (2021). https://research.noaa.gov/, Accessed on November 2021

Ramos, P. M., Pereira, J. M. D., Member, S., Ramos, H. M. G., Member, S., & Ribeiro, A. L. (2008). *A Four-Terminal Water-Quality-Monitoring Conductivity Sensor*. *57*(3), 577–583.

Rayner, T. (2021). Taking the slow route to decarbonisation? Developing climate governance for international transport. *Earth System Governance*, *8*, 100100. https://doi.org/10.1016/J.ESG.2021.100100

Renforth, P., Jenkins, B. G., & Kruger, T. (2013). Engineering challenges of ocean liming. *Energy*, *60*, 442–452. https://doi.org/10.1016/J.ENERGY.2013.08.006

Renforth, Phil. (2019). The negative emission potential of alkaline materials. *Nature Communications*, *10*(1). https://doi.org/10.1038/s41467-019-09475-5

Renforth, Phil, & Henderson, G. (2017). Assessing ocean alkalinity for carbon sequestration. *Reviews of Geophysics*, *55*(3), 636–674. https://doi.org/10.1002/2016RG000533

Reverdin, G., Kestenare, E., Frankignoul, C., & Delcroix, T. (2007). Surface salinity in the Atlantic Ocean (30°S–50°N). *Progress in Oceanography*, *73*(3–4), 311–340. https://doi.org/10.1016/J.POCEAN.2006.11.004

Richard E. Zeebe, D. A. W.-G. (2002). CO2 in Seawater: Equilibrium, Kinetics, Isotopes. *Journal of Marine Systems*, *36*(3–4), 269–270. https://doi.org/10.1016/s0924-7963(02)00179-3

Roy, R. N., Roy, L. N., Vogel, K. M., Porter-Moore, C., Pearson, T., Good, C. E., Millero, F. J., & Campbell, D. M. (1993). The dissociation constants of carbonic acid in seawater at salinities 5 to 45 and temperatures 0 to 45°C. *Marine Chemistry*, *44*(2–4), 249–267. https://doi.org/10.1016/0304-4203(93)90207-5

Rruff Database. (2021). *RRUFF Project*. Access on November 2021.

Sá, M. V. C., & Boyd, C. E. (2017). Dissolution rate of calcium carbonate and calcium hydroxide in saline waters and its relevance for aquaculture. *Aquaculture*, *469*, 102–105. https://doi.org/10.1016/j.aquaculture.2016.11.033

Smirniotis, Panagiotis, and K. G. (2015). *Water gas shift reaction: research developments and applications.* Elsevier.

Smith, P., Davis, S. J., Creutzig, F., Fuss, S., Minx, J., Gabrielle, B., Kato, E., Jackson, R. B., Cowie, A., Kriegler, E., Van Vuuren, D. P., Rogelj, J., Ciais, P., Milne, J., Canadell, J. G., McCollum, D., Peters, G., Andrew, R., Krey, V., … Yongsung, C. (2016). Biophysical and economic limits to negative CO2 emissions. *Nature Climate Change*, *6*(1), 42–50. https://doi.org/10.1038/nclimate2870

Tamm, K., Kallaste, P., Uibu, M., Kallas, J., Velts-Jänes, O., & Kuusik, R. (2016). Leaching thermodynamics and kinetics of oil shale waste key components. *Oil Shale*, *33*(1), 80–99. https://doi.org/10.3176/oil.2016.1.07

Tilton, Leroy W., and J. K. T. (1922). Accurate representation of the refractivity and density of distilled water as a function of temperature. *Phys., Rev 2.20: 249*.

Ucla institute. Accessed on November 2021, from https://stats.idre.ucla.edu/

Uibu, M., Tamm, K., Velts-Jänes, O., Kallaste, P., Kuusik, R., & Kallas, J. (2015). Utilization of oil shale combustion wastes for PCC production: Quantifying the kinetics of Ca(OH)2 and CaSO4·2H2O dissolution in aqueous systems. *Fuel Processing Technology*, *140*, 156–164. https://doi.org/10.1016/j.fuproc.2015.09.010

UN. (1992). *A/CONF.151/26/Rev.l (Vol. l) Report of the United Nations Conference on Environment and Development Rio de Janeiro, 3-14 June 1992 Volume I Resolutions Adopted by the Conference*.

Van Eekeren, M. W. M., and J. van P. (1994). *Improved milk-of-lime for softening of drinking water- the answer to the carry-over problem. Aqua 43.1*.

Vonk, G., Piriou, B., Felipe Dos Santos, P., Wolbert, D., & Vaïtilingom, G. (2019). Comparative analysis of wood and solid recovered fuels gasification in a downdraft fixed bed reactor. *Waste Management*, *85*, 106–120. https://doi.org/10.1016/J.WASMAN.2018.12.023

Wang, J., Keener, T. C., Li, G., & Khang, S. J. (1998). The dissolution rate of Ca(OH)2 in aqueous solutions. *Chemical Engineering Communications*, *169*, 167–184. https://doi.org/10.1080/00986449808912726

www.desarc-maresanus.net. (2021). https://www.desarc-maresanus.net/

Zamfirescu, C., & Dincer, I. (2009). Ammonia as a green fuel and hydrogen source for vehicular applications. *Fuel Processing Technology*, *90*(5), 729–737. https://doi.org/10.1016/J.FUPROC.2009.02.004

6. Appendix

6.1 pH-meter (Mettler-Toledo InLab Routine Pro-ISM)

The pH-meter is an instrument with great versatility and accuracy. It is necessary to pay attention to many elements in order to optimize the measurements. The instrument can work just when attached at its "SevenExcellence" console to which it is connected via cable with a BNC connector. The sensor has a small plastic cap at the top of the glass tube which allows the electrode to be filled with its specific solution supplied (KCl 3 mol/L), the glass body must always be full of it. A small cylinder, opened on one of the two bases and filled with a specific solution, protects the membrane at the tip of the sensor when the instrument is not working. The cap must be always on the top of the sensor when it is not employed, otherwise damages may occur.

It is important to calibrate the instrument periodically or when it is suspected that the measurements are no longer accurate. This may be identified by measuring one of the supplied solutions, with known pH, and comparing the output of the instrument with the expected one. During this research, the instrument was recalibrated, on average, every two weeks. The procedure and type of calibration is selected via the "SevenExcellence" interface. Then, taking care to clean the electrode with distilled water from one measurement to another, it is sufficient to use the provided standards in sequence. For better accuracy, it is recommended to use three standards among whom one should be close to the values of the future samples analyzed.

6.2 Conductivity-meter (Mettler-Toledo InLab 731-ISM)

The conductivity-meter is, perhaps, the simplest and easiest maintenance sensor, it has to be stored dry. It is connected to "SevenExcellence" console via a cable with BNC connector too.

Calibration should be carried out periodically, in the case of this research it was performed about every two weeks. The calibration mode and the standards to be used (as close as possible to the samples to be analyzed) are selected from the interface, then the sensor is immersed in the selected standards one after the other.

The sensor produces some noise in the results that are due to: the base value of conductivity or the temperature variation during a test. These limitations are explained in section 2.3 and 2.5.2. It is recommended to maintain a stable temperature during the trial, otherwise these noises are observed throughout all the experiment. The software allows you to select different types of temperature compensation; it is advisable search into the literature, selecting the most suitable compensation for the analyzed solution and the goal of the experiment.

An observed small flaw is its sensitivity, which is in the order of 1‰ of the read data value. At high conductivities (seawater), this signifies a variation of roughly 50 µS/cm, causing a sort of discrete step measurements of that variable.

6.3 Calcium – meter (PerfectION comb CA)

The calcium sensor is the third sensor used in the experiments and attached to the SevenExcellence instrument. It is very sensitive and the most difficult to use. It worked properly for a few tests but the head quickly degraded to the point where the instrument became unreliable and was shelved.

The sensor consists of several components, the most delicate is the head, which has a very sensitive membrane which should never be rubbed or torn, this membrane degrades through the use until it does not provide reliable data. The head is closed by a plastic tube which has always to be filled with its electrolyte solution.

The instrument tends to lose its calibration day by day and the calibration should be carried out periodically, at least every week. To perform the calibration, it is sufficient to select the standards and the mode from the "SevenExcellence" interface. Standards are prepared by diluting, at different concentrations with distilled water, the standard at 1 000 g/L of Ca^{++}. In addition to this, a small quantity of the ISA solution, a signal-amplifier electrolyte (2 ml every 100 ml of standard) is employed. Solution has to be shaked with a magnetic stirring rod, two or three points for calibration are suggested.

If the sensor is planned to be used in the next 3 to 4 days, it has to be stored in a 100 g/L of Ca^{++} solution and, inside the electrode, it must be kept filled with its own solution. Otherwise it can be disassembled and stored.

6.4 Automatic titrator

The automatic titrator returns the alkalinity value in mg/L of $CaCO_3$ equivalent, after analyzing 50 ml of solution. It has two working options: one for low alkalinity values (up to 400 mg/L) and one for high alkalinity values (up to 4000 mg/L). It has to be calibrated for each mode and appropriate solutions are used. In this research, the instrument was calibrated every week.

From the interface it is possible to select the calibration mode, start the tests and save the data. To calibrate it follow the instructions the calibration is performed on 50 ml (distilled water and proper standard alkalinity solution in different proportions depending on the selected high/low range of values). Accuracy is required in this step, a pipette with a capacity of 2 mL is supplied with the instrument and it is suggested to use it for the low mode calibration.

The automatic titrator consists also of a pH-meter (necessary to be calibrated every week) and a thermometer, each time a titration is performed, they are immersed in the solution and they must be cleaned with distilled water at the end of the use. The pH-meter is slower to reach the equilibrium value if compared with the "SevenExcellence" pH-meter.

The body of the pH-meter, as the "SevenExcellence" one, is filled with its proper solution and the membrane on the tip of the sensor is protected by a plastic cap, filled with a storage solution, when not in use.

For titration of solutions that exceed the limit of 4000 mg $CaCO_3$ it is possible to pour less than 50 ml and then rescale the final result (for example for 25 ml, the result should be multiplied by 2), of course this reduces the accuracy of the measurement.

The instrument has an old interface, sometimes it crashes and saving data into a USB stick can be a bit slow.